UCRL-10531

University of California

Ernest O. Lawrence
Radiation Laboratory

NUCLEAR REACTIONS INDUCED BY PIONS AND PROTONS

Berkeley, California

DISCLAIMER

UCRL-10531
UC-34 Physics
TID-4500 (18th Edition)

UNIVERSITY OF CALIFORNIA

Lawrence Radiation Laboratory
Berkeley, California

Contract No. W-7405-eng-48

NUCLEAR REACTIONS INDUCED BY PIONS AND PROTONS

Paul L. Reeder

(Ph. D. Thesis)

November 27, 1962

Printed in USA. Price $2.75. Available from the
Office of Technical Services
U. S. Department of Commerce
Washington 25, D.C.

Contents

NUCLEAR REACTIONS INDUCED BY PIONS AND PROTONS

Paul L. Reeder

Lawrence Radiation Laboratory and Department of Chemistry
University of California
Berkeley, California

November 27, 1962

ABSTRACT

Effects due to elementary particle-like collisions within nuclear matter have been observed in several nuclear reactions caused by pions and protons. Simple nuclear reactions of the form $Z^{A}(a,an)Z^{A-1}$ and $Z^{A}(a,ap)(Z-1)^{A-1}$ have excitation functions that are sensitive to changes in the elementary-particle cross sections.

The excitation function for the reaction $C^{12}(\pi^-,\pi^-n)C^{11}$ was measured from 53 to 1610 MeV by bombarding targets of plastic scintillator with pions. The intensity of the pion beam was monitored with a two-counter telescope and 40 Mc scaling system. The scintillator target was mounted on a phototube and became the detector for the C^{11} positron activity. Corrections were made for muon contamination in the beam, coincidence losses in the monitor system, C^{11} activity produced by stray background at the accelerator, C^{11} activity produced by secondaries in the target, and the efficiency of the C^{11} detection system.

The $C^{12}(\pi^-,\pi^-n)C^{11}$ cross sections rise to a peak of about 70 mb at 190 MeV, which corresponds to the resonance in free-particle π^-n scattering at 190 MeV. Calculations based on a "knock-on" collision mechanism and sharp-cutoff nuclear density reproduce the shape of the experimental excitation function, but the magnitudes of the calculated values are low by a factor of six. The calculation shows that the $C^{12}(\pi^-,\pi^-n)C^{11}$ reaction occurs in the nuclear surface region at all bombarding energies. The contributions to the (π^-,π^-n) reaction

predominate on the front surface of the nucleus in order to give the pion the maximum probability of escaping.

The excitation functions for the reactions $Zn^{68}(p,2p)Cu^{67}$ and $Fe^{57}(p,2p)Mn^{56}$ were measured radiochemically from 400 MeV to 6.2 GeV. The slight increase in the (p,2p) cross sections measured from 400 to 720 MeV is related to the occurrence of a quasi-free-particle pp collision within the nucleus. Due to the proton momentum distribution, the increase is not as pronounced as the rise in free-particle pp total cross sections from 400 to 1000 MeV.

From 2.2 to 6.2 GeV, the $Zn^{68}(p,2p)Cu^{67}$ and $Fe^{57}(p,2p)Mn^{56}$ cross sections are constant at 21 ± 2 mb and 50 ± 8 mb, respectively. The difference in magnitudes of the (p,2p) cross sections is ascribed to the availability of only two protons in Zn^{68} and of six protons in Fe^{57} for this particular reaction.

The free-particle effects are not seen in more complex reactions as evidenced by the constant cross sections from 0.72 to 6.2 GeV for the yields of Mn^{51} and Mn^{52} from the reactions of protons with iron and for the yields of Cu^{61} and Cu^{64} from the reactions of protons with zinc.

Cross sections are presented for a few products from pion-induced reactions requiring several nucleons to be emitted. The yields of Mn^{56}, Mn^{52} and Fe^{52} from the bombardment of natural Cu by π^-, the yields of Cu^{67}, Cu^{64}, Cu^{61}, Mn^{56} and Mn^{52} from the π^- bombardment of natural Zn, and the cross section for Na^{24} from $\pi^- + Al^{27}$ are compared to the yields for similar reactions induced by protons. At the high energies considered here, interaction of a π^- with these targets is shown to give yields that are of the same order of magnitude as the yields from proton reactions. These results are interpreted as experimental evidence that pion processes are very important for energy transfer in high-energy nuclear reactions.

NUCLEAR REACTIONS INDUCED BY PIONS AND PROTONS

Paul L. Reeder

Lawrence Radiation Laboratory and Department of Chemistry
University of California
Berkeley, California

November 27, 1962

I. INTRODUCTION

Knowledge of the π meson has been considerably increased since Yukawa first proposed that a particle of about 300 electron mass units (m_e) was responsible for nuclear forces.[1] His theory stated that the attractive forces between nucleons were a result of the exchange of this particle from one nucleon to another. Nucleon attraction between nn, pp, and pn pairs required the existence of strongly interacting particles with positive, negative, and neutral charges. The experimental confirmation of this hypothesis came in 1947 with the discovery of π mesons in cosmic rays at high altitudes.[2] In 1948, π mesons were produced artificially for the first time at the Berkeley 184-inch cyclotron.[3] Since then the properties and behavior of π mesons have been investigated in a great variety of experiments. The π meson acquired the name pion to distinguish it from the μ meson, or muon, which was discovered in cosmic rays in 1936. Charged pions have a mass of 273 m_e, whereas the neutral pion has a mass of 264 m_e. The charged pions are unstable and in free space decay with a mean lifetime of 2.55×10^{-8} sec. The decay products are charged muons and neutrinos (ν):

$$\pi^{\pm} \rightarrow \mu^{\pm} + \nu.$$

Pions interact strongly with matter and these interactions have been intensively studied in recent years. Much of the work has been concerned with the interactions of pions and free nucleons as a means of studying the nuclear force. For pions striking free nucleons, the possible interactions are elastic scattering, charge-exchange scattering,

inelastic scattering (particle production), and absorption. Absorption of a pion by one nucleon takes place with the emission of one high-energy γ ray to conserve energy and momentum. Cloud chambers, counters, bubble chambers, and recently, spark chambers have been the most common experimental techniques for studying these interactions. From this work there is now information on total πN cross sections, elastic πN cross sections, inelastic and charge-exchange cross sections, angular distributions of all kinds of πN scattering, and polarization effects in πN scattering. Properties of this type are best studied with liquid-hydrogen targets, in order to eliminate the complicating effects of nuclear binding and scattering from the nucleus.

However, it is also of interest to study the reactions of pions with nuclear matter and specific nuclei. Here the pions still undergo the previously mentioned scattering processes. In the absorption process, however, the π rest-mass energy is converted into nucleon and nuclear excitation and the high-energy γ ray is not seen. The techniques mentioned before are not conducive to studying the residual nuclei after a pion interaction has taken place. Nuclear emulsions have been useful for studying pion reactions in heavier nuclei. However the recent increase in pion-beam intensity has now made it feasible to study pion-induced nuclear reactions by radiochemical techniques. The main advantage of radiochemistry is that yields of specific nuclei can be measured rather than yields of emitted particles.

A brief mention of some of the notations employed throughout this report is necessary here. A nuclear reaction is often symbolized by (a, bc) where a represents the incident particle, and b and c are the particles leaving the struck nucleus. The quantity $\sigma(pp)$ represents the total cross section for scattering of free protons by incident protons. Likewise, $\sigma(pn)$, $\sigma(\pi^- p)$, $\sigma(\pi^- n)$ all stand for free-particle total cross sections. The symbol πN is used to mean pion collisions with nucleons in cases where collisions with both nucleon charge states are allowed.

Because of low-intensity beams, previous radiochemical experiments were limited to studying only the reactions of pions after they were stopped in large quantities of target material.[4,5,6,7] This meant that only the yields from the absorption of very low-energy pions could be obtained. Because relatively large intensities of high-energy pion beams are now available, it is possible to use thinner targets so that the pions do not lose an appreciable amount of their energy in passing through the target. Thus we can study nuclear reactions caused by high-energy pions, and make direct comparisons with similar reactions caused by high-energy protons. The experiments reported here provide information not only on high-energy pion absorption processes, but also on direct πN collision events within nuclear matter. This latter information gives unique proof of the validity of the impulse approximation for pion-nucleon collisions within nuclear matter.

Since much of this report is concerned with free-particle-like collisions within nuclear matter, the free-particle total cross sections are presented in Appendix A for pp, pn, π^+p, and π^-p scattering. From the principle of charge symmetry, we take the nn cross sections to be equal to the pp cross sections. Likewise, the π^-n cross sections equal the π^+p cross sections, and the π^+n cross sections equal the π^-p cross sections.

Pion-nucleon scattering has a unique feature not present in nucleon-nucleon scattering—that is, the large resonance peak at an incident pion energy of 190 MeV. It is this resonance peak that makes it possible to identify πN collisions within nuclear matter.

The specific reaction studied here was the $C^{12}(\pi^-,\pi^-n)C^{11}$ reaction. Cross sections were measured as a function of energy through the free-particle resonance region. The existence of a peak in the (π^-,π^-n) excitation function is interpreted as a direct result of a πN collision within the C^{12} nucleus.

The free-particle pp cross sections exhibit a rise over the energy region of 400 to 1000 MeV. Additional evidence for free-particle-like collisions in nuclear matter is discovered in the excitation functions for (p,2p) reactions on Zn^{68} and Fe^{57}. The (p,2p) cross

sections show increases which follow the increase in the free-particle pp cross sections, in distinct contrast to (p,pn) cross sections, where no such increase is expected from the free-particle pn cross sections.

A limited amount of data is presented for nuclear reactions following high-energy pion absorption. Pion fluxes are still considerably below fluxes of proton beams—making it necessary to use relatively thick targets. This in turn complicates the radiochemical technique. However, the combination of low-background beta counting and "bucket" - type (large volume) chemistry permitted the study of a few products from pion bombardments of Al, Cu, and Zn. Comparison of these yields with similar yields for proton bombardments shows that there are only minor differences.

The greater accuracy obtained in the experiment for the $C^{12}(\pi^-,\pi^-n)C^{11}$ reaction is due to the use of a nonchemical technique for identifying the C^{11} radiation. The C^{12} targets were made of plastic scintillator which, after irradiation with pions, became the detector for the positrons from C^{11}. This technique gave a high detection efficiency and 100% chemical yield.

II. $C^{12}(\pi^-,\pi^-n)C^{11}$ EXPERIMENT

A. Meson Beams at the 184-Inch Cyclotron

The excitation function for the reaction $C^{12}(\pi^-,\pi^-n)C^{11}$ was measured experimentally by using the pion beams available at the 184-inch cyclotron. Targets of plastic scintillator were bombarded with a monitored beam of pions; the amount of C^{11} produced was determined by following the decay of C^{11} by positron counting.

Beams of pions at the 184-inch cyclotron are obtained by bombarding a Be or C target with the full-energy internal proton beam. Since pions have a different charge-to-mass ratio than protons have, the cyclotron magnetic field bends the pions out of the cyclotron vacuum tank through a thin Al window. A quadrupole magnet called "Selrex" is located just outside the window to focus the pions through an 8-ft-diam iron wheel which allows the pions to enter the experimental area called the "meson cave." Since different-energy pions come out at different positions along the Al window, the quadrupole magnet may be rolled along a track and the iron wheel turned to various angles in order to obtain different-energy pion beams. Once the pions reach the meson-cave area, the beam path is at the discretion of the experimenters. The experiments reported herein were performed by using the pion beams set up by many different physics-groups at the 184-inch cyclotron. All of the beam setups involved the use of a bending magnet for momentum selection and another quadrupole magnet for focusing, once the beam reached the meson-cave area. When possible, irradiations of the plastic targets were conducted simultaneously with the experiments of the physics-groups. A typical physics-group experiment would involve bombardment of a liquid-hydrogen target with pions and the measurment of the scattering at various angles around the target. The main pion beam would pass through the H_2 target at 0 deg and would be available for irradiating chemistry targets. The beam setup for the 380-MeV π^- beam is typical of many of the experiments, and is shown in Fig. 1. The

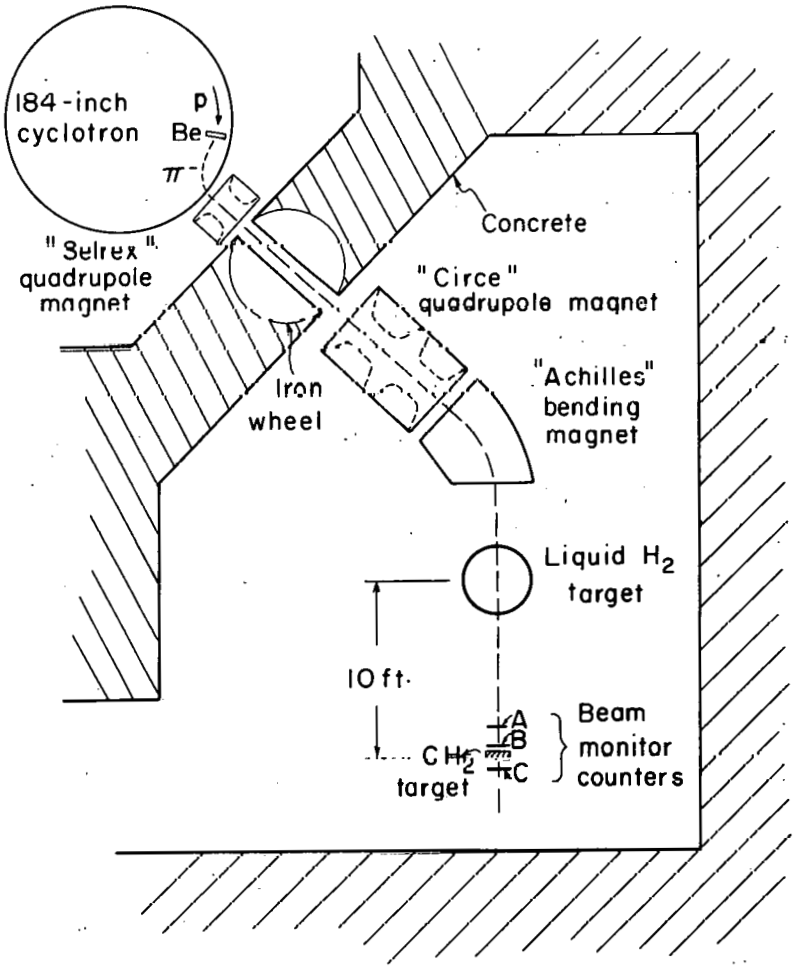

Fig. 1. Experimental setup at 184-inch cyclotron for 380-MeV π^- beam.

beam-monitor counters for the chemistry targets are shown behind the liquid-hydrogen target used in the physics experiment.

The pion energies at the quadrupole focus were determined by the physics group involved, by means of wire orbit analysis of the bending magnet and by range curves in Cu and CH_2. The range curve also gave information on the composition of the beam. The bending magnets could not eliminate particles that have the same momentum as the pions, so all the π^- beams contained μ^- and e^- as contaminants. The correction for this contamination is discussed in Sec. II-C. Usual running conditions were such that the momentum spread of the pion beam was from 1 to 3% for pion energies greater than 200 MeV. At 127 MeV the beam momentum spread was about 7%. At lower energies the momentum spread may have been as much as 10%, due to the use of absorbers before the bending magnet to degrade the beam energy. From the energy of the pions at the center of the physics target or at the magnet focus, the energy of the pions at the midpoint of the plastic scintillator targets was calculated by using the energy-loss tables of Rich and Madey.[8] The calculation takes account of the fact that the pions had to pass through the back half of the physics target, a finite distance of air, the beam-monitor counters, and the first half of the target itself. Since the plastic scintillator targets were thick enough (1 in.) for the pions to lose an appreciable amount of energy in passing through the target itself, the energy drop in the target was combined by root-mean-square addition with the energy spread of the beam to determine the overall energy spread.

B. Beam-Monitoring System

1. Monitor Counters

The pion beam was monitored, as shown in Fig. 2, with two plastic scintillator detectors attached by lucite light pipes to RCA 6810A photomultiplier tubes. A third counter was used as a beam monitor while running plateau curves and delay curves. The dimensions of each counter and light pipe are given in Table I.

Table I. Dimensions of monitor counters.

Counter	Type	Surface dimensions (in.)	Thickness (in.)
A	Square	3.50 × 3.50	0.25
B	Circular disk	2.50 diam	0.25
C	Circular disk	2.50 diam	1.00

The targets were attached to the back side of counter B and had the same diameter so that counter B defined the beam size. The actual beam spot at the focus of the quadrupole is usually an ellipse with a major axis comparable to the size of counter B. However, since the monitor counter telescope was generally several feet beyond the focus of the quadrupole, the beam was diverging at the location of the counters and filled an area larger than counter B. It is assumed that all pions passing through counter B also passed through the target. Counter A was made larger than counter B, to minimize the need for extremely accurate alignment. Thus it is assumed that any pion passing through counter B must have passed through counter A also. All three counters were mounted about 6 to 8 in. apart on an Al frame in such a manner that they could be adjusted to meet varying conditions of space and beam height.

The plastic scintillators and light pipes were wrapped with Al foil to act as reflectors and then wrapped with black tape to eliminate

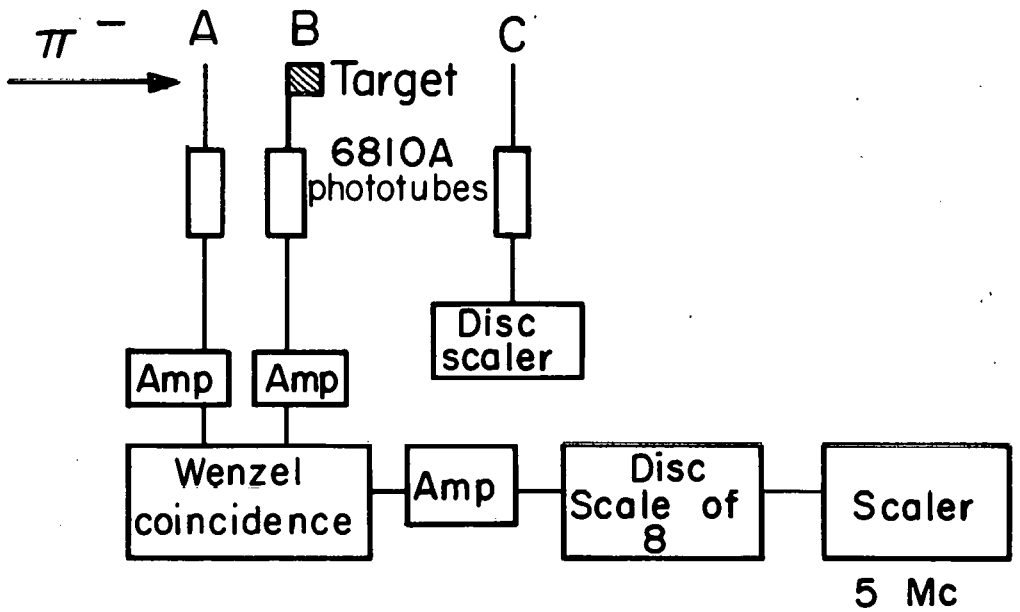

Fig. 2. Electronics for 40-Mc beam-monitor system.

all light leaks. The Al foil and tape were neglected in computing the energy loss for the pion to reach the target. Whenever possible the center of each counter was aligned with the 0-deg pion-beam line with the aid of a transit.

The photomultiplier-tube bases for counters A and B were designed for use with high-intensity beams.[9] Each of the last five dynodes is supplied with a separate voltage from a voltage-divider panel. The voltage is stabilized on each output by a cathode follower. This reduces the possibility that an intense burst of particles will cause the pulse output to sag because of too much current being drawn from the dynode voltage supply.

The tube base for counter C was a standard high-current tube base without the extra feature of voltage stabilization for the last five dynodes.

2. Electronics

The pulses from counters A and B were led through 125-Ω transmission lines to the meson counting area where they were each amplified by a Hewlett-Packard (H.P.) 460A distributed amplifer. The amplifier outputs were fed into a tube-type Wenzel coincidence unit equipped with 4-nsec clipping lines. This meant the resolving time was 8 nsec for a coincidence event. The lowest energy π used in this experiment was 50 MeV, and the distance between counters A and B was usually about 20 cm; the time required for a π to travel between the two counters was therefore about 1 nsec. Any fluctuation about this time would be well within the resolving time of the coincidence unit. The chance that two particles pass through the two counters within the resolving time is discussed under corrections to beam monitor in Sec. II-C-1.

The output of the coincidence unit was amplified by two H.P. distributed amplifiers, then led to a discriminator and scale-of eight.[10] This unit emitted one pulse for every eight input pulses above the discriminator setting. When connected to a 5-Mc scaling circuit, the scaling system was rated at 40 Mc— which was necessary in order to count the pion beam directly.

Pulses from counter C were inverted and used without amplification to drive a discriminator and 5-Mc scaling circuit. The counts from C were used only in normalizing data while conditions were being adjusted for the A-B system.

3. Operation

The first step in operating the beam-monitoring system consisted of setting the gains of the two channels of the coincidence unit to give the same pulse output for a given pulse input. A delay curve was obtained by inserting various lengths of cable before one input to the coincidence unit. The counting rate should be constant as long as the two pulses come within the resolving time of the coincidence unit. The shape of the delay curve gives an indication of how well the system is operating. A typical delay curve is plotted in Fig. 3. Each point was obtained by taking the coincidence counting rate of A + B for a fixed number of counts in counter C at a given delay setting.

Another check on the system could be made by plotting the coincidence counting rate A + B as a function of the high voltage or gain of one counter while holding the voltage or gain of the other counter constant. A typical plot of this line is shown in Fig. 4.

The final check on the monitor system was performed by plotting the counting rate as a function of the discriminator setting of the scale-of-eight unit. This curve should be quite flat, as shown in Fig. 5. All data were taken for a fixed number of counts in counter C.

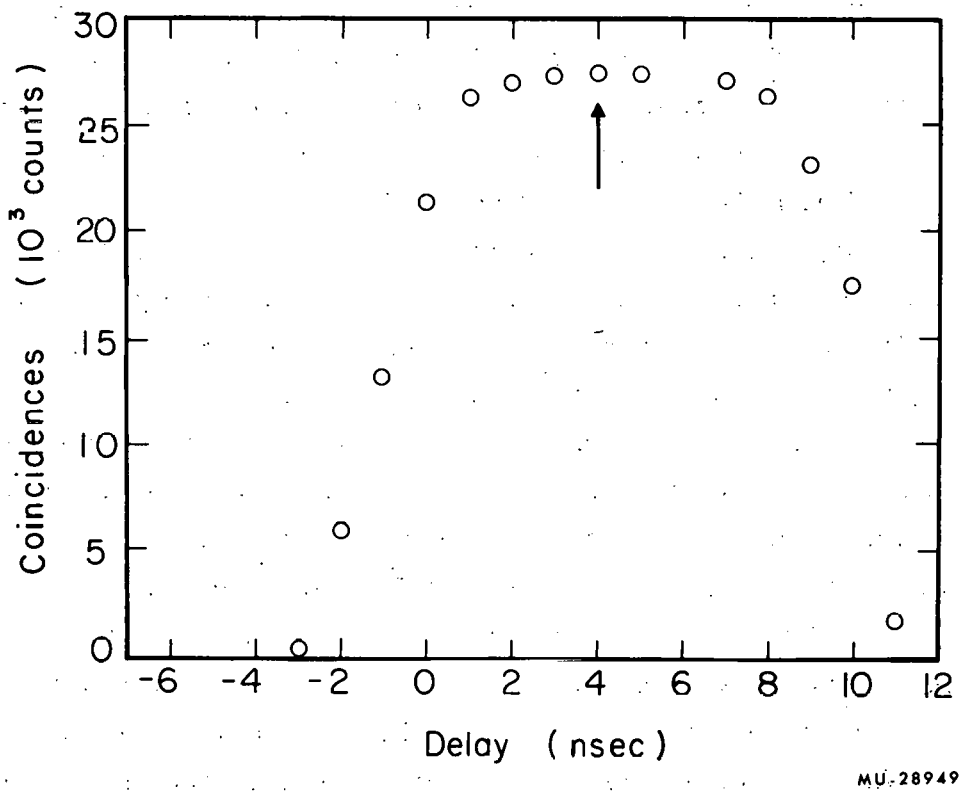

Fig. 3. Delay curve for beam-monitor system. (The arrow represents the optimum operating point.)

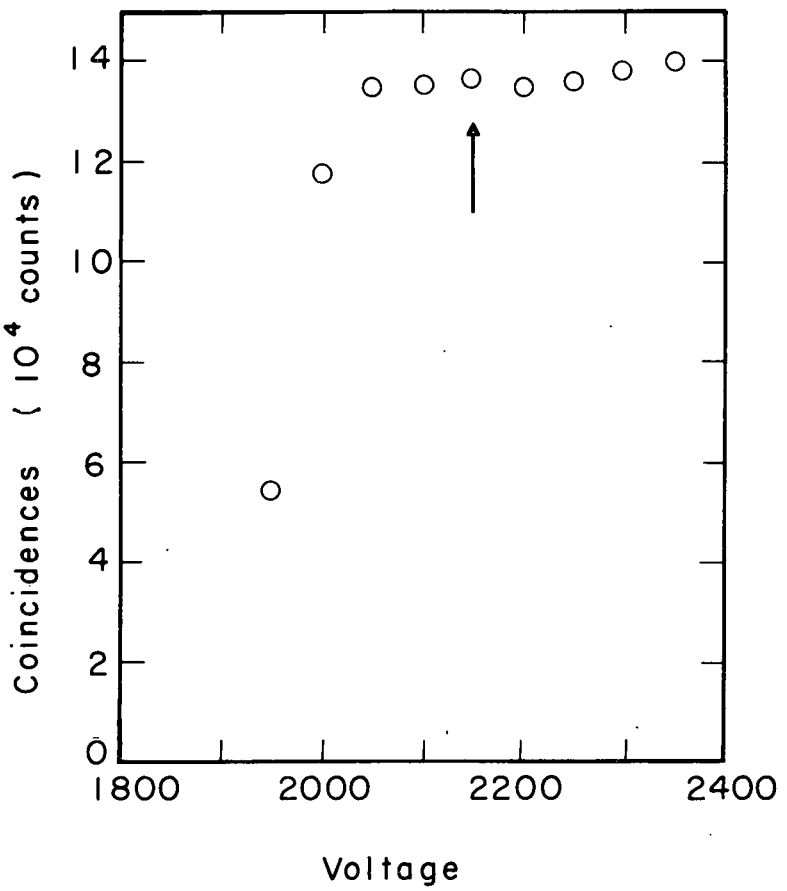

Fig. 4. High-voltage curve. The coincidence counting rate of counters A and B is plotted vs the voltage for counter A. Counter B voltage is constant. (The arrow represents the optimum operating point.)

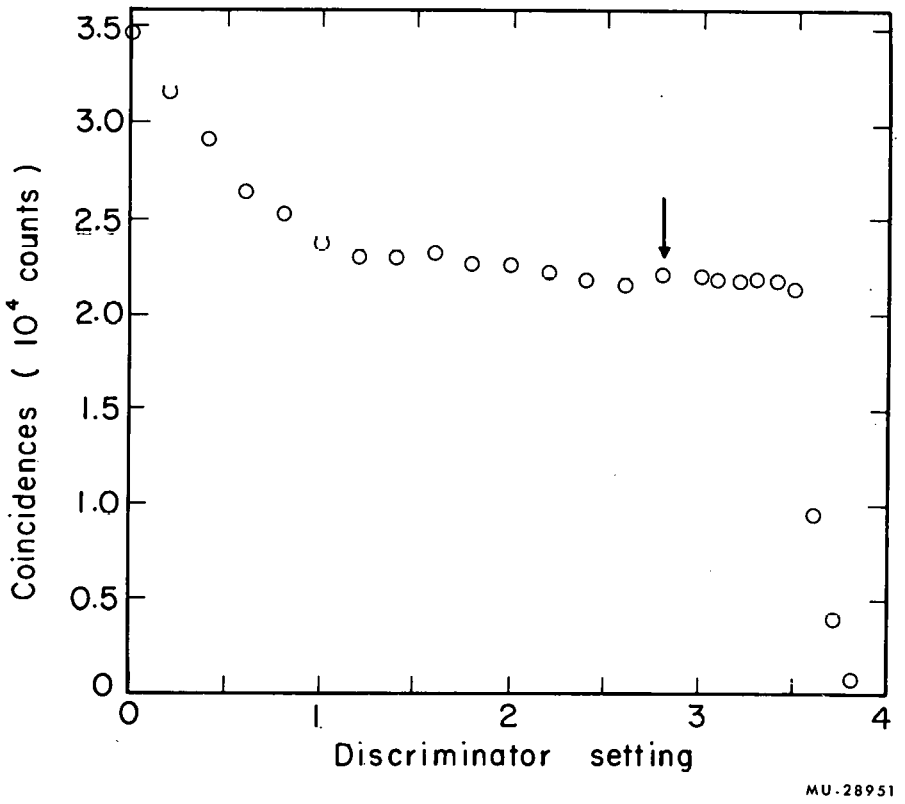

Fig. 5. Discriminator curve. A and B coincidence counts plotted vs discriminator height (arbitrary units).

C. Corrections to Beam Monitor

1. Accidentals

The total number of coincidence counts from counters A and B divided by the counting time does not give the particle intensity directly. Even with the high-speed counting equipment used, the average counts/min must be corrected for coincidence losses. These losses occur when two or more pions pass through the counter telescope simultaneously. The internal proton beam of the 184-inch cyclotron has a great deal of time dependence inherent in normal operation. The beam comes at the rate of 64 bursts/sec with each burst lasting about 400 μsec. Within each burst of 400 μsec, there are fine structure pulses, "fsp", of 13 nsec duration which come 54 nsec apart. The duty cycle which defines the percentage of the time that particles actually are passing through the counters, can be calculated as follows.

$$\text{Duty cycle} = (\text{No. of fsp/sec})(\text{Time of one fsp})$$

$$= \left(\frac{400\ \mu\text{sec/burst}}{54\ \text{nsec/fsp}}\right)\left(\frac{64\ \text{burst}}{1\ \text{sec}}\right)\left(\frac{13 \times 10^{-9}\ \text{sec}}{\text{fsp}}\right) = 0.6\%$$

For a typical average beam of 10^6 π/min, the instantaneous counting rate $= (10^6\ \pi/\text{min})\ \left(\frac{1}{0.006}\right)\ \left(\frac{1\ \text{min}}{60\ \text{sec}}\right) = 2.7 \times 10^6\ \pi/\text{sec}$.

The coincidence loss or "accidentals" can be estimated by dividing the instantaneous counting rate by the counting capacity of the beam-monitor system.

$$\text{Acc. (short spill)} = \frac{2.7 \times 10^6\ \pi/\text{sec}}{40 \times 10^6\ \text{pulses/sec}} = 6.7\%$$

for these conditions the experimentally observed accidentals rate agreed roughly with this number.

Although the beam is more difficult to obtain, the 400 μsec burst can be "stretched" to about 10 msec which means a duty cycle of about 15%. For an average beam intensity of 10^6 π/min, the accidentals for a stretched beam is about 0.3%. The experimental accidental-percentage is somewhat higher than this figure because even with the stretched beam, approximately 30% of the beam still comes in the 400 μsec "spike". The fractions of the beam in the spike and in the stretched beam vary widely depending on the cyclotron operating conditions and operators, so that the accidental counting rate must be determined for each target bombardment.

The fine structure pulse of 13-nsec duration is of the same magnitude as the resolving time of the coincidence unit. In most cases only one pion per fine structure pulse is expected. However, an empirical method was used to determine the probability of two pions appearing in the same fine structure pulse. It was assumed that this probability was equal to the probability of counting one particle in one pulse and another particle in the next pulse 54 nsec later. Experimentally this means that the number of simultaneous pions was determined by adding 54-nsec delay to one of the counters before the pulse reached the coincidence unit. Counting rates with the 54 nsec delay were usually taken just before target runs at the same beam level as the actual run. This coincidence rate was added to the rate for the target bombardment determined with normal delays. With the beam levels ordinarily obtained during these experiments, the correction for accidentals did not exceed 10% of the beam intensity. A plot of total counts (monitor plus accidentals) vs internal-proton-beam intensity was taken during short spill operation. This plot is shown in Fig. 6. Assuming that the number of pions through the counter telescope is linearly related to the internal-proton-beam intensity, the deviation of the solid curve from a straight line shows when saturation and voltage sag begin to affect the counters.

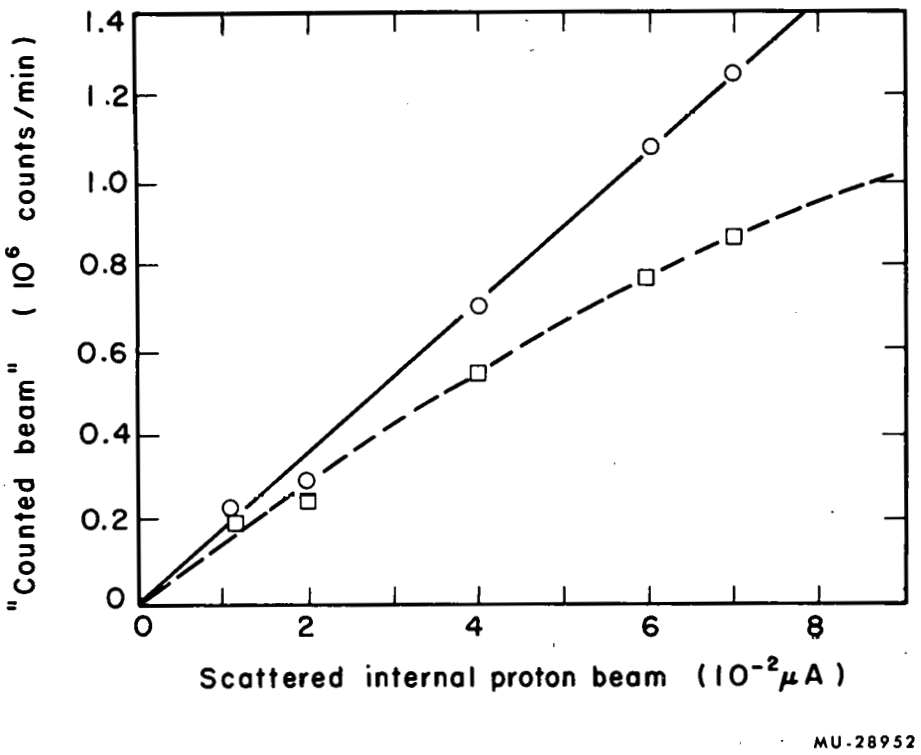

Fig. 6. "Counted beam" versus internal beam. Dashed curve is the uncorrected total counts in telescope. Solid curve is the sum of uncorrected total counts and "accidentals" as defined in the text.

Targets were always bombarded with beam intensities such that the sum of monitors plus accidentals was still on the linear part of the plots.

2. Muon Contamination

The largest correction to the beam-monitor intensity comes from the contamination of the beam with μ mesons. The π^- meson decays to $\mu^- + \nu$ in free space with a mean life $\tau = 2.55 \times 10^{-8}$ sec.[11] This decay is isotropic in the c.m. system. The kinetic energy in the center of mass of the decaying pion is 4.14 MeV. The μ^- interacts with nucleons just like a heavy electron because it undergoes weak interactions.

Several experiments were tried to see if μ^- could produce C^{11} from C^{12} by elastic scattering of the muon and neutron. All of these experiments gave negligible amounts of C^{11} activity, but because of low μ-beam intensities, an upper limit of about 1.6 mb was placed on the probability of C^{11} production by negative muons. Although the muons (likewise any electrons in the beam) did not contribute to C^{11} production, the muons were counted by the counter telescope. There were two components to the muon contamination, depending on whether the $\pi - \mu$ decay occurred before or after the bending magnet. For decays occurring before the magnet, the magnet separates all μ's with momentum different from that of the beam pions, but those muons with the same momentum could not be eliminated. A differential range curve in Cu or CH_2 after the bending magnet gave the relative number of pions, muons, and electrons having the same momentum in the beam. Data taken by the physics groups were used in all cases. However, a range curve taken simultaneously with the Crowe group during a π^+ beam-study experiment is shown in Fig. 7. The differential range curve computed from these data is also given and shows the peaks due to pions and muons.

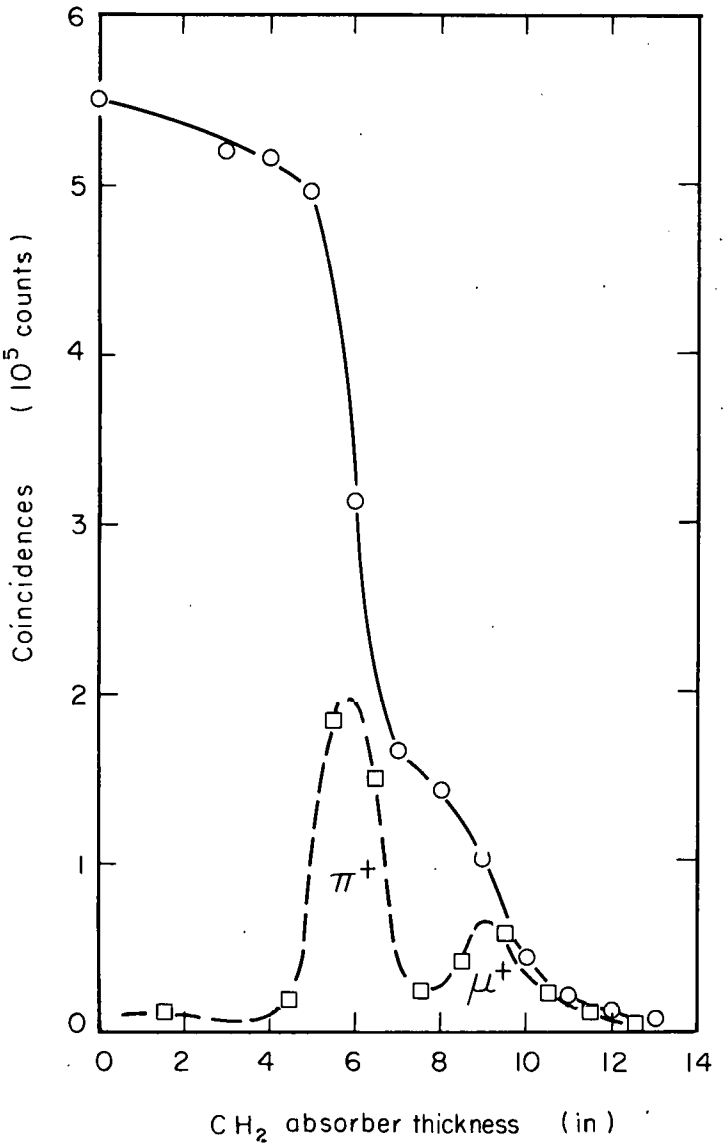

Fig. 7. Range curve for 73-MeV π^+ beam. Solid curve is coincidence counting rate vs absorber thickness. Dashed curve is differential range curve.

For pions that decay to muons after the bending magnet there is no momentum selection. Thus muons of any energy may be accepted by the counter telescope, provided that the muons are within the solid angle subtended by the telescope. The fraction of the muons in the beam from this source is not easily measured but can be calculated to a high degree of accuracy. (See Appendix B for the detailed calculation of this correction.) The total muon contamination varied from about 40% of the total beam at 50 MeV to about 8% at 373 MeV.

D. Beam Studies

1. Beam Profiles with π^+ Beam

One set of measurements was performed by using the 123-MeV π^+ beam set up by Bingham and Kruger. The experimental setup made it necessary to place the counter telescope between the quadrupole magnet "Circe" and Bingham's target. The current settings for the doublet quadrupole magnet Circe were calculated by using the method described by Chamberlain in order to obtain a focus at the counter telescope.[12] The spatial distribution of the pion beam at the focal point of Circe for these current settings was checked by taking beam-profile curves. The beam profiles were measured with a two-counter telescope consisting of 1-cm^2 plastic scintillators. The telescope was mounted on a motor-driven frame and could be moved horizontally or vertically across the beam by remote control from the counting room. The coincidence counting rate as a function of distance across the beam is shown for the vertical direction in Fig. 8a and for the horizontal direction in Fig. 8b. By taking the full width at half maximum (FWHM) as the criterion for describing the beam, the area of the beam was found to be

$$\text{Area} = \pi ab = \pi\,(3.05)(1.35) = 12.9\ \text{cm}^2.$$

The beam shape at counter B was an ellipse with major axis 6.1 cm and minor axis 2.7 cm. The total area within the FWHM was 12.9 cm^2, whereas the total area of counter B is 31.7 cm^2. However, only 72% of the beam is included under the FWHM. Because the horizontal distribution was so broad, some of the remaining 28% of the beam missed counter B. For this experiment counter A was a 2.5-in.-diam 1-in.-thick plastic. The area of the FWHM beam at counter A was larger than counter A itself, so that approx 83% of the beam passing through

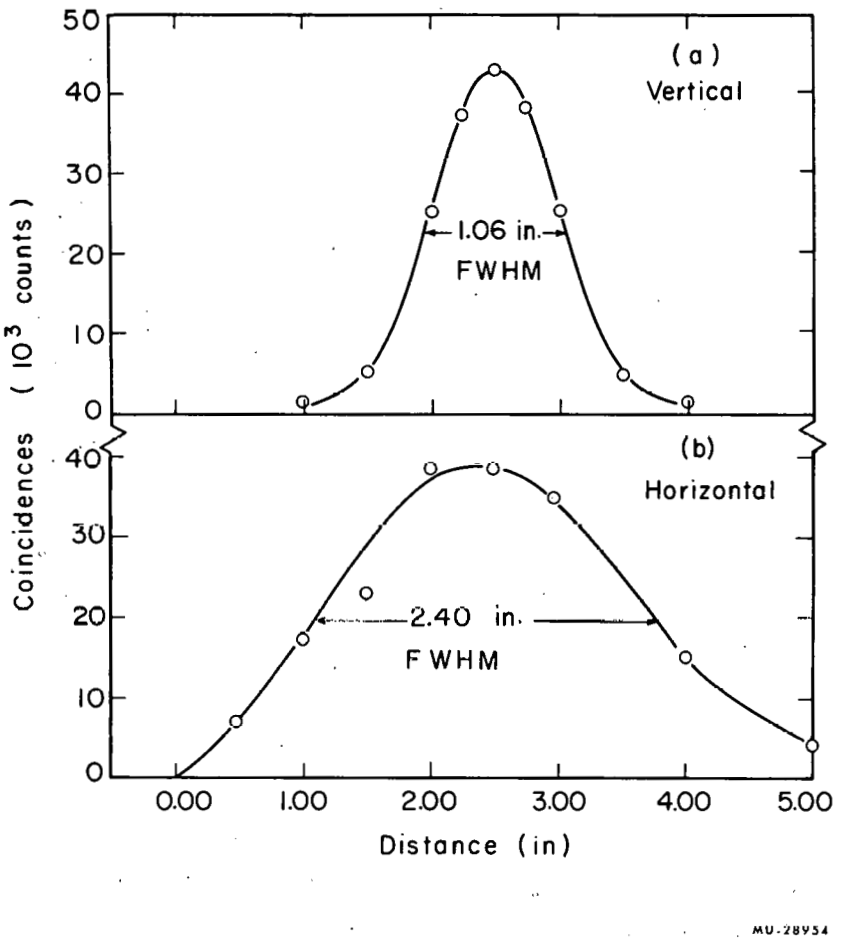

Fig. 8. Beam profiles. The coincidence counting rate is plotted vs the distance across the beam.

(a) Vertical distance.

(b) Horizontal distance.

B missed counter A. This number was determined by geometrical calculations and checked with the ratio of A + B coincidence counts to B singles counts. Therefore, for this experiment only, the singles counting rate of B was used as a monitor of the beam intensity, whereas in all successive experiments the coincidence counting rate of A + B was used as the beam monitor. The experiment with π^+ involved a situation in which the pion beam was converging in moving from counter A to counter B. However, in all subsequent experiments the pion beam was diverging with respect to counter A and counter B because of the location of the counter telescope beyond the focal point of the quadrupole magnet. The use of a larger area for counter A in subsequent experiments also made it impossible for a pion to reach counter B and the target without passing through counter A.

2. Ion Chamber

During the preliminary experiments with 380- and 130-MeV π^- beams, an ion chamber with an effective diameter of 4 in. was used to monitor the beam. This ion chamber was similar to one described by Chamberlain et al.[13] and was connected to an electrometer voltmeter which integrated the current collected in the ion chamber. The electrometer-voltmeter output drove a chart recorder to give a permanent record of the beam intensity. The multiplication factor for converting total charge collected by the ion chamber into the number of pions passing through the chamber is given by

$$M = \frac{t}{w}\left(\frac{dE}{dx}\right) ,$$

where

$\frac{dE}{dx}$ = the rate of energy loss per g/cm^2 for a given energy π in the 96% argon, 4% CO_2 mixture,

t = the surface density of the gas in g/cm^2, and

w = 25.5 eV/ion pair, as determined by Chamberlain at 345 MeV.

Then M gives the number of ion pairs per incident pion.

At 380 and 130 MeV, an 8-in.-thick Cu collimator with a 2-in.-diam hole was placed in front of the ion chamber. The targets were taped to the back side of the ion chamber. The cross sections measured in this fashion agreed to about 10% with the cross sections measured with the counter-telescope monitor at 380 MeV. For consistency, the ion-chamber data at 373 MeV were not included. However, because no counter-telescope data were available at 127 MeV, the ion-chamber cross sections were included in the excitation function.

The ion-chamber data are not expected to be as accurate as the counter data because the ion chamber did not define the beam through the target, and because the Cu collimator adds a great number of scattered particles to the beam.

3. Film Study

At 127 MeV, Polaroid film (type 57, with a speed rating of 3000) was taped over the downstream opening of the quadrupole magnet to determine the distribution of π^- through the magnet. The exposure time was about 15 min. The pictures indicate that the pions (and other charged particles, μ^- and e^-) fill the entire opening, which has a 4-in.-radius, but most of the intensity is apparently within a 3-in.-radius circle. This information is useful in determining the maximum beam angle at the focus. Polaroid film placed behind the ion chamber, which itself was about halfway between the quadrupole magnet and its focal point, gave a radiograph (pionograph?) of the ion chamber, but no information about the distribution of the beam.

E. Bevatron Experiment

At the outset of this work, a few experiments were performed at the Bevatron by using the 1.75-GeV/c π^- beam set up by Segrè group to study pion-pion interactions.[14] After sufficient magnetic analysis and focusing, the 1.75-GeV/c pion beam passed through a liquid-hydrogen target. The 2.5-in.-diam. chemistry targets were placed behind the physicists' beam-monitor counter and irradiated for a known number of Bevatron pulses. The Segrè-group experimenters supplied the number of pions per pulse through a 4-in.-diam circle[$(1.1 \pm 0.1) \times 10^4$ π/pulse]. An oscilloscope display of the horizontal distribution of the pion beam showed that most of the pion beam would strike the 2 1/2-in.-diam plastic scintillator target.

Two bombardments were performed with this experimental setup. In the first run, the background in the β^+ detection system completely hid the C^{11} decay. After lowering the background a second run was performed. For this bombardment the initial activity of C^{11} was about equal to the background of about 135 counts/min and could be resolved with an accuracy of about 15%. When combined with the approx 20% error in the measurement of the pion intensity through the 2.5-in.-diam target, this gave an overall error of about 25% for this cross section.

F. Detection System for C^{11}

After irradiation at the accelerator, the plastic-scintillator targets were brought back to the chemistry building where detection equipment was arranged to follow the C^{11} decay. Targets were not counted at the cyclotron because of the large and erratic background at the accelerator. For each "run" at the cyclotron, the target was "run"down to the chemistry building. (Fortunately, this was all downhill.) The current course record for the cyclotron-to-chemistry-building dash was set at 3 min 25 sec from the time the beam was turned off to the time the β^+ counter was turned on.[15] This time was typically about 4 to 6 min which is only approx 1/4 of the C^{11} half-life.

The C^{11} detection system consisted of the plastic-scintillator target mounted on an RCA 6655A photomultiplier tube,[16] a White cathode follower, a DD2 linear amplifier, and scaler. (The photomultiplier tube base was enclosed in a 2-in.-thick lead cave which had a door for inserting the phototube with its scintillator and cover in place.) Figure 9 shows a block diagram of this apparatus. The plastic scintillator was attached directly to the phototube face with Dow Corning 200 silicone grease. An ice cream carton lined with Al foil to act as a light reflector and wrapped with black masking tape to seal out all external light, slipped snugly over the plastic scintillator and phototube. Mounting of the plastic scintillator and sealing of the system could be done in about 1 min. Various authors have noticed a short-lived "activity" of about 1.5 min when a plastic scintillator which has been exposed to light is sealed and "counted".[17] The background of about 135 counts/min in this counting system was too large to notice this effect. Any correction from this effect to the counting data would be included in the method used for determining the stray-particle background correction to be discussed in Sec. II I-1.

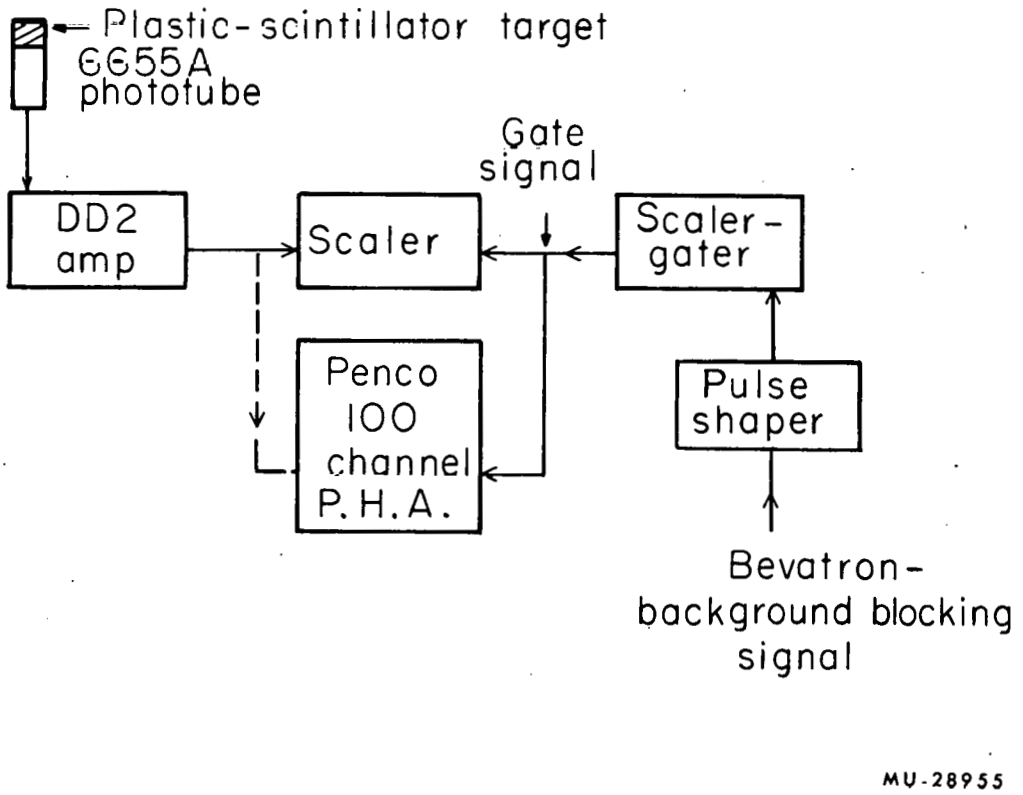

Fig. 9. Electronics for C^{11} detection system.

1. Blocking System for Bevatron Background

Although the counting area was located over 100 yards from the Bevatron, the background was greatly affected by whether the Bevatron was on or off. When the Bevatron was off the background in the C^{11} detection system was about 135 count/min, but when the Bevatron was on the background was about 230 counts/min. The Bevatron produces 10 pulses/min; each pulse lasts 1.75 sec. The Bevatron pulses could be seen by displaying the signals from either a NaI or plastic scintillator detector on an oscilloscope in the counting room. This meant that high-energy protons or neutrons were coming from the Bevatron and interacting in the detectors or Pb shields to produce the extra background.

The electronics group under the leadership of Duane Mosier, and later under George Kilianm, devised a system that allowed the C^{11} detector to be turned off during the short burst from the Bevatron. A positive 20-V dc bias was applied to a telephone line coming from the Bevatron to the chemistry building. At the start of the Bevatron accelerating cycle, this line was shorted to ground long enough to trigger a pulse in a scaler-gater. The scaler-gater unit puts out a 20-V gate signal after a preset delay, following the trigger signal from the Bevatron. The trigger signal starts (t=0) when the Bevatron "rf" field is turned on. The width of the gate and the length of the delay could be varied to cover the time interval during the Bevatron burst. The time of beam spill out of the Bevatron depends on the needs of the particular experiment in progress, so it was necessary to set the length of delay and width of gate pulse just before each C^{11} experiment.

A clock is connected to the on-off switch so that the total elapsed time can be measured with the scaler-gater also. The live time, which is the time during which the scaler is actually on, can be calculated if the number of Bevatron block signals received and

the length of each block pulse are known.

When the Bevatron is operated at low beam levels or on stretched spill out (the time during which the full-energy beam is striking the internal target) it is not possible to distinguish Bevatron bursts from normal background, so the scaler-gater system is not useful. However, when the Bevatron is operating normally at full beam, use of the scaler-gater can cut the background in the plastic scintillator detector by a factor of almost two, by using a block signal of about 0.2 sec in width. Since there are only 10 block signals per minute, the off-time of the counters is only 2 sec/min or about 3.3%.

2. Standardization

Because C^{11} emits positrons with a continuous spectrum of energies, the output signals from the linear amplifier have a continuous spectrum of pulse heights. Thus the discriminator setting of the scaler has a vital bearing on the detection efficiency of the system. By raising or lowering the discriminator level, one can decrease or increase the fraction of the positron spectrum accepted by the scaler. To ensure that the same fraction of the β^+ spectrum was accepted in all runs, an external Cs^{137} β^- source was counted before the run. The Cs^{137} source was made by evaporating 5 λ of standardized Cs^{137} solution onto an Al disk, and covering the source with Videne TC plastic film. This source could be placed inside the ice cream carton cover, giving almost 2π geometry and little thickness between source and detector. Standardization was achieved by keeping the discriminator of the scaler constant and adjusting the gain of the DD2 linear amplifier to give the same counting rate. Cs^{137} has a half-life of about 27 years and decays by β^- emission to the ground state and an excited state at 0.662 MeV.[18] Of the β^- decay, 92% is to the excited state and 8% to the ground state. The γ ray from the 0.662-MeV level is internally converted in almost 10%

of the decays. Thus the β^- spectrum of Cs^{137} consists of two β^- groups plus a sharp line due to the conversion electrons, e^-.

Beta spectra. The output of the linear amplifier could be sent to a Penco 100-channel pulse-height analyzer to display the spectrum of pulses from the plastic scintillator detector. The conversion line appears as a broad peak superimposed on the lower energy β^- spectrum, as shown in Fig. 10. In order to obtain the β^- spectrum shown in the figure, it was necessary to subtract the counts due to Compton scattering of γ rays which interact in the plastic. The Cs^{137} source was covered with enough Al to stop all the β^- particles (E_{max} = 1.2 MeV; range = 500 mg/cm^2 of Al) and was counted in the same manner as the uncovered source for the same length of time. The pulses from the covered source gave a spectrum for the Compton electrons from the 0.662-MeV γ ray. When this spectrum was subtracted from the spectrum for an uncovered source, the result was the true $\beta^- + e^-$ spectrum. The resolution of the conversion line of Ba^{137m} at 0.624 MeV was about 30%. (FWHM) The conversion line of Ba^{137m} was used to calibrate the pulse-height analyzer by adjusting the amplifier gain to place the conversion e^- peak in a given channel.

The C^{11} spectrum was also displayed on the pulse-height analyzer and is plotted in Fig. 11. The slope of the high-energy side of the beta spectrum when extrapolated to the base line gives a rough indication of the end-point energy. The β spectra of several isotopes were taken, and the end-point energies were determined by extrapolation of the slopes. These end-point energies, when plotted vs channel number, gave a rough calibration curve, as shown in Fig. 12. The isotopes used and their end-point energies are listed in Table II.

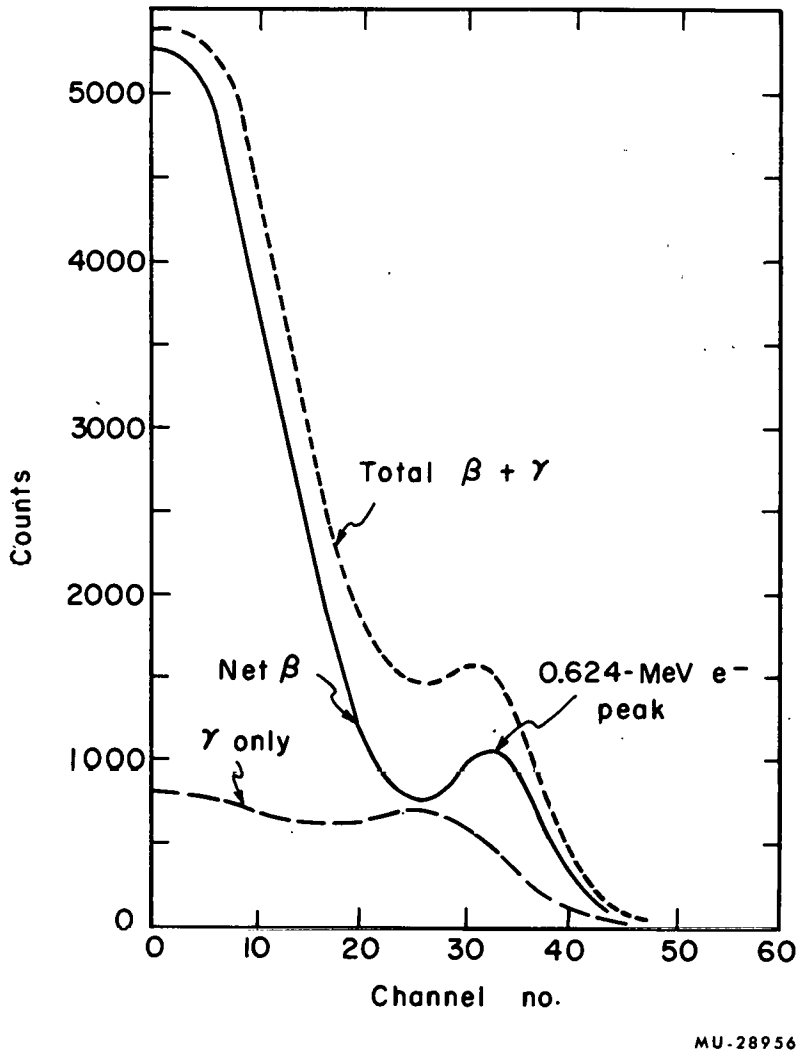

Fig. 10. Cs^{137} spectra in plastic scintillator (2π geometry). Dotted curve is total counts, dashed curve is background due to the 0.662-MeV γ ray, solid curve is net β spectrum showing the 0.624-MeV conversion peak.

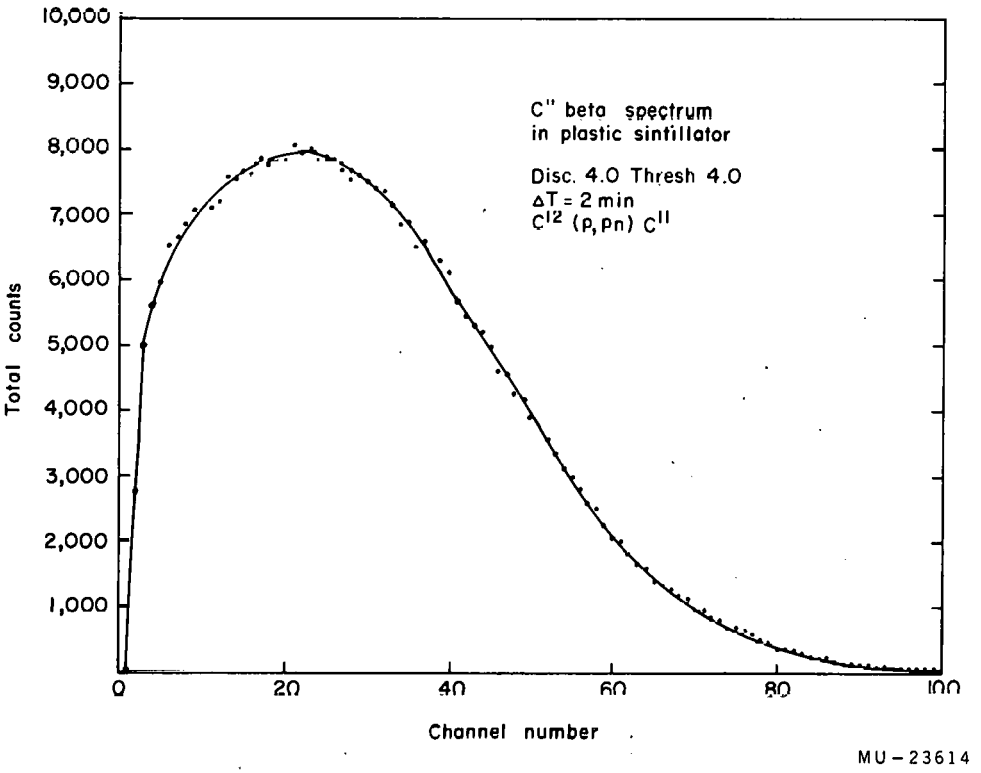

Fig. 11. C^{11} β spectrum in plastic scintillator. The arrow refers to the discriminator cutoff for the scaler.

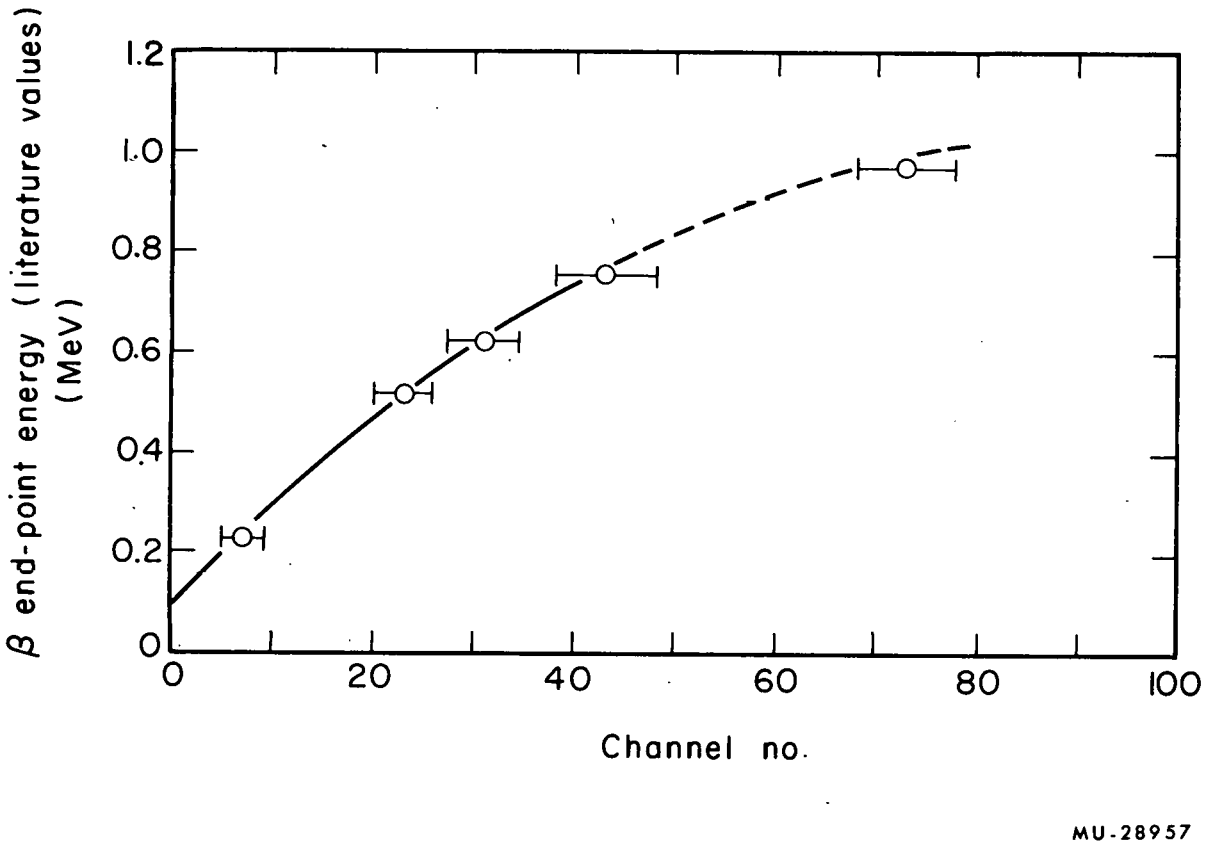

Fig. 12. Calibration curve for β spectra in plastic scintillator.

Table II. Standards for calibration curve.

Isotope	End-point energy (MeV)	Type
Pm^{147}	0.223	β^-
Cs^{137}	0.514	β^-
Ba^{137m}	0.624	Conversion e^-
Tl^{204}	0.764	β^-
C^{11}	0.968	β^+

The straight line for the internal C^{11} positron spectrum gives an end point in agreement with the calibration curve.

The use of the pulse-height analyzer with the plastic-scintillator detector is useful mainly to give a rough indication of the spectrum and end-point energy to prove that C^{11} was the isotope responsible for the observed activity. Further refinements in source mounting and γ-ray discrimination would permit greater accuracy in the use of plastic scintillator as a β spectrograph, as discussed by Bosch and Urstein.[19]

3. Decay Curve

Proof that the observed activity was actually due to C^{11} comes from the decay curve. Figure 13 shows the experimental decay curve obtained by bombarding the plastic scintillator with an especially intense pion beam. Once the constant cosmic ray background is subtracted there is only one component in the decay curve. The measured half-life of 20.4 min agrees with the literature value for C^{11}. Because the intensities of the available pion beams varied

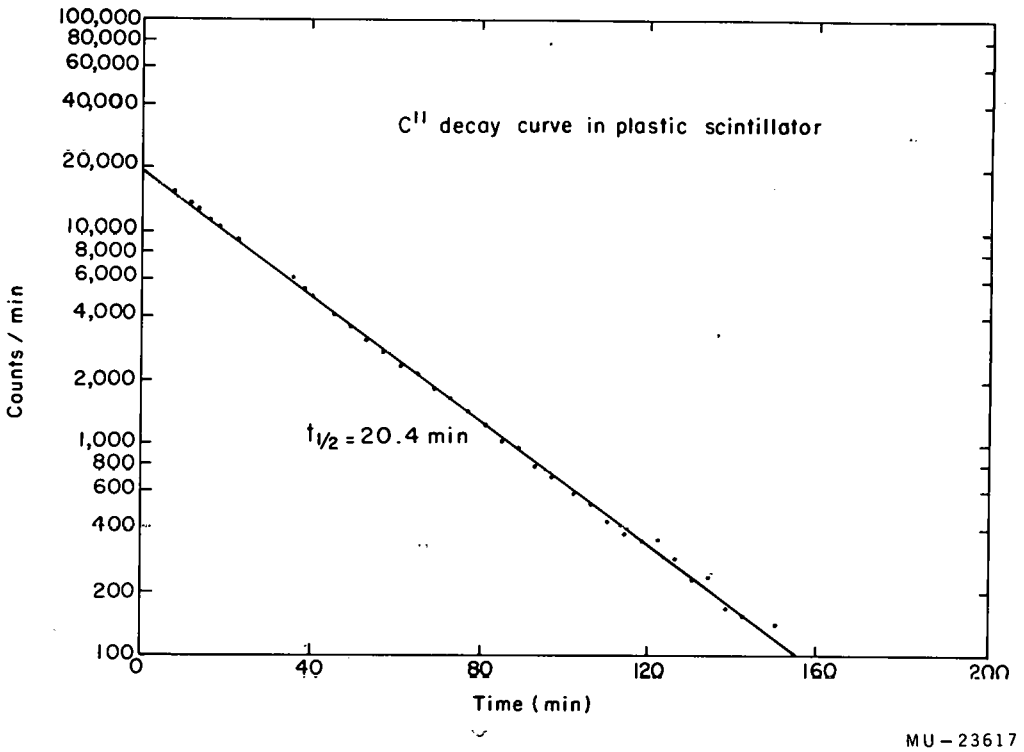

Fig. 13. C^{11} decay curve in plastic scintillator.

with the energy of the beam and with the goals of different experimenters, the initial activity of C^{11} obtained by extrapolating the decay curve back to the end of the bombardment varied greatly. For the Bevatron experiment at 1610 MeV the initial activity was only 135 counts/min above a background of 135 counts/min, whereas one bombardment with the 304-MeV beam at the cyclotron gave an initial activity of about 47,000 counts/min. However, most of the data were obtained with initial activities of a few thousand counts/min. The counting data were plotted, the activity was extrapolated to end-of-bombardment time, and the initial activity A_0, was read from the graph.

G. Efficiency of C^{11} Detection System

1. Theory of β-γ Coincidence Method

For absolute determination of the cross sections, the efficiency of the C^{11} detection system must be known. A β-γ coincidence method was used to measure the efficiency. This technique requires the simultaneous measurement of the counting rate in the β detector N_β, the counting rate in a γ detector N_γ, and the coincidence counting rate $N_{\beta\gamma}$. Because C^{11} decays 99 + % by positron emission the coincidence is between the positron and the 0.511-MeV γ ray from the annihilation of the positron. The absolute disintegration rate N_0 is given by the product of the singles counting rate divided by the coincidence counting rate. The use of β-γ coincidence technique in determining absolute disintegration rates is discussed by Campion[20] for the general case with high-efficiency β detectors, and by Cumming and Hoffman[17] for the specific case of C^{11}.

With the assumption that the efficiency is independent of the location of the activity in the source, the equations for N_β, N_γ, and $N_{\beta\gamma}$ given by Cumming and Hoffman can be modified so that:

$$N_\beta = [\epsilon_\beta + 2(1 - \epsilon_\beta)f]\, N_0 \quad ,$$

$$N_\gamma = 2\, \epsilon_\gamma\, N_0 \quad ,$$

$$N_{\beta\gamma} = 2\, \epsilon_\gamma\, [\epsilon_\beta + 2(1 - \epsilon_\beta)f]\, N_0 ,$$

where

ϵ_β is the efficiency of the β counter for detecting β,

ϵ_γ is the efficiency of the γ counter for detecting γ,

and f is the probability that an annihilation γ is counted by the β detector.

The quantity

$$\frac{N_\beta N_\gamma}{N_{\beta\gamma}} = \frac{[\epsilon_\beta + 2(1 - \epsilon_\beta)f]N_0 \; 2\epsilon_\gamma N_0}{2\epsilon_\gamma [\epsilon_\beta + 2(1 - \epsilon_\beta)f]N_0} = N_0$$

equals the absolute disintegration rate. The C^{11} counter efficiency was found by dividing the observed counting rate by the disintegration rate.

2. Apparatus

A fast-slow coincidence system set up by Richard Chanda was used for the β-γ coincidence measurements. This equipment was designed as a dual-channel coincidence unit with pulse-height analysis in each channel. The pertinent units of the fast-slow coincidence system are shown in Fig. 14. The fast coincidence unit was designed by Mitch Nakamura of the electronics development group.

Two pulses are taken off each phototube. The fast pulse is amplified by distributed amplifiers and sent to the fast coincidence unit. The slow pulse goes through a cathode follower, which stretches and shapes the pulse to make it suitable for a DD2 linear amplifier. Each DD2 amplifier used in this experiment has a single-channel analyzer built into the same chassis. The output of the single-channel analyzers was sent to the slow coincidence unit (Tranco). Meanwhile the output of the fast coincidence unit was sent through a variable delay and gate unit which delayed the pulse, and generated a pulse to be in triple coincidence with the two pulses from the single-channel analyzers.

The output of the Tranco coincidence unit was sent to a scaler. The output of the single-channel analyzer was also sent directly to a scaler to record the number of single events in each detector. Thus only those pulses that went to the coincidence unit were recorded as singles. This means that the efficiency of the β singles counter was

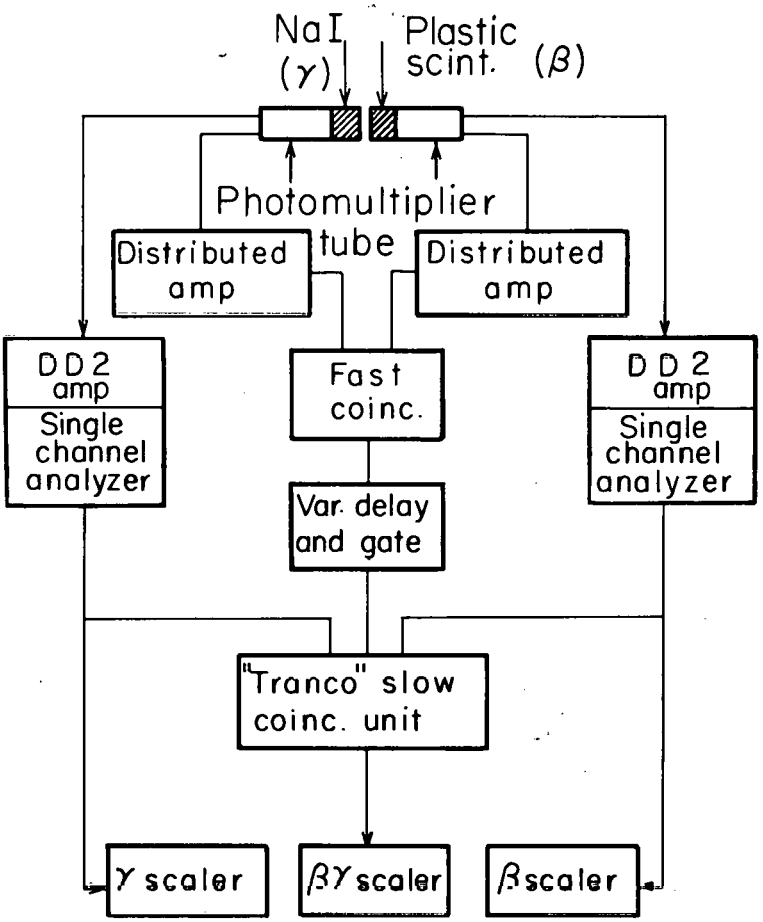

Fig. 14. Electronics for "fast-slow" βγ coincidence system.

equal to the efficiency of the β channel of the coincidence counter, and likewise for the γ pulses.

3. Techniques

The resolving time of the fast-slow coincidence unit is governed by the length of clipping line attached to the fast coincidence unit. The clipping line used was 16.7 ft of RG/63, 125-Ω cable, which has a transit time of 20 nsec. Because the pulse must be reflected back through the cable, the clipped pulses have a 40-nsec length. The width of the delay curve is expected to be about twice this time, as is shown by the experimental delay curve in Fig. 15. The delay curve is obtained by introducing various lengths of cable into one or the other signal lines to the fast coincidence unit, then measuring the coincidence counting rate. In order to test whether one is obtaining 100% coincidence efficiency, clip lines of various lengths are used on the coincidence unit. As long as the counting rate on the plateau does not decrease as the width of the plateau decreases, one still has 100% counting efficiency. The resolving time with the 16.7-ft clip line of the coincidence unit was measured experimentally by counting two separate Na^{22} sources with the detectors placed far enough apart to prevent any true coincidences. The random coincidence rate (chance coincidences) obtained by this method is related to the resolving time by

$$N_{ch} = 2\tau N_{\beta} N_{\gamma} ,$$

where

N_{ch} is the chance coincidence counting rate,
N_{β} is the counting rate in the β detector,
N_{γ} is the counting rate in the γ detector,

and τ is the resolving time.

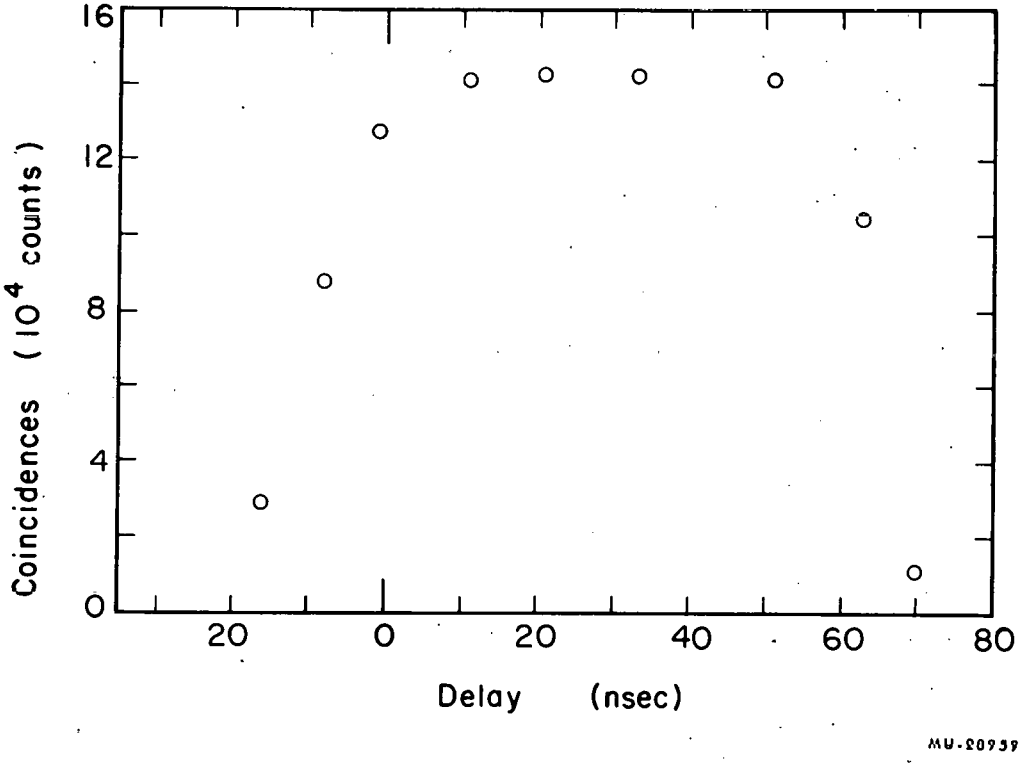

Fig. 15. Delay curve for fast coincidence circuit in $\beta\gamma$ coincidence experiment.

The resolving time obtained was 1$\frac{1}{2}$0 nsec, which is in fair agreement with the width of the delay curve.

The timing for the triple coincidence was not nearly as critical as with the fast coincidence, since the trigger pulses were all 2-μsec long.

The operation of the coincidence system was checked by using a Na^{22} source. This source was previously standardized in a 4π β counter. The disintegration rate measured by 4π counting agreed within the experimental error with the disintegration rate determined by the β-γ coincidence method.

The highly active C^{11} source needed to obtain reasonable counting rates with the coincidence apparatus was prepared by bombarding one of the 2.5-in.-diam by 1-in.-thick plastic-scintillator targets with the 730-MeV external proton beam of the 184-inch cyclotron.[21] Even at one-sixth the full-intensity proton beam, too much C^{11} activity was produced for the β-γ counting equipment to handle immediately. The proton beam was uncollimated and presumably created C^{11} throughout the entire volume of the target in the same fashion as the pion beam.

The singles and coincidence counting rates were measured at several different times. Then the plastic scintillator and phototube were taken to the C^{11} detector cave, mounted in the tube base, and the counting rate measured under the same conditions as with an ordinary pion bombardment. Several points were measured for the C^{11} decay curve in the positron detection system, after which the phototube and scintillator were moved back to the coincidence apparatus for several β-γ coincidence measurements. This cycle was repeated so that points were obtained for the disintegration-rate (N_0) decay curve and for the C^{11}-detector decay curve. From the C^{11}-detector decay curve, the counting rate was interpolated to each of the times at which a disintegration rate data point was taken. The ratio of the

C^{11}- detector counting rate to the disintegration rate at a given time was equal to the efficiency of the β counter. The average of the efficiencies at seven different times was found to be $82.7 \pm 2.8\%$. All these points were taken after the source had decayed to a level the electronics could handle.

The raw data from the β-γ coincidence measurement consisted of the singles counting rate in the β and γ detectors, and the coincidence counting rate. Several corrections had to be made to this data before calculating the source strength. The chance-coincidence counting rate, N_{ch}, was calculated by using the τ determined from the two Na^{22} sources and was subtracted from the observed coincidence counting rate. The natural-background counting rate in each of the singles counters and in the coincidence counter was subtracted from their respective counting rates. (This background was determined 24 hours after the end of bombardment.) Because a γ ray associated with C^{11} decay was produced only as a result of a positron being emitted, events in which an annihilation γ gave a pulse in the plastic scintillator counter and no pulse from a positron was observed, were treated as true β counts.

H. Targets

The plastic-scintillator targets used throughout this experiment were a blend of polystyrene (97%), terphenyl (3%), and tetraphenyl butadiene (0.03%). This plastic is 91.54% C by weight and 8.46% H. The plastic scintillator was machined and polished by the accelerator technicians group to a diameter of 2.5 in. and a thickness of 1 in. The surface density in atoms of C per cm^2 was calculated from the following formula:

$$n = \frac{W}{A} (\%C) \frac{N}{M} ,$$

where

n = atoms of C per cm^2,
W = weight of plastic scintillator in grams,
A = area in cm^2
%C = percentage of C in scintillator,
N = Avogadro's number in atoms per mole,
M = atomic weight of C in g/mole.

C^{13} is 1.11% of naturally occurring C; however, no attempt was made to distinguish between the production of C^{11} from C^{12} or C^{13}. The cross sections presented in this report were calculated for the production of C^{11} from both carbon isotopes.

Four different plastic scintillators were used at various times during this experiment. These scintillators are listed in Table III along with their calculated surface densities.

Table III. Plastic scintillator targets.

Target	Surface density
PL I	1.115×10^{23} (atoms C/ cm^2)
PL II	1.218×10^{23}
PL III	1.12×10^{23}
PL IV	1.146×10^{23}

PL I and PL II were used during the preliminary experiments when an ion chamber was used to monitor the pion beam rather than the counter telescope. These targets were also placed in the external proton beam at the 184-inch cyclotron to provide the high-activity C^{11} source for the β-γ coincidence experiment. After these proton bombardments, PL I and PL II had built up a considerable internal background due to the 53-day Be^7 activity. Be^7 decays mainly by K capture to the ground state, but has a 0.477-MeV γ ray in 12% of the decays.[18] Pulse-height analysis of the background in PL I and PL II gave a spectrum that corresponded to the Compton scattered electrons from the 0.477-MeV γ ray.

PL III and PL IV were used in all the runs with the counter telescope. Since these targets were bombarded only in the relatively low-intensity pion beams, Be^7 was never produced in observable yield. The background in these targets remained at a constant level despite the many pion bombardments involved. Before each bombardment, the plastic scintillator was cleaned with ethyl alcohol to remove the silicone grease used to couple the scintillator to the phototube. At the end of these experiments, the targets PL III and PL IV were reweighed to see if any loss in weight had occurred because of the frequent cleaning. No change in weight was observed.

I. Corrections to C^{11} Initial Activity

1. Neutron Background

The meson cave at the 184-inch cyclotron has a background of fast neutrons and other particles, which might contribute to the production of C^{11}. The effect of this background radiation was measured by placing an identical plastic scintillator at various locations around the target position and exposing it for the same length of time as the target itself. The activity in the dummy scintillator was then counted in the same manner as the target. The dummy activity was fairly independent of location if the dummy had been placed about a foot or more out of the beam. The correction due to stray background was taken as the activity of the dummy target when placed a foot from the beam. This correction varied, depending on the particular experimental setup in use at the time. Even though the internal beam was usually run at its maximum level, the amount of background around the counter telescope varied because different amounts of concrete and wood shielding were used in the various beam setups.

The activity in the dummy target due to stray background in the meson cave was seldom as much as the natural cosmic-ray background of the detection system, so it was extremely difficult to resolve a decay curve due to the dummy activity. A 20.4-min decay curve was arbitrarily drawn through the data and extrapolated to zero time. The extrapolation from the first data point to zero time was about 5 min, which should not have caused a serious error. This initial activity was subtracted from the initial activity of the target to obtain the net activity due to the pion beam. This correction was less than 5% of the initial activity, except for the data at 53, 60 and 1610 MeV. At the three energies mentioned, the absolute magnitude of the correction was even less than in the other cases, but the total initial activity was so low that the correction was as much as 20%.

The use of the dummy target activity also corrected for another slight source of error. As mentioned previously, some authors have noticed that plastic scintillators after being exposed to light will produce an apparent activity due to its own phosphorescence or due to static electrical charges caused by rubbing the scintillator before mounting. The cosmic ray background was too large to see this effect in this apparatus, but if such an effect were present, it would be included in the subtraction for stray background. The activity in the target scintillator never showed any component other than that due to C^{11}.

2. Internal Secondaries

Because the scintillator targets were thick, the possibility existed that secondary particles (neutrons and protons) produced by nuclear interactions of the pions with target nuclei could cause the production of C^{11}. The secondary particles would need at least 18.3-MeV energy to overcome the binding energy of the neutron in C^{12}. Thus evaporation nucleons, normally averaging a few MeV, would probably not have enough kinetic energy to create C^{11}. However, particles ejected during the initial cascade or as a partner in an absorption event could be sufficiently energetic. Because a wide variety of kinetic energies is possible for these particles and because the cross sections are changing rapidly with energy, no attempt was made to calculate a correction due to this effect. The correction was found experimentally by measuring the cross section as a function of lucite thickness placed before counter B and the target. The cross section is expected to increase with increasing lucite thickness, so by extrapolating the observed cross sections back to zero thickness it was hoped to correct for finite target thickness. Lucite was chosen as the absorber because of its similarity to plastic scintillator in physical properties and its convenience.

Because small changes in cross section were measured by this technique, it was necessary to use a very intense pion beam to insure

reproducibility and accuracy. The 310-MeV π^- beam set up by Booth et al. was sufficiently intense.[22] However, their experimental setup required the use of a γ-ray counter consisting of alternate layers of Pb and plastic scintillator. One corner of this counter extended into the pion beam, meaning that the pion energy at the plastic targets was 215 ± 37 MeV. The spread in energy was caused by the fact that some of the pions reaching the target had to pass through more of the γ counter than others. The measured correction represents an average correction for a relatively large energy range. Because this correction was not measured at other energies, it was assumed that the absolute correction was independent of pion energy and dependent only on the total number of pions through the target. The absorption cross section probably determines the production rate of secondaries. At 215 MeV the absorption cross section is about 25mb.[23] It does not vary by more than a factor of two from this value over the energy range from 50 to 300 MeV.

The large beam intensity and relatively large $C^{12}(\pi^-,\pi^-n)C^{11}$ cross section at 215 MeV gave large initial C^{11} activities of the order of 10,000 counts/min. The cross sections as a function of thickness are plotted in Fig. 16. All the points were obtained with a total number of pions of about 3.75×10^7. The correction, related to pion intensity for convenience, amounted to 2 mb for this number of pions, so all the cross sections were corrected by 0.267 mb/10^7 pions through the target. For many bombardments the absolute magnitude of the correction was negligible because of low beam intensities.

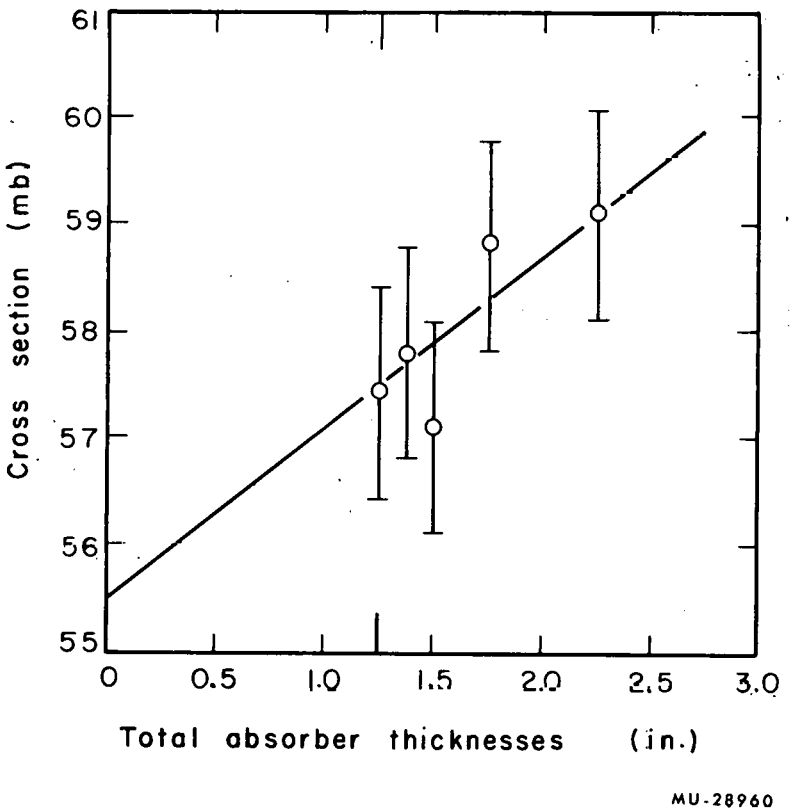

Fig. 15. Correction for finite target thickness. $C^{12}(\pi^-,\pi^-n)C^{11}$ cross section is plotted vs the sum of the scintillator target, counter B, and lucite thicknesses.

J. Results

1. Data

The corrected cross sections are presented in Table IV and the $C^{12}(\pi^-,\pi^-n)C^{11}$ excitation function is shown in Fig. 17. The table gives the incident-pion energy preceded by a number referring to the Physics group listed in Appendix E whose pion beam was used. The final column gives the number of individual bombardments used to determine the cross section. The uncertainty listed with the pion energy is compounded out of the energy spread of the beam in passing through the target. The pion energies of 179 and 212 MeV were obtained by placing 2 in. and 1 in., respectively, of Cu in the 245-MeV beam. The energy of 342-MeV was obtained by placing 1 in. of Cu in the 373-MeV beam. All the energies in the table refer to the energy of the pions at the mid-point of the plastic-scintillator target.

Also included in this table are two high-energy measurements made at Brookhaven by using a similar technique.

At the bottom of the table are listed the two measurements made with π^+ beams at the 184-inch cyclotron. These experiments are discussed in Sec. V.

2. Errors

The error associated with the cross section was calculated from the uncertainties in efficiency of the C^{11} detector, production by secondaries, stray background, muon contamination, and initial activity. The efficiency of the C^{11} detection system (Sec. II-G) was measured to be 83 ± 3% and was the same for all bombardments. The uncertainty in the correction for production of C^{11} by secondaries (Sec. II-I-2) was large but the magnitude of the correction was small and often negligible. This correction was typically about 4 ± 2%. The correction for stray background (Sec. II-I-1) was about 20 ± 5% at 53, 60, and 1610 MeV and less than 5 ± 1% at other energies. The correction for muon contamination (Sec. II-C-2) was large, 35 ± 5%, at the very low energies but decreased to about 8 ± 1% at 373-MeV. The uncertainty in the determination of the initial activity (

(Sec. II-F-3) depended on the intensity of the pion beam. The 53-, 60-, and 1610-MeV beams had low intensities and consequently the C^{11} decay curves could be extrapolated with an accuracy of about 15% for the initial activity. At other energies the initial activity could be determined to less than 5%.

Table IV. Cross sections for the reaction $C^{12}(\pi^-,\pi^-n)C^{11}$.

Physics group (Appendix E)	Incident-pion energy (MeV)	Cross section (mb)	No. of bombardments
1	53 ± 5	3 ± 2	(1)
1	60 ± 6	11 ± 2	(2)
2	80 ± 8	39 ± 3	(2)
3	127 ± 11	56 ± 4[a]	(3)
4	179 ± 10	68 ± 6	(3)
4	212 ± 10	68 ± 6	(3)
4	245 ± 10	61 ± 6	(3)
5	304 ± 9	42 ± 4	(3)
6	342 ± 10	37 ± 4	(2)
6	373 ± 10	30 ± 3	(3)
6	423 ± 10	26 ± 8	(4)
7	1610 ± 20	21 ± 5[b]	(1)
	1000	20 ± 3[c]	
	1900	20 ± 3[d]	
	Cross sections for the reaction $C^{12}(\pi^+,\pi^+n)C^{11}$		
8	73 ± 7	55 ± 20	(1)
2	110 ± 7	40 ± 4	(3)

[a]The pion beam was monitored by means of a calibrated ion chamber.

[b]The counter telescope was not used for this cross section. The pion intensity was calculated from data supplied by Segrè-group experimenters for the pion beam at the Bevatron.

[c]These data are from reference 24.

[d]These data are from reference 25.

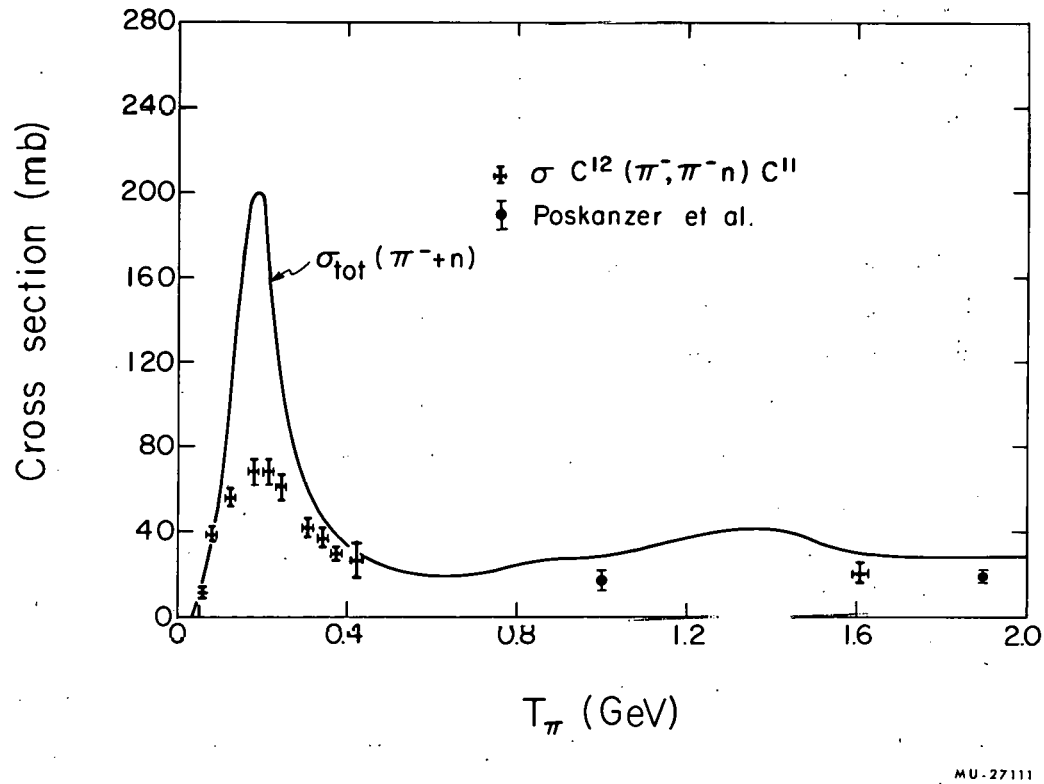

Fig. 17. Cross section for $C^{12}(\pi^-,\pi^-n)C^{11}$ reaction plotted vs incident pion energy. The smooth curve is the total cross section for π^-n free-particle scattering, which is equal to the total cross section for π^+p scattering by charge symmetry.

III. $C^{12}(\pi^-,\pi^-n)C^{11}$ DISCUSSION

A. General Discussion of π + C

Previous experiments of π scattering on C have been concerned mainly with measuring the total cross section, elastic (or diffraction) cross section, and the inelastic (or absorption) cross sections. Much of this work has been summarized by Ignatenko.[26] The Russian work shows that both the total cross section and inelastic cross sections seem to have an energy dependence similar to that of the free -particle πN scattering.

This effect is quite pronounced in the data for the inelastic cross section for π^- on C. Angular distributions for elastic and inelastic scattering of π^- on C^{12} have also been measured along with the energy distribution of the inelastically scattered pions. The elastic scattering can be calculated by using the optical model. The inelastic scattering shows a large backward peaking which corresponds to pion scattering from individual nucleons in C^{12}. The interpretation is that the pion interacts with the nucleus solely by πN collisions rather than with clusters of nucleons or with the nucleus as a whole. Because so many of the nucleons in C^{12} may be considered as surface nucleons, there is a high probability that the pions escape from C^{12} after just one collision. However, for heavier nuclei the data indicate that multiple collisions may occur before the pion escapes.

Relatively few experiments have been performed where specific nuclides have been measured as products of pion-induced reactions. The excitation function for $C^{12}(\pi^-,\pi^-n)C^{11}$ presented here is a partial explanation of why the total cross section and inelastic cross sections for π^- on C^{12} show a maximum at the πN free-particle-scattering resonance. The $(\pi^-;\pi^-n)$ reaction is only one of several

inelastic reactions that may occur following the initial pion-nucleon collison. Examples of other reactions are (π^-,π^-p), (π^-,π^0n), $(\pi^-,\pi^-xn\,yp)$, etc. All these reactions will be initiated by a primary πN collision, the probability of which is governed by the free-particle cross section. The sum of all these processes is then equal to the inelastic cross section.

The situation is slightly different in heavy nuclei where, following the initial πN collision, both the collision partners are likely to undergo further collisions with other nucleons and wash out the free-particle resonance. However, even in heavier nuclei the (π^-,π^-n) reaction is expected to show the resonance behavior, since this reaction probably occurs mainly on the nuclear surface.

B. Discussion of (p, pn) Mechanisms

The theoretical discussion of the $C^{12}(\pi^-,\pi^-n)C^{11}$ reaction will be based entirely on analogy with the C^{12} (p, pn) C^{11} reaction. Therefore, this discussion will begin with a brief review of the present status of the (p, pn) reaction in general, follow with a comparison of the possible mechanisms as applied to both (p, pn) and (π^-,π^-n) reactions, and end with a rough calculation of the $C^{12}(\pi^-,\pi^-n)C^{11}$ cross sections based on the direct-interaction model.

The (p, pn) reaction has been extensively studied in recent years.[27,28,29,30] The experimental results have been compared with the predictions of the Monte Carlo calculations of Metropolis.[31] The calculated cross sections are consistently low by factors of two to nine, depending on the energy region and the target nucleus considered. The approximations in the nuclear model are probably responsible for this discrepancy. The model used a square well instead of a more realistic diffuse nuclear surface.

Three different mechanisms probably contribute to the (p, pn) reaction. These mechanisms have different relative importances in different energy regions. In reasonably heavy nuclei the compound-nucleus mechanism probably dominates the yield for incident proton energies up to about 40 MeV. This mechanism assumes that the bombarding particle is completely absorbed by the target nucleus. The kinetic energy of the projectile is shared among all the nucleons, resulting in a highly excited nucleus. After a relatively long time the nucleus de-excites by emission of the necessary particles and γ rays.

At higher bombarding energies, most spallation reactions are interpreted in terms of the Serber process.[32] This mechanism supposes that the nuclear reactions occur in two stages. The first stage is a "cascade" of fast two-body collisions, with some nucleons being knocked out directly. The end of the cascade stage results in a highly excited nucleus which then de-excites in a manner similar to the compound nucleus —by evaporation of nucleons and γ-ray emission.

The (p,pn) reaction above 40 MeV is thought to proceed through two special applications of the Serber process. If the incident particle strikes a particular nucleon and both collision partners escape from the nucleus directly, the process is called the "pure knock-on" or "one-step" mechanism. This is equivalent to a one-collision cascade without evaporation. The struck nucleon must be a neutron in order to have a (p,pn) reaction. The excitation energy caused by the removal of this neutron must not be greater than the binding energy of the most loosely bound particle in the residual nucleus. It if were, other nucleons would be emitted and the (p,pn) product would not be observed.

The other special application of the Serber process is the "knock-on plus evaporation" or "two-step" mechanism. In this mechanism there is again just one collision between the incident particle and a nucleon of the target nucleus. However, this time only one of the collision partners escapes directly while the second partner shares its recoil energy with the whole nucleus. Eventually the nucleus de-excites by the emission of one nucleon. The struck nucleon in this case may be either a proton or a neutron. If the knocked-out particle is a proton, then the evaporated particle must be a neutron in order to have a (p,pn) event, and vice versa if the knocked out particle is a neutron. To distinguish these last two mechanisms, we will call the first one a (P,Pn) event and the second a (P,Np) event, following the nomemclature of Metropolis et al.[31] The one-step mechanism can be denoted as a (P,PN) event.

Merz and Caretto attempted to distinguish between the (P,PN) and the (P,Pn) mechanisms by studying the recoil behavior of the Cu^{64} nuclide in the reaction $Cu^{65}(p,pn)Cu^{64}$ over the energy region of 100 to 400 MeV.[33] They concluded that both mechanisms were important over this energy region with the (P,Pn) process being more important at the lower energies and the (P,PN) process predominating at the higher energies.

A distinctly different way for a (p, pn) reaction to occur would be by neutron pickup to form a deuteron. This process is expected to decrease very rapidly with energy.[30]

C. $C^{12}(p,pn)C^{11}$ Reaction

This reaction has been studied extensively because of its convenience as a monitor for proton intensities. The presently accepted cross sections in the energy range from threshold to 300 MeV are those given by Crandall.[34] Reference to some of the higher energy cross section measurements are given in the work of Cumming, Friedlander and Swartz.[35] Recently these cross-section measurements have been extended to 28 GeV by Cumming, Friedlander, and Katcoff.[36] There are two distinctive features of the $C^{12}(p,pn)C^{11}$ excitation function. The first is the low-energy peak at about 45 MeV, and the second is the lack of energy dependence above 1 GeV. The energy insensitivity at high energies is a general characteristic of all (p,pn) reactions. As shown in Fig. 18, the shape of the $C^{12}(p,pn)C^{11}$ low-energy peak is rather different from the peaks of (p,pn) excitation functions for other light and medium mass nuclei.[27] The C^{12} peak is not nearly as sharp as the observed peaks in F^{19} and Na^{23}. The C^{12} peak occurs at an energy about 15 MeV higher than these other peaks, which is more than the energy needed to account for the tight binding of the neutron in C^{12} (E_B = 18.3 MeV). The fall off of the C^{12} peak is much more gradual than that of the corresponding peaks for F^{19} and Na^{23}. Since C^{12} is such a small nucleus with most of the nucleons being close to the surface, it seems reasonable to assume that compound-nucleus formation is relatively less important for the C^{12} peak than for the peaks in other (p,pn) reactions. Also the compound-nucleus mechanism seems unlikely for the $C^{12}(p,pn)C^{11}$ reaction on the basis of the excitation energy. Starting with 45-MeV kinetic energy of the incident proton, and subtracting 3.9 MeV for the recoil energy of the compound nucleus, 18.3 MeV for the binding energy of the neutron, and about 0.4 MeV for the Coulomb barrier of the evaporated proton, we are left with 22.4 MeV to be used as kinetic energy of the evaporated proton and neutron or as γ-ray

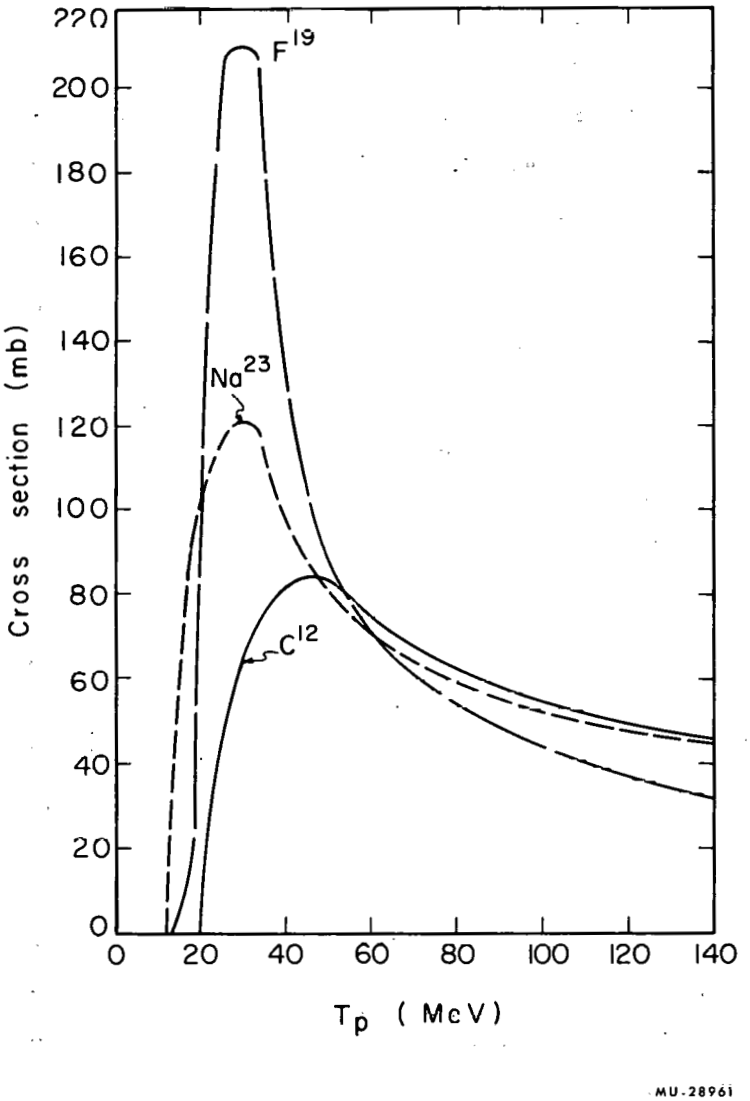

Fig. 18. Excitation functions for (p,pn) reactions in light nuclei;
solid curve is for $C^{12}(p,pn)C^{11}$ reaction (see reference 34);
dashed curve is for $F^{19}(p,pn)F^{18}$ reaction (see reference 27); and
dotted curve is for $Na^{23}(p,pn)Na^{22}$ reaction (see references 27 and 99).

de-excitation. This seems to be an unusually large amount of excess excitation energy for two evaporated particles to carry off.

On the other hand, if we assume the (P,Pn) mechanism at 45 MeV and assume that the average excitation energy for the evaporation step is half the incident energy (to be discussed in Sec. III. D-2), we have 22.5-MeV excitation energy at the peak of the $C^{12}(p,pn)C^{11}$ reaction. Then subtracting the neutron binding energy of 18.3 MeV leaves us with 4.2 MeV if the neutron is evaporated with zero kinetic energy. If the residual excitation is greater than about 8 MeV, the C^{11} nucleus is unstable toward α emission. This argument favors the two-step mechanism over the compound-nucleus mechanism at the peak of the excitation function.

The Monte Carlo calculations show that the (P,Pn) mechanism is increasing in importance as the incident energy decreases, whereas the (P,PN) mechanism decreases in importance at lower energies.[31] The (P,PN) decrease at low energies is due to the shorter mean free paths for low-energy nucleons. However, the recoil experiments of Singh and Alexander show that in the energy region from 0.25 to 6.2 GeV, the (P,PN) mechanism is the major contributor to the $C^{12}(p,pn)C^{11}$ reaction.[37] Thus we conclude that the two-step mechanism (P,Pn) is the major process at the low-energy (peak) region and the one-step mechanism (P,PN) predominates at the high-energy region ($E > 0.25$ GeV). These arguments will be important in our analysis of the mechanism of the (π^-,π^-n) reaction.

Figure 19 shows a plot of the excitation function for the reaction $C^{12}(p,pn)C^{11}$, the total pn cross section, and the pn elastic cross section for comparison. The (p,pn) and total pn excitation functions coincide even without normalization in the region from 100 to 400 MeV. Above 400 MeV the free-particle pn cross section increases slightly and the (p,pn) cross section decreases slightly. This behavior can still be explained in terms of

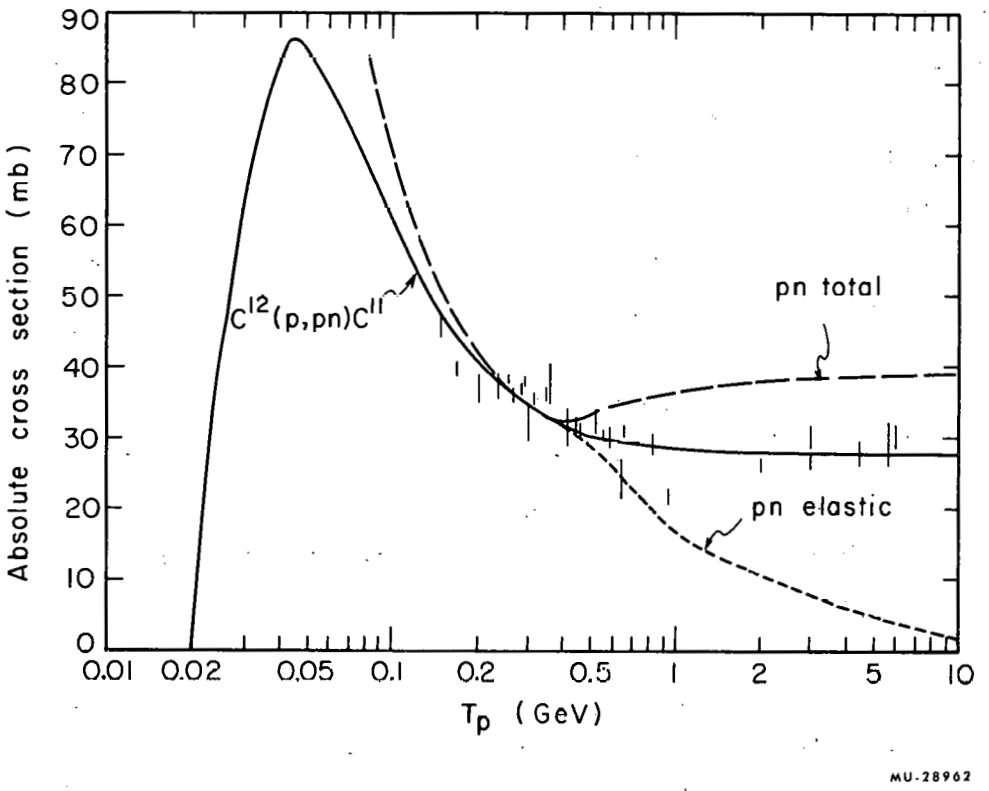

Fig. 19. Solid curve is the $C^{12}(p,pn)C^{11}$ excitation function plotted from data of references 34,35,36,93,94, and 95. The vertical lines represent the experimental cross sections measured in the high-energy region. Dashed curve is the pn total cross section. Dotted curve is the pn elastic cross section.

the single-pn-collision model. At 400 MeV the production of π mesons becomes significant. This means that an additional particle (the pion) must also escape from the nucleus without interacting with other nucleons in order to produce the (p, pn) product. Because the probability that the pion escapes unscathed is less than 1, the yield of C^{11} will be lower than what would be expected on the basis of the total cross section. Since the newly created pion does have a finite chance of escaping, especially from a small nucleus, the yield of C^{11} will be greater than that expected from just the elastic pn scattering cross section alone. This is illustrated in Fig. 19. The fact that the pn and (p, pn) cross sections coincide from 100 to 400 MeV may be coincidental but it makes the comparison easier.

The same statements about the effect of pion production on the yield of C^{11} can be applied to the C^{12} (π^-, π^- n) C^{11} reaction. The data of Fig. 17 show that at 400 MeV the π^-n and (π^-, π^- n) excitation functions are almost identical while the three high-energy points for the (π^-, π^- n) reaction are lower than the π^-n excitation function. Pion production by incident pions would tend to lower the (π^-, π^-n) cross section regardless of whether the one-step or two-step mechanism applies.

D. $C^{12}(\pi^-,\pi^-n)C^{11}$ Mechanism

With this background on the mechanism of the (p,pn) reaction, we now proceed to investigate the mechanism(s) of the $C^{12}(\pi^-,\pi^-n)C^{11}$ reaction. The basic πN interaction is a strong interaction just as is the NN interaction. Thus we expect the (π^-,π^-n) reaction to proceed by one of the mechanisms already discussed.

For incident pions, the process analogous to the compound-nucleus mechanism would be pion absorption. However, absorption of a π^- could not possibly lead to C^{11} since the "compound system" would have a net charge of $Z = 5$.

The two-step mechanism for the pion-induced reaction would consist of a single collision between the incident pion and a nucleon in C^{12}. The pion must then escape the nucleus, and the recoil energy of the struck nucleon must be converted into excitation energy of the nucleus. Eventually the nucleus evaporates just one neutron. For the proton-induced reaction, it was possible for a neutron to be ejected from the initial collision and then be followed by proton evaporation, (Pp,Np). However, the analogous pion-induced process is extremely doubtful—no one has yet shown the existence of meson evaporation.

In the one-step mechanism, only a π^-n collision is allowed and both the pion and the struck neutron emerge from the nucleus immediately. The residual excitation must be less than about 8 MeV to avoid further nucleon evaporation.

For pion-induced reactions, the process analogous to deuteron formation would be the formation of a pion-nucleon isobar. The isobar is a resonant state of a pion plus nucleon and has a lifetime determined from the width of the resonance, Γ, and the uncertainty principle, $\tau = \frac{\hbar}{\Gamma}$. This lifetime is comparable to the time the isobar takes to cross the nucleus, about 10^{-23} sec. Because little is known about isobar cross sections in nuclear matter, we will assume in our later

calculations that the pion and neutron leave the nucleus as separate entities.

Impulse approximation. Before invoking the one-step or two-step mechanisms, we must investigate whether the impulse approximation is still valid for pion-induced reactions. Impulse approximation is the term coined by Chew to describe the assumption that elementary-particle interactions are unchanged within nuclear matter.[38,39,40] The impulse approximation is valid when the mean free path, λ, of the incident particle is much greater than its particle wavelength, $\lambda\!\!\!^{-}$, and when the binding energy of the struck nucleon, V, is negligible compared with the energy of the incident particle, T.

The particle wavelength may be calculated from $\lambda\!\!\!^{-} = \hbar/p$, where p is the momentum. The mean free path for pions in nuclear matter as discussed in Sec. IV.-B is shown later in Fig. 26. For the energy region of interest here, $T_\pi > 50$ MeV, λ is always greater than $\lambda\!\!\!^{-}$. The smallest ratio of $\lambda/\lambda\!\!\!^{-}$ is 1.5, which occurs at the 190-MeV resonance, where λ = 1.0 F and $\lambda\!\!\!^{-}$ = 0.66 F.

Nucleon binding energies are expected to be less than 50 MeV, even for nucleons in tightly bound or "core" shells, so for the bombarding energies of this work, T is always greater than V. Thus we will assume throughout this discussion that the impulse approximation is valid, to the extent that pion-nucleon collisions do occur within the nucleus. However, we will use "effective" cross sections for collisions within nuclear matter, rather than free-particle cross sections.

1. Probability of a (π^-,π^-n) Event

On the basis of the one- and two-step mechanisms, let us set up an expression for the probability of a (π^-,π^-n) reaction occurring at a given location in the nucleus. The general expression is:

$$P = P_i\, P_{coll}\, P_\pi\, P_n\,, \qquad (1)$$

where

P is the probability of a (π^-,π^-n) reaction at a specific point,

P_i is the probability of an incident pion reaching that point,

P_{coll} is the probability of a collision at that point,

P_π is the probability of the recoil pion escaping unscathed,

and P_n is the probability that one and only one neutron is emitted from the nucleus, either by direct knock-on or by evaporation from an excited nucleus.

P_i and P_π are functions only of the pion mean free path and the distance the pion travels in nuclear matter. Thus P_i and P_π are independent of the two reaction mechanisms under consideration. However, P_n and P_{coll} depend on which mechanism one assumes.

For the one-step mechanism, $P_n = \exp(-s_n/\lambda_n)$, where s_n is the distance the recoil neutron has to travel to reach the nuclear surface and λ_n is the mean free path of the neutron. P_{coll} is proportional to the cross section for a π^-n collision because only a π^-n collision is allowed.

For the two-step mechanism, P_n is given by an evaporation formula of the type[41]

$$P_n = \int P_n(\epsilon)d\epsilon = \int K\sigma\epsilon \frac{W(f)}{W(i)} d\epsilon \qquad (2)$$

where $P_n(\epsilon)d\epsilon$ is the probability per unit time of evaporating a neutron with kinetic energy between ϵ and $\epsilon+d\epsilon$, K stands for a group of constants, σ is the cross section for the inverse reaction, and W(f) and W(i) are the density of states for the final and initial nuclei, respectively. For a given excitation energy the integration is performed over only those neutron energies that leave the residual nucleus with less than 8 MeV. P_{coll} is proportional to the sum of the π^-n and π^-p cross sections because both π^-n and π^-p collisions can take place.

2. Determination of mechanism

Our problem now is to determine whether the $C^{12}(\pi^-,\pi^-n)C^{11}$ reaction proceeds by the one-step or two-step mechanism. Because the experimental $C^{12}(\pi^-,\pi^-n)C^{11}$ excitation function peaks at the same

incident pion energy as the free-particle scattering resonance, it seems very likely that a πN collision is taking place inside the nucleus. However, both the one-step and two-step mechanisms contain the term P_{coll}, which is proportional to the effective πN cross section in nuclear matter. Thus both mechanisms could conceivably give rise to a peak provided the other terms in the expression for P do not cancel it out.

If we plot the cross sections for the $C^{12}(\pi^-,\pi^-n)C^{11}$ reaction and the cross sections for the $C^{12}(p,pn)C^{11}$ reaction on the same graph as a function of the momentum of the incident particle, we find that the peaks coincide as shown in Fig. 20. If this plot implies similar mechanisms, we would expect that the momentum transfer and resultant excitation energy of the nucleus are the factors controlling the cross sections in the peak region, because we have indicated that the $C^{12}(p,pn)C^{11}$ reaction proceeds predominantly by the two-step mechanism in the peak region. Yet we claim that the $C^{12}(\pi^-,\pi^-n)C^{11}$ peak is associated with the free-particle π^-n resonance.

This ambiguity can be resolved if we compare the probability for neutron escape, P_n, under the assumption of a two-step mechanism for the case of the (p,pn) and the (π^-,π^-n) reactions. The probability of neutron evaporation and the number of neutrons evaporated is dependent on the value of the excitation energy of the nucleus, and does not depend on how the excitation energy was introduced. Assuming that the product of the three terms, $P_i P_{coll} P_\pi$, is not too different for the proton case and the pion case at the energies of the excitation function peaks, the nuclear excitation energy should be the same if the (π^-,π^-n) and (p,pn) reactions proceed by the same mechanism.

Therefore it is of great interest to plot the average excitation energy under the assumption that a single collision occurs and that the recoil energy of only the struck nucleon is converted into nuclear excitation energy. In order to calculate the average recoil energy $\langle T_R \rangle$, it is necessary to weight the recoil energy for a given scattering angle by the angular distribution:

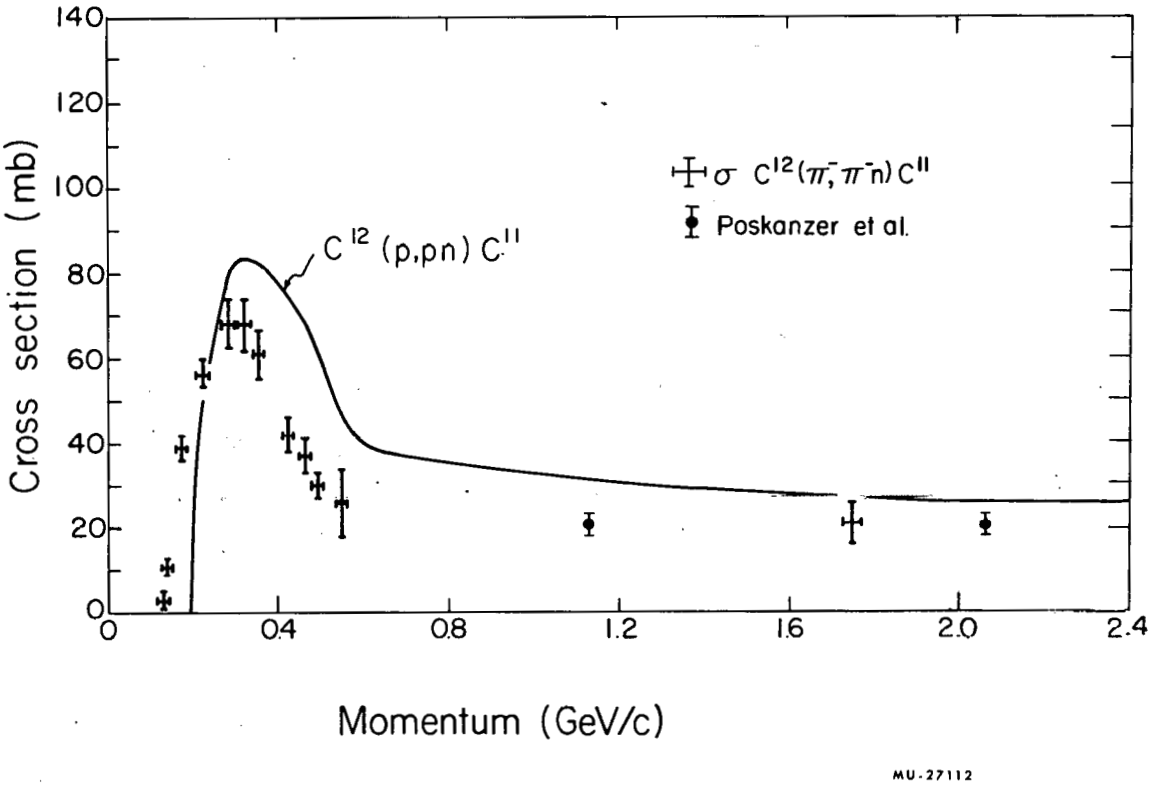

Fig. 20. Cross section for $C^{12}(\pi^-,\pi^-n)C^{11}$ reaction plotted vs the momentum of the incident pion. The smooth curve is the cross section for $C^{12}(p,pn)C^{11}$ reaction plotted vs incident proton momentum. Data are taken from references 34,35,36, 93,94, and 95.

$$\langle T_R \rangle = \frac{\int P(\theta)\, T_R(\theta)\, d\theta}{\int P(\theta)\, d\theta} \quad . \qquad (3)$$

This is quite simple for the nucleon-nucleon case where the angular distribution $P(\theta)$ is either isotropic or symmetric about 90 deg(c.m.) in the incident-proton energy region of interest, 20 to 100 MeV. The recoil energy, T_R, is given by

$$T_R = \frac{2m_1 m_2}{(m_1 + m_2)^2} (1 - \cos \theta') T_1, \qquad (4)$$

where T_1 is the incident energy and θ' is the c.m. angle of the scattered particle. For equal-mass particles this expression is

$$T_R = \frac{1}{2} T_1 (1 - \cos \theta').$$

Integrating T_R over an isotropic or a symmetric angular distribution gives $T_R = \frac{1}{2} T_1$, as shown in Fig. 21.

The average nucleon recoil energy for the πN scattering, however, is considerably more complicated. The angular distributions are quite different above the $J = T = 3/2$ resonance for $\pi^- n$ and $\pi^- p$ scattering. Thus it is necessary to calculate the average recoil energy for a $\pi^- n$ and $\pi^- p$ event separately, weight the average recoil energies by the cross sections for $\pi^- n$ and $\pi^- p$ events, and average again. Thus:

$$\langle T_R \rangle = \frac{\langle T_R^{\pi^- n} \rangle (\sigma_{\pi^- n}) + \langle T_R^{\pi^- p} \rangle (\sigma_{\pi^- p})}{(\sigma_{\pi^- n}) + (\sigma_{\pi^- p})} \qquad (5)$$

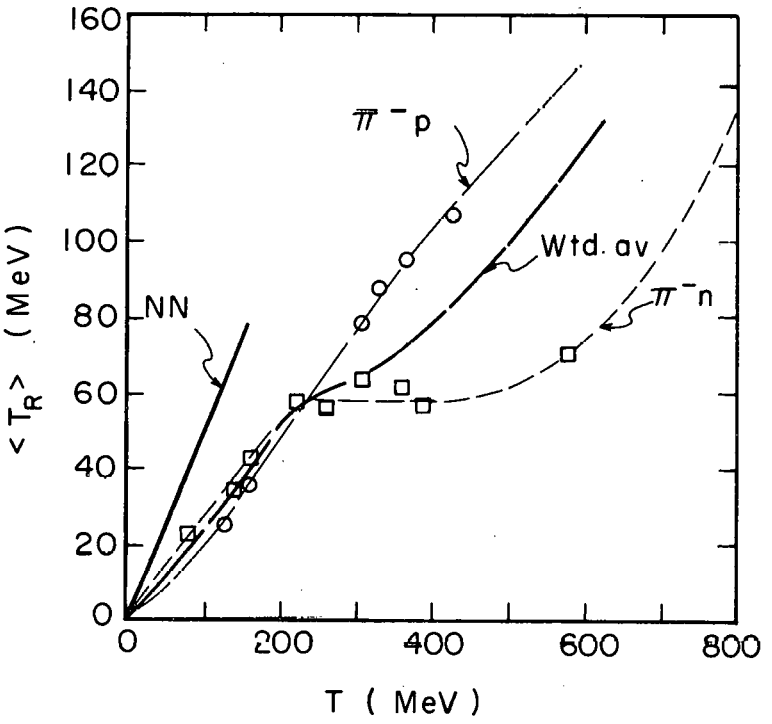

Fig. 21. Average nucleon-recoil energy plotted vs incident particle energy. Heavy solid curve is $\langle T_R \rangle$ for incident protons. Light long-dashed curve is $\langle T_R \rangle$ for π^-p scattering. Light short-dashed curve is $\langle T_R \rangle$ for π^-n scattering. Heavy dashed curve represents weighted average of $\langle T_R \rangle$ for π^-p and π^-n scattering.

$\langle T_R^{\pi^- n} \rangle$ and $\langle T_R^{\pi^- p} \rangle$ were calculated by using the relativistic formula[42]

$$T_R = m_2 c^2 \left[(\gamma_2')^2 - 1 \right] (1 - \cos\theta_1') \qquad (6)$$

where

$$(\gamma_2')^2 = \frac{\left[\gamma + \frac{m_2}{m_1} \right]^2}{1 + 2 \frac{m_2}{m_1} \gamma + \left(\frac{m_2}{m_1} \right)^2} .$$

γ is the ratio of the pion total energy to its rest-mass energy in the laboratory reference frame, m_1 is the rest-mass of the pion, and m_2 is the rest-mass of the nucleon.

The average excitation energies calculated in this manner are shown plotted in Fig. 21 as a function of the incident-particle bombarding energy. Note the considerably different behavior for π^-n and π^-p scattering above 300 MeV.

For our purposes it is more interesting to plot the average excitation energy as a function of incident-particle momentum as shown in Fig. 22. The $C^{12}(p,pn)C^{11}$ and $C^{12}(\pi^-,\pi^- n)C^{11}$ excitation-function peaks coincide when plotted vs incident momentum. However, the average recoil energy of the struck particle, which we are equating to the average excitation energy, is quite different as a function of incident-particle momentum. At the peaks that occur at about 300 MeV/c the average excitation energy of a two-step $(\pi^-,\pi^- n)$ reaction would be more than twice that of a two-step (p,pn) reaction.

Such a high excitation energy for the pion-induced reaction means that more than one nucleon would be evaporated if this process

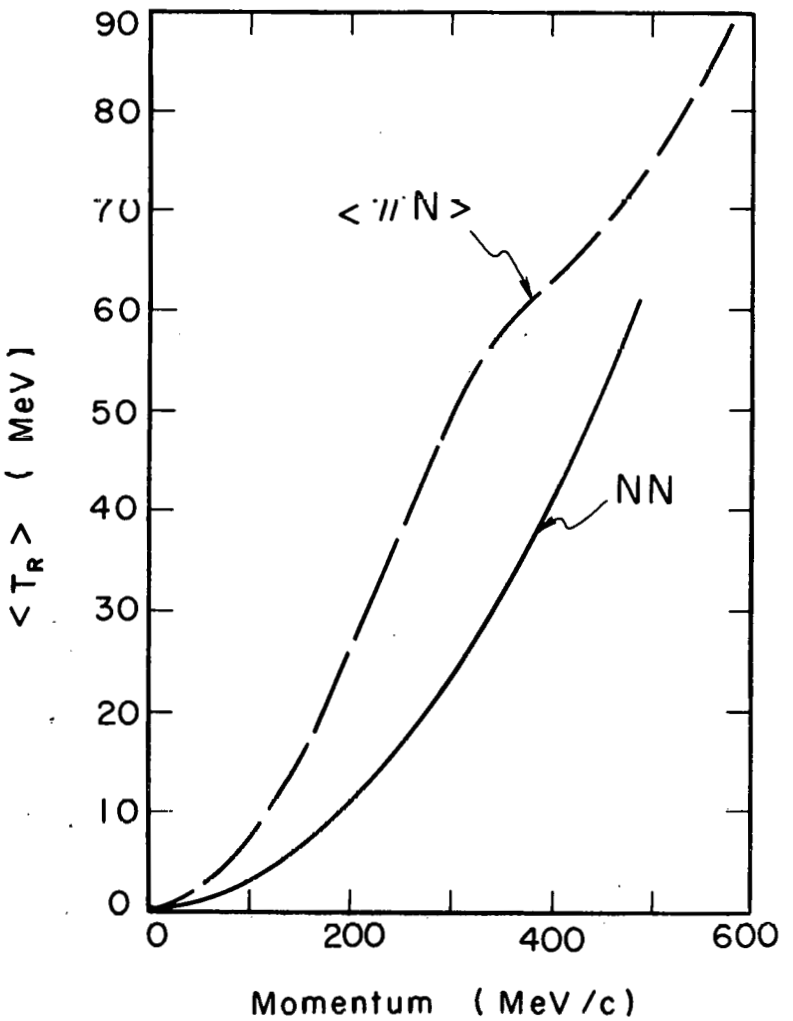

Fig. 22. Average excitation energy from a single collision plotted vs the incident particle momentum. Solid curve is $\langle T_R \rangle$ for a proton-nucleon collision. Dotted curve represents weighted average of $\langle T_R \rangle$ for $\pi^- p$ and $\pi^- n$ scattering.

occurs. In addition, the higher recoil energy of the struck neutron would make it easier for the neutron to escape directly. Thus it seems highly unlikely that the (π^-,π^-n) reaction can occur by the two-step mechanism. The overlap of the (p,pn) and (π^-,π^-n) peaks when plotted as a function of momentum is probably more of a coincidence than of fundamental importance.

A possible method of testing this conclusion would be to measure the excitation function for the reaction $F^{19}(\pi^-,\pi^-n)F^{18}$. The $F^{19}(p,pn)F^{18}$ reaction peak is about 15 MeV lower than the $C^{12}(p,pn)C^{11}$ peak, mainly because of the difference in neutron binding energy.[27] If the $F^{19}(\pi^-,\pi^-n)F^{18}$ peak was measured sufficiently accurately and was found to remain at the πN resonance energy, then we would know that the momentum of the incident particle is not what is responsible for the peak, but rather the peak is caused by the free-particle resonance.

It would also be interesting to measure the $C^{12}(\pi^+,\pi^+n)C^{11}$ reaction in the energy regions of the 600- and 900-MeV, T = 1/2 free-particle resonances. If peaks occurred in the (π^+,π^+n) cross sections at these energies, we would have additional evidence for the elementary-collision mechanism.

E. Resonance-Broadening Due to Neutron Momentum

The simplest explanation of the peak in the $C^{12}(\pi^-,\pi^-n)C^{11}$ excitation function is the one-step or pure knock-on mechanism. The prominent peak in the free-particle πN scattering is a useful tool for showing that elementary particle collisions occur in nuclear matter.

The resonance peak in free-particle π^-n scattering has a full width at half maximum of about 145 MeV, whereas the corresponding width of the (π^-,π^-n) excitation function is roughly 300 MeV. The greater width in the (π^-,π^-n) peak is probably due to the fact that the struck neutron in the (π^-,π^-n) case is moving at a relatively high velocity, whereas the neutron may be considered to be at rest in the free-particle scattering. The broadening of the resonance peak due to the motion of the struck neutron can be estimated as follows.[43]

Consider the following pion-neutron scattering diagram for the laboratory system, where:

E' = total energy of neutron,
p' = momentum of neutron,
E = total energy of pion,
p = momentum of pion,
M = rest mass of neutron,
μ = rest mass of pion.

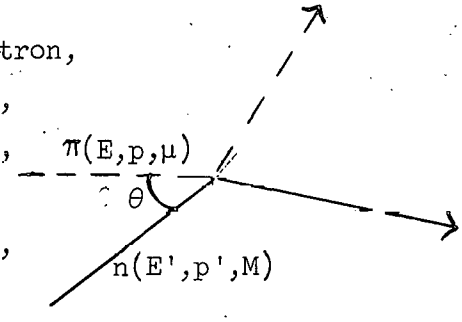

The solid line represents the neutron and the dashed line the pion. The square of the invariant mass of this system is given by S, where:

$$S = (E + E')^2 - (p + p')^2 = M^2 + \mu^2 + 2\,(EE' - \vec{p}\cdot\vec{p}'). \tag{7}$$

The invariant mass is the total energy of the system in the c.m. frame of reference. We then consider the two reference frames:

1. The target neutron is at rest.
2. The target neutron is moving with a momentum p'.

Letting the subscripts 1 and 2 denote the two reference frames, we have:

$$S_1 = M^2 + \mu^2 + 2(M E_1), \quad \text{since} \quad p_1' = 0 \text{ and } E_1' = M,$$

$$S_2 = M^2 + \mu^2 + 2(E_2 E_2' - p_2 p_2' \cos\theta),$$

where θ is the lab angle between the two momentum vectors. Because the interaction cross sections are equal when the c.m. total energy is equal, we will equate S_1 and S_2 and find the difference in pion energies in the two frames:

$$S_1 = S_2 = M^2 + \mu^2 + 2ME_1 = M^2 + \mu^2 + 2(E_2 E_2' - p_2 p_2' \cos\theta). \tag{8}$$

We then approximate E_2' by M since the total energy of a neutron in a nucleus is only slightly changed from the total energy of a free neutron:

$$2ME_1 = 2(E_2 M - p_2 p_2' \cos\theta)$$

$$ME_1 - ME_2 = - p_2 p_2' \cos\theta = M\Delta E,$$

where ΔE is the desired shift in pion energy due to the neutron momentum. With the assumption that the struck neutrons have an isotropic momentum distribution, the average angle will be 0 or 180 deg, so:

$$\Delta E = \frac{\pm p_2 p_2'}{M} . \tag{9}$$

The pion momentum, p_2, at the $\pi^- n$ resonance is 300 MeV/c and the neutron mass, M, is 939 MeV. However the average neutron momentum must be estimated from the available information on proton-momentum distributions. Garron et al. have measured the proton-momentum distribution in C^{12} and have found the data fit separate functions for the s- and p-shell protons.[44] In the next section we will discuss the

reasons why the π^-n collision can only be with p-state neutrons. Anticipating that discussion, we will assume that only the average momentum of the p state is significant. From the data of Garron et al. the average momentum of the p-state protons is 150 MeV/c and we assume that this is valid for the p-state neutrons also. The resultant energy shift, ΔE, is 48 ± 5 MeV. For a head-on collision this would require a decrease of 48 MeV, and for an overtaking collision this would require an increase of 48 MeV in the pion energy in order to keep the c.m. total energy constant. Therefore the total width of the πN resonance for neutrons moving in C^{12} would be approximately:

$$\text{FWHM} = (145 \pm 10) + (48 \pm 5) + (48 \pm 5) = 241 \pm 12 \text{ MeV} \qquad (10)$$

This is slightly less than the experimental width of 300 ± 30 MeV, even after considering the errors on these estimations.

The discrepancy could conceivably be accounted for by a potential for the pion nucleus system. Several authors have required an attractive potential of about 24 MeV to explain pion scattering from complex nuclei.[45,46,23] Using Eq. (9), we estimate an increased width of about 7 MeV due to an attractive potential of 24 MeV. The experimental data presented here are not accurate enough to distinguish effects of this magnitude.

In addition to broadening the resonance peak, an attractive potential ought to shift the peak of the C^{12} $(\pi^-,\pi^-n)C^{11}$ excitation function to lower energy, but more accurate experimental data would be needed to check this prediction also. It is possible that the pion- nucleus potential is weak in the surface regions where the greatest contributions to the (π^-,π^-n) reaction are expected. Thus the potential might have little effect on the (π^-,π^-n) reaction.

F. Benioff Model

Using the impulse approximation, Benioff has given a simplified relationship for calculating (p,pn) cross sections at GeV energies on the basis of a shell-model nucleus with a diffuse surface.[41] This formula is:

$$\sigma_{(p,pn)} = 36 \text{ mb} \sum_{\substack{\text{allowed} \\ \text{shells}}} n_{n\ell j} M_{n\ell} , \qquad (11)$$

where $M_{n\ell}$ is the fractional availability of a particular shell-model state to contribute to the (p,pn) reaction, $n_{n\ell j}$ is the number of neutrons in that particular state and 36 mb is a constant derived from the free-particle cross section. The allowed states are only those states from which a neutron can be removed without exciting the nucleus to cause it to evaporate additional particles. For example, the $s_{1/2}$ protons of C^{12} have a binding energy of about 35 MeV, whereas the binding energy of the $p_{3/2}$ protons is about 16 MeV as determined by (p,2p) coincidence measurements.[44] If a proton were snatched from the $s_{1/2}$ shell, the nuclear excitation due to the $s_{1/2}$ hole would be the difference in the $s_{1/2}$ and $p_{3/2}$ binding energies, or approximately 19 MeV, which is more than enough energy for further particle emission. The neutron binding energies are not expected to differ very much from the proton binding energies for light nuclei so the same reasoning applies to the neutron shells. Thus we say that the two $s_{1/2}$ neutrons are not available for the (p,pn) or (π^-,π^-n) reactions. The sum in Eq. (11) is only over the $p_{3/2}$ neutron shell, which for C^{12} contains four neutrons.

Benioff presents a series of graphs allowing $M_{n\ell}$ to be calculated for various shell states in various nuclei. The constant in front of the summation signs is proportional to the free-particle cross section. Thus it was possible to use Benioff's graphs and appropriate

cross sections for pion scattering in order to calculate the (π^-,π^-n) cross section as a function of energy. The results of this calculation are presented in Table V.

Table V. Comparison of experimental and calculated $C^{12}(\pi^-,\pi^-n)C^{11}$ cross sections following method of Benioff.

Pion energy (MeV)	$\sigma(\pi^-,\pi^-n)$ calc. (mb)	$\sigma(\pi^-,\pi^-n)$ exp. (mb)
190	58	68
370	25	30
1000	21	20
1610	22	21

The agreement is very good regardless of the approximations in the calculation.

However some of Benioff's assumptions in deriving his formula do not apply to the pion-nucleon scattering problem presented here. Benioff's assumptions were expected to be valid only for inelastic scattering of GeV protons and it may be somewhat presumptuous to apply his equation to lower-energy pion scattering. The particular assumptions that are not valid for the pion case are:

1. The assumption that all the outgoing particles travel at 0 deg to the incident beam
2. The assumption that the struck neutron was at rest
3. The assumption that the Pauli exclusion principle does not restrict the number of allowed collisions
4. The assumption that free-particle cross sections can be used without modification in nuclear matter.

Since none of these assumptions are valid for the (π^-,π^-n) reaction, it was desirable to do a calculation to show where in the

nucleus the (π^-,π^-n) reaction is likely to take place. Ideally, one should take account of the angular distribution of πN scattering and also use "effective" cross sections rather than the free-particle cross sections. The calculation outlined in the following section uses a very simple nuclear model and effective cross sections, but performs only a rough integration over the angular distributions, for convenience. However the test of the calculation is in how well it predicts the shape and magnitude of the experimental excitation function. In addition the calculation does provide information on where in the nucleus the (π^-,π^-n) reaction is most likely to take place.

IV. $C^{12}(\pi^-,\pi^-n)C^{11}$ THEORETICAL CALCULATION

A calculation based on the one-step mechanism was performed to show how the concept of a simple two-body collision leads to a peak in the (π^-,π^-n) cross section at the same energy as the $J = T = 3/2$ πN resonance. The mechanism was assumed to involve just one collision between the incident pion and a neutron in the C^{12} nucleus. Both collision partners escaped immediately without interacting with any other nucleons.

An alternative calculation based on the two-step mechanism did not give a peak at the resonance energy. We will first discuss the one-step calculation and present the results. Following this, we will present the two-step calculation and compare its results with the one-step calculation and with the experimental excitation function.

A. One-Step Calculation

The probability that a π^-n collision at a given location in the nucleus contributes to the $C^{12}(\pi^-,\pi^-n)C^{11}$ reaction was calculated for all locations, and these probabilities were integrated over the entire nuclear volume. The location of a collision was determined by specifying the values of two parameters, a and x, where a represents the impact parameter and x represents the distance of travel in the nucleus along the direction parallel to the incident-beam direction. See Fig. 23(a) for a schematic representation of a typical collision event and for a description of the notation employed. Cylindrical symmetry was assumed for all locations with a given value of a and x.

The probability of a (π^-,π^-n) event occurring at a given location was calculated from Eq. (1):

$$P(a,x) = P_i P_{coll} P_\pi P_n \ , \qquad (1)$$

where $P(a,x)$ is the probability of a (π^-,π^-n) event at a location (a,x).

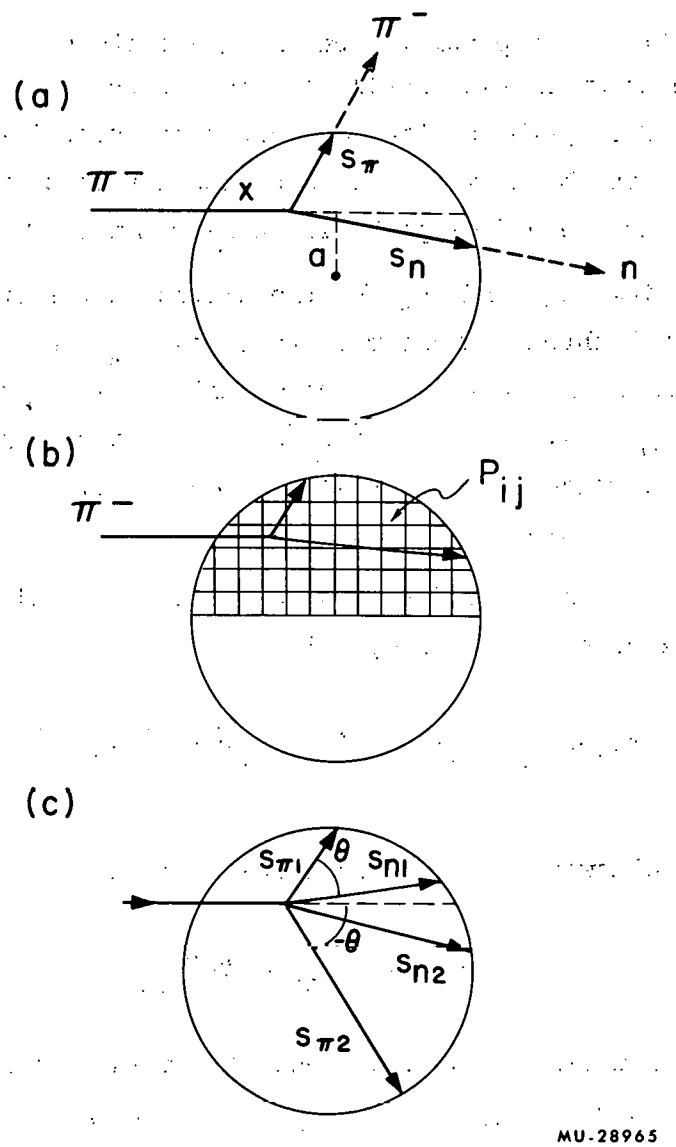

Fig. 23. (a) Representation of a typical π^-n collision.
a is the impact parameter of the incident pion.
x is the distance the pion travels in nuclear matter before reaching the point of collision.
s_n is the distance the neutron travels after the collision to reach the nuclear surface.
s_π is the distance the pion travels after the collision.

(b) Semicircular matrix P_{ij}

(c) Determination of average exit distances
$\langle s_n \rangle = \frac{\langle s_{n1} \rangle + \langle s_{n2} \rangle}{2}$ $\langle s_\pi \rangle = \frac{\langle s_{\pi 1} \rangle + \langle s_{\pi 2} \rangle}{2}$

The probability of a particle traveling a distance x without having a collision is given classically by the expression $e^{-x/\lambda}$, where λ is the mean free path for the particle under consideration. By using the notation in which x is the distance the incoming pion travels and λ_i is its mean free path in nuclear matter, $P_i = \exp(-x/\lambda_i)$.

Letting s_π and s_n be the distances the outgoing pion and neutron travel through nuclear matter, and λ_π and λ_n be the respective mean free paths in nuclear matter, we have $P_\pi = \exp(-s_\pi/\lambda_\pi)$, $P_n = \exp(-s_n/\lambda_n)$. If we set Δx equal to the distance over which a π^-n interaction can occur, then the probability of having a collision within Δx is given by $P_{coll} = 1 - \exp(-\Delta x/\lambda_{\pi^-n})$, where λ_{π^-n} is the mean free path between π^-n collisions. The resulting expression for $P(a,x)$ is:

$$P(a,x) = \exp(-x/\lambda_i)\left[1-\exp(-\Delta x/\lambda_{\pi^-n})\right]\exp(-s_\pi/\lambda_\pi)\exp(-s_n/\lambda_n). \tag{12}$$

If Δx is allowed to become infinitely small then

$$1-\exp(-\Delta x/\lambda_{\pi^-n}) = dx/\lambda_{\pi^-n},$$

where dx is a differential element of distance along the incident-beam path. Since $1/\lambda_{\pi^-n} = \rho_n\sigma_{\pi^-n}$, where ρ_n is the neutron density and σ_{π^-n} is the π^-n cross section, we could write

$$P(a,x) = \exp(-x/\lambda_i)\,(\rho_n\sigma_{\pi^-n}\,dx)\exp(-s_\pi/\lambda_\pi)\exp(-s_n/\lambda_n). \tag{13}$$

Expression (13) is equivalent to Eq. (1) as given by Benioff.[47] The cross section for the (π^-,π^-n) reaction is then found by integrating along the path length dx, weighting the result by $2\pi a\,da$ to account for the cylindrical symmetry, and integrating over da.

$$\sigma_{\pi,\pi m} = \int da\ 2\pi a \int dx\ \rho_n \sigma_{\pi^- n}\ \exp(-x/\lambda_i)\ \exp(-s_\pi/\lambda_\pi)\ \exp(-s_n/\lambda_n). \tag{14}$$

To avoid the use of a machine computation, many simplifying approximations had to be made. Let us consider a plane through the nucleus—including the beam path and the center of the nucleus. This plane was divided into squares with sides equal to one-tenth the nuclear radius. The probability of a $(\pi^-,\pi^- n)$ event was calculated for each square. Rather than doing the integrations, the probability of a $(\pi^-,\pi^- n)$ event was summed over all the squares parallel to the beam path and having the same impact parameter, weighted by the area perpendicular to the beam direction corresponding to the impact parameter, and summed over the impact parameters. It was useful to employ the concept of a semicircular matrix whose elements were the squares corresponding to the locations of a $\pi^- n$ collision, as indicated in Fig. 23(b). The matrix elements were labeled as P_{ij}, where i and j were integers—i corresponding to units along the impact parameter a, and j corresponding to units along the path length x. Each unit represents one-tenth the nuclear radius. With this change in notation, and setting

$$\int_0^r 2\pi\ a\ da = \sum_{i=1}^{10} \pi\ (a_i^2 - a_{i-1}^2)\ , \tag{15}$$

the cross section was found from the expression

$$\sigma_{\pi,\pi m} = \sum_{i=1}^{10} \left[\pi\ (a_i^2 - a_{i-1}^2) \sum_j P_{ij}\right]\ , \tag{16}$$

where P_{ij} is identical with P(a,x) of Eq. (12), with Δx equal to one-tenth the nuclear radius.

1. Nuclear Model

The C^{12} nucleus was assumed to consist of a degenerate Fermi gas of nucleons contained in a spherical box of radius 3.04 F. The nucleon density was assumed to be constant at 1.02×10^{38} nucleons/cm^3 out to the nuclear radius and then was assumed to fall sharply to zero. The Stanford electron-scattering data of Hofstadter show that this assumption is incorrect for the proton-density distribution.[48] For C^{12} he gives a distribution of the form

$$\rho(r) = \rho_0 \left(1 + \frac{\alpha r^2}{a_0^2}\right) \exp(-r^2/a_0^2), \qquad \alpha = 4/3, \quad a_0 = 1.635 \text{ F.} \tag{17}$$

The distance to the point where the density has fallen to half its value at the center of the nucleus is 2.30 F and the skin thickness parameter (the 90% to 10% ρ_0 distance) is equal to 1.90 F.

Thus almost all the C^{12} nucleons can be considered to be in the surface region, which is extremely sensitive to "simple" reactions. However the use of the accurate density distribution greatly complicates the calculation so the simpler square-well model was chosen. The radius of 3.04 F gives the equivalent square-well density corresponding to the diffuse density. (If for the square well, $r = r_0 A^{1/3}$ then $r_0 = 1.33$ F.) The nuclear volume is equal to $(4/3)\pi r^3$ and thus the density of nucleons is $\rho = 3A/4\pi r^3$, where A is the mass number.

The outgoing distances s_π and s_n are strongly dependent on the location of the collision and on the scattering angle. For a fixed scattering angle θ, the scattering distribution is independent of the angle ϕ (the scattering angle in the plane perpendicular to the beam direction.) However, the distance to the nuclear surface is a function of ϕ for collisions not occurring on the central axis. The average distance traveled by the outgoing pion $\langle s_\pi \rangle$ to reach the nuclear surface was approximated by averaging the two distances corresponding to the given scattering angle θ and to $-\theta$ in the two-dimensional plane

defined by the beam path and the center of the nucleus. [See Fig. 23(c).] The same procedure was used to find $\langle s_n \rangle$, the average distance the n travels through nuclear matter for a given scattering angle θ.

2. Angular Integration

The angular distributions for πN scattering have been measured at many energies.[49,50,51,52] These angular distributions vary considerably with energy. In the region of the $J = T = 3/2$ resonance, the π^+p and the π^-p angular distributions have the same shape. This is true up to at least 270 MeV. In the region of the higher πN resonances noticeable differences appear in the π^+p and π^-p angular distributions. In order to calculate the (π^-,π^-n) cross section at a given energy, it is necessary to calculate the cross section at each scattering angle θ, weight each cross section by the relative probability of having a scattering event at that angle, and then integrate the cross section over all the scattering angles. To do this in detail would have required an extremely large amount of time, which was not warranted because of the simplicity of the model chosen for this reaction. Therefore at a given incident-pion energy the (π^-,π^-n) cross section was calculated for only three scattering angles, $\theta_{c.m.} = 0, 90$, and 180 deg. Furthermore, the contribution by the single-collision mechanism to (π^-,π^-n) reactions for pions scattered at 0 deg was assumed to be zero since the struck neutron receives so little recoil energy. Hence the dependence on the scattering angle was taken into account by calculating the (π^-,π^-n) cross section from the following formula:

$$\sigma_{\pi,\pi n} = \frac{\Sigma P(\theta)\sigma_{\pi,\pi n}(\theta)}{\Sigma P(\theta)} = \frac{P(0)\sigma(0) + P(90)\sigma(90) + P(180)\sigma(180)}{P(0) + P(90) + P(180)} . \qquad (18)$$

After the scattering angle was chosen, the recoil energies were calculated from the nonrelativistic expression for elastic scattering, Eq. (21).

B. Mean Free Path of Pions and Protons

The mean free paths in nuclear matter have a great influence on the magnitude of the (π^-,π^-n) cross sections. From classical physics the mean free path of a particle moving in a gas of density ρ particles/cm^3 and having a collision probability of σ cm^2/particle is given by the expression $\lambda = 1/\rho\sigma$.

The nucleon density was taken to be 1.02×10^{38} N/cm^3, as determined above. However, the determination of σ for pions and neutrons moving in nuclear matter is a rather complicated affair. To a first approximation, a weighted average of the free-particle cross sections may be used. However, in nuclear matter the nucleons are not at rest. The nucleon-momentum distribution means that the struck particle is moving with an energy that is not negligible when compared to the incident particle. The projection of the struck nucleon's momentum along the beam axis determines whether the collision occurs at a greater or lower c.m. energy than the c.m. energy expected if the nucleon were at rest. Thus the effective cross section for a collision in nuclear matter represents an average over the nucleon-momentum distribution. Mathematically the effective cross section is given by:

$$\langle\sigma\rangle = \int dE'd\psi \; P\,(E';\psi)\sigma\,[E(E',\psi)] \;, \qquad (19)$$

where

E is the c.m. energy,

E' is the nucleon energy,

and

ψ is the angle of the nucleon momentum with respect to the direction of the incident particle.

$P(E', \psi)$ is the probability of having a nucleon with energy E' and moving at an angle ψ . This quantity is directly related to the nucleon-momentum distribution.[44,53-58] Most of the papers written on this subject discuss only the proton-momentum distribution. If the

present experimental data were sufficiently accurate and the calculations more refined, analysis of the (π^-,π^-n) reaction in the resonance region might be a way of determining neutron-momentum distributions. The factor $\sigma[E(E', \psi)]$ represents the cross section as a function of the c.m. energy. This function is known from the free-particle scattering data. However in nuclear matter, E becomes a function of the neutron energy E' and the angle ψ .

1. Nucleon Mean Free Path

Because the C^{12} nucleus was assumed to be a completely degenerate Fermi gas, the Pauli exclusion principle prohibits those collisions in which the nucleon recoil energy is not greater than the maximum Fermi energy. The fraction of collision events satisfying this criterion is dependent on the angular distribution. Clements and Winsberg have made an extensive computation of nucleon-nucleon cross sections within nuclear matter.[59] The ratio of the effective cross section to the free-particle cross section, α , was expressed as

$$\alpha = \frac{\langle\sigma\rangle}{\sigma_0} = 1 - K\frac{T_F}{T_0} , \qquad (20)$$

where T_F = Fermi energy, and T_0 = incident energy.

For nonrelativistic nucleon-nucleon collisions and for an isotropic angular distribution, K is equal to 7/5 for $T_0 > 2T_F$ as originally derived by Goldberger.[60] Since nucleon-nucleon scattering is not isotropic at higher energies, Clements and Winsberg present K as a function of energy. With Clements and Winsberg's values for K and with the Fermi energy of C^{12} equal to 28.5 MeV (found by extrapolating the Fermi energies tabulated by Metropolis et al.[31]), the effective cross sections for pn and pp scattering in the C^{12} nucleus, $\langle\sigma_{pn}\rangle$ and $\langle\sigma_{pp}\rangle$, were calculated. Because C^{12} has equal numbers of protons and neutrons, the effective cross section for a neutron moving in nuclear matter was taken as the average of $\langle\sigma_{pn}\rangle$ and $\langle\sigma_{pp}\rangle$:

$$\langle\sigma_n\rangle = \frac{1}{2} \left(\langle\sigma_{pn}\rangle + \langle\sigma_{pp}\rangle\right) . \qquad (21)$$

The mean free paths calculated from $1/\lambda = \rho\langle\sigma\rangle$, where ρ is the nucleon density, are shown plotted in Fig. 24.

2. Pion Mean Free Path

The problem of pions moving in nuclear matter has not been analyzed in such great detail as Clements and Winsberg did for the nucleon-nucleon case. In addition to finding the effective π^-n and π^-p scattering cross sections, one must include the effects of pion absorption. In 1956 Frank, Gammel, and Watson discussed this problem in connection with their derivation of an optical-model potential for pion-nucleus scattering.[61]

For pions the mean free path is given by $1/\lambda = 1/\lambda_s + 1/\lambda_a$, where λ_s is the mean free path for scattering, and λ_a is the mean free path for absorption. $1/\lambda_s$ is calculated from $1/\lambda_s = \rho\langle\sigma_\pi\rangle$, where ρ is the nucleon density, and $\langle\sigma_\pi\rangle$ is the effective scattering cross section for a pion moving in nuclear matter. $\langle\sigma_\pi\rangle$ can be approximated by the expression

$$\langle\sigma_\pi\rangle = \frac{1}{2} \alpha \left(\sigma_{\pi^-n} + \sigma_{\pi^-p}\right) , \qquad (22)$$

where σ_{π^-n} and σ_{π^-p} are the free-particle cross sections and α is the "fudge factor" that reduces the effective cross section because of the Pauli exclusion principle and the motion of nucleons in nuclear matter. Sternheimer[62] and Okun[63] have both discussed the problem of meson scattering in nuclear matter and derived similar expressions for the case of isotropic scattering. For πN scattering, they found that $K = 1.747$ in Eq. (20). The values of α calculated for a Fermi energy of 28.5 MeV are plotted in Fig. 25.

However, throughout most of the energy regions of interest here, the πN scattering is not isotropic, so that Eq. (20) is not valid. From the equations and data given by Frank, Gammel, and Watson, the α's

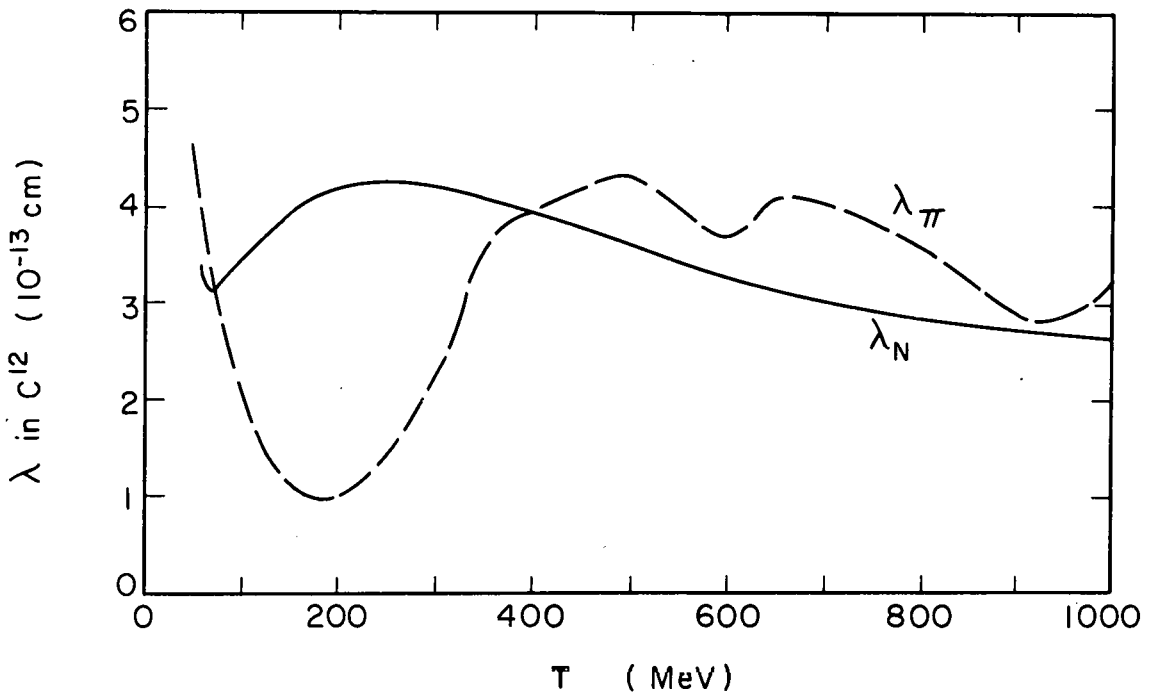

Fig. 24. Mean free path for pions and protons moving inside the C^{12} nucleus plotted vs incident particle energy. Solid curve is λ for protons. Dashed curve is λ for pions.

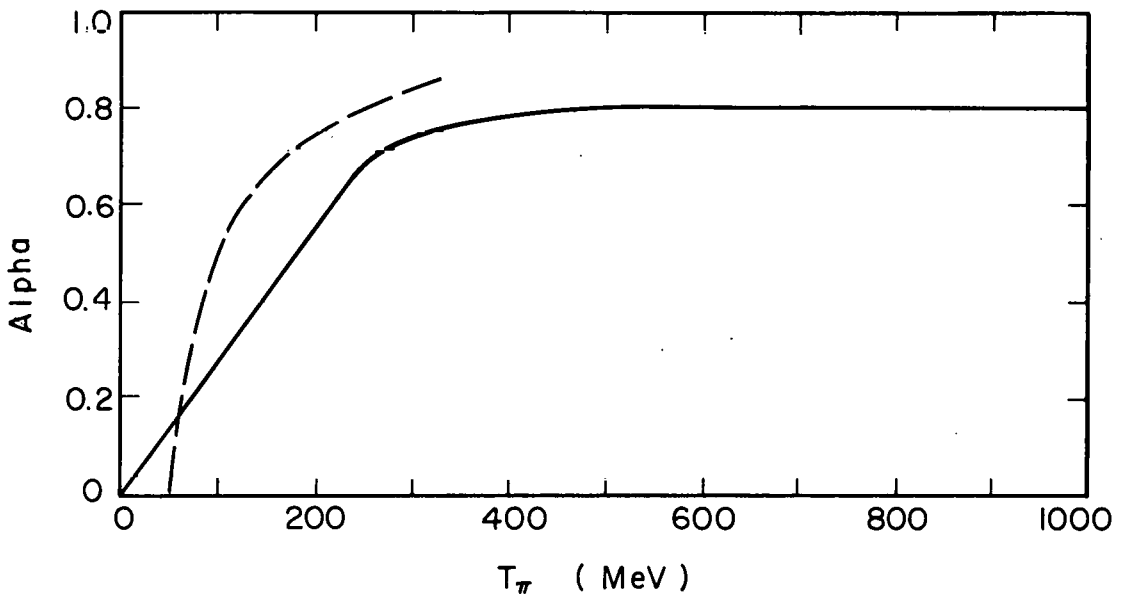

Fig. 25. α (defined in text) plotted vs incident pion energy. Solid curve is used to calculate pion mean free path. Dashed curve is hypothetical α if pion-nucleon scattering were isotropic and nonrelativistic.

that they had used were calculated for energies up to 400 MeV.[61] These α's are also plotted in Fig. 25. Above 400 MeV α was assumed to be constant at about 0.8.[64] This assumption is supported by the Monte Carlo calculations of Grea who found that $\alpha = 0.788$ for 4.5 GeV π^-.[65]

The absorption cross section used by Frank et al., was based on the capture cross section of deuterons for π^+ mesons. The analytical expression they used for this cross section disagrees with the experimental absorption cross sections quoted by Metropolis et al.[23] Therefore the mean free paths for pions were recalculated from the Metropolis values for the absorption cross sections and from the α values of Frank, et al. The calculation was extended to higher incident-pion energies, using a constant value of $\alpha = 0.8$. These mean free paths are plotted in Fig. 24 together with the neutron mean free path. Note that the meson mean free path is considerably smaller than the neutron mean free path over the energy region of the $J = T = 3/2$ resonance. However at higher energies, the meson mean free path is actually slightly longer than the neutron mean free path. Note also that the 600- and 890-MeV resonances in the $T = 1/2$ system appear as minima in the mean free path at the corresponding energies. The gradual decrease in mean free path for neutrons from 400 to 1000 MeV is caused by the increasing pp (or nn) cross section due to inelastic scattering (pion creation).

The pion mean free path from 0 to 350 MeV can be compared with the mean free path calculated by Ignatenko on the basis of the optical model from the total inelastic cross sections of pions on various nuclei.[26] The λ calculated here and the λ calculated by Ignatenko generally agree quite well.

C. Results of One-Step Calculation

The (π^-,π^-n) calculation was performed at three energies: 190, 370 and 1600 MeV, chosen to illustrate the main features of the experimental excitation function. The calculated cross sections must show a large rise at 190 MeV if the model and single-collision mechanism have any validity. The point at 370 MeV is where the experimental cross sections apparently begin to level out. Sixteen hundred MeV should be a typical high-energy point since it is just beyond the known pion resonances. The cross section was not calculated below 190 MeV because of the uncertainty in the mean free path of the recoil neutron at very low energies.

The following angular distributions were used for these energies.

Table VI. Angular distributions used in one-step calculation.

Pion energy (MeV)[a]	$\frac{d\sigma}{d\Omega}$ $\frac{mb}{sr}$	Reference
190 (190)	$1+3\cos^2\theta$	62
370 (360)	$1.33+4.63\cos\theta+6.30\cos^2\theta$	66
1600 (1550)	$-0.4\cos\theta -2.4\cos^3\theta-4.2\cos^4\theta+8.\cos^5\theta+9.6\cos^6\theta$	49

[a]The energies in parentheses refer to the actual energies at which the angular distributions were measured.

The results of the calculation at these three energies are presented in Table VII along with the experimental results for comparison. The discussion of where in the nucleus the (π^-,π^-n) reaction takes place is given in Sec. IV. D.

Table VII. Results of $C^{12}(\pi^-,\pi^-n)C^{11}$ calculation.

T_π (MeV)	$\frac{d\sigma(0)}{d\Omega}$	$\frac{d\sigma(90)}{d\Omega}$	$\frac{d\sigma(180)}{d\Omega}$	$\sigma_{\pi,\pi n}(90)$	$\sigma_{\pi,\pi n}(180)$	$\sigma_{\pi,\pi n}$ (mb)	Normalized[a] σ (mb)	Experimental σ (mb)
190	4.0	1.00	4.0	4.6	30.5	14.1	87	68 ± 6
370	12.3	1.33	3.0	13.1	15.2	3.8	25	30 ± 3
1600	11.5	0.25	2.0	20.7	21.0	3.4	21	21 ± 5

[a]Results normalized to experimental σ at 1600 MeV

The calculated values all came out lower than the experimental values by a factor of about six. Normalization of the calculated cross sections to the experimental cross section at 1600 MeV, presumably the least sensitive energy, points out the similar energy dependence of the calculated and experimental values.

The magnitude of the calculated cross sections is strongly dependent on the values of the mean free path. Since the values of the effective πN cross section are rather uncertain, the mean free path might be in error, which could account for part of the discrepancy. The use of nonrelativistic kinematics also affects the mean free path. The recoil energies calculated relativistically differ by about 25% from the values calculated nonrelativistically at 190 MeV. This in turn affects the mean free path and the calculated cross section by roughly 25%. Although the error in recoil energy due to nonrelativistic kinematics will increase at higher energies, the mean free paths are much less sensitive to energy, so the error in cross section will still be less than 25%.

The approximations in the angular integration probably contribute to the error also. Small contributions to the (π^-,π^-n) reaction from forward-scattered pions would have a large weight due to the preponderance of forward scattering—especially at higher energies.

The approximation used to find the average distance the recoiling particles travel in order to reach the nuclear surface may also be responsible for the discrepancy. The two-dimensional average distance used here probably overestimates the distance needed to escape and tends to decrease the calculated cross sections.

The calculation outlined here is not a Monte Carlo type calculation. However, the nuclear model chosen here is equivalent to the nuclear model used by Metropolis et al. and suffers from the same approximation—namely, the lack of a diffuse surface.[31,23] Monte Carlo calculations of (p,pn) reactions have been low by factors of two to nine for a variety of target nuclei.[30,47] However, the Monte Carlo calculations do seem to give better agreement for light nuclei than for medium and heavy nuclei.[27]

Improved Monte Carlo calculations are in progress which use a trapezoidal model for the nucleus. Preliminary results seem to give (p,pn) cross sections which agree with the experimental values.[67] Hence it appears reasonable that use of a nucleon-density function with a more accurate surface would improve the (π^-,π^-n) calculation.

In view of the above uncertainties, the low magnitude of the calculated cross sections is not regarded as a serious indictment of the mechanism used to explain the $C^{12}(\pi^-,\pi^-n)C^{11}$ reaction. In fact, the similar energy dependence of the calculated and experimental cross sections is good evidence that the single-collision mechanism with both partners escaping directly is a valid description of the reaction mechanism.

1. Pions Plus Other Target Nuclei.

The nuclear model and calculation outlined above will probably have to be modified in order to account for $(\pi,\pi n)$ reactions in other light nuclei. Benioff found a strong correlation between the magnitude of the (p,pn) cross section and the number of "available" neutrons in light nuclei.[29] Preliminary data of Anderson and

Newman[68] seem to indicate that this correlation is even more pronounced in (π^-,π^-n) reactions on targets ranging from N^{14} to P^{31}.

To account for the fact that some neutrons may be "available" for a $(\pi,\pi n)$ reaction and others not, the factor for the probability of a collision in Eq. (12) could be modified. As expressed in Eq. (12) the probability of a collision occurring within a short path length Δx is: $P_{coll} = 1-\exp(-\Delta x/\lambda_{\pi n})$, where $1/\lambda_{\pi n} = \rho(\alpha\sigma_{\pi^- n})$ and ρ is the density of neutrons (taken to be half the nucleon density for C^{12}). The quantity α is assumed to be the same as that defined above for the effective πN cross section, because $\pi^{\pm}p$ angular distributions are so similar at energies near the $J = T = 3/2$ resonance. The quantity $\sigma_{\pi^- n}$ is the free-particle cross section. A simple change of ρ from the density of neutrons, to ρ^*, the density of available neutrons, might be sufficient to account for $(\pi,\pi n)$ cross sections as a function of mass. Gusakow notes a smooth correlation of (p,pn) cross sections as a function of mass for medium- and heavy-mass targets at energies of 100- and 400-MeV. This would seem to indicate that shell-structure effects are washed out above the light-mass region in contrast to the data of Markowitz.[30] It remains to be seen whether shell-structure effects occur in (π^-,π^-n) reactions on medium-mass targets.

2. Cause of (π^-,π^-n) Peak.

The term for the probability of a collision $[1-\exp(-\Delta x/\lambda_{\pi^- n})]$ is also responsible for the fact that the (π^-,π^-n) reaction gives a peak at the same energy as the free-particle scattering peak. For small Δx, the term is approximately $\Delta x/\lambda_{\pi^- n} = \Delta x\rho\alpha\sigma_{\pi^- n}$. Thus there is almost a linear dependence on the free $\pi^- n$ cross section. The mean free paths of the other exponential terms do not show the resonance behavior as sharply since they contain averages over the $\pi^- p$ and $\pi^- n$ cross sections. Also, the exponential factors for the incoming and outgoing pion tend to cancel each other's effect in the resonance

region. If the incoming pion is in the resonance region, for large scattering angles the scattered pion will ordinarily be out of the resonance region. Likewise, for incoming pions just beyond the resonance region, large-angle scattering shifts the outgoing pion down into the resonance region. Thus the product $P_i P_\pi$ is not as sensitive a function of energy as P_i and P_π individually.

D. Location of $(\pi^-, \pi^- n)$ Reaction

The above calculation points out very adequately another interesting feature of $(\pi, \pi n)$ reactions—that is, it serves to identify which regions of the nucleus contribute most strongly to the $(\pi, \pi n)$ reaction. The easiest way of showing these regions is to plot the relative contribution to the $(\pi^-, \pi^- n)$ reaction of each square in the semicircular matrix. Rotation of this semicircle about the axis parallel to the beam path and passing through the center of the nucleus causes the entire nuclear volume to be generated.

Figure 26a shows the probability of $(\pi, \pi n)$ events for the specific case of an incident pion of 370 MeV which scatters from a neutron at an angle of 180 deg in the center of mass. This figure gives rather striking evidence that at 370-MeV the $(\pi^-, \pi^- n)$ reaction is occurring predominantly on the surface of the C^{12} nucleus. Moreover, the surface facing the incident beam, the "front", contributes most strongly under these conditions. The calculations showed that for all energies and scattering angles, the $(\pi, \pi n)$ reaction occurred predominantly on the surface. A quantitative estimate of the depth of this surface region is quite uncertain due to the inadequacies of the nuclear model used. However, one can estimate that well over half of the $(\pi, \pi n)$ events occurred in a surface region whose depth was less than 0.2 of the nuclear radius.

Whether or not the $(\pi, \pi n)$ contribution comes from the front or back surface of the nucleus depends on the energy and scattering angle of the pion. For example, for 370-MeV π^- incident on C^{12} and

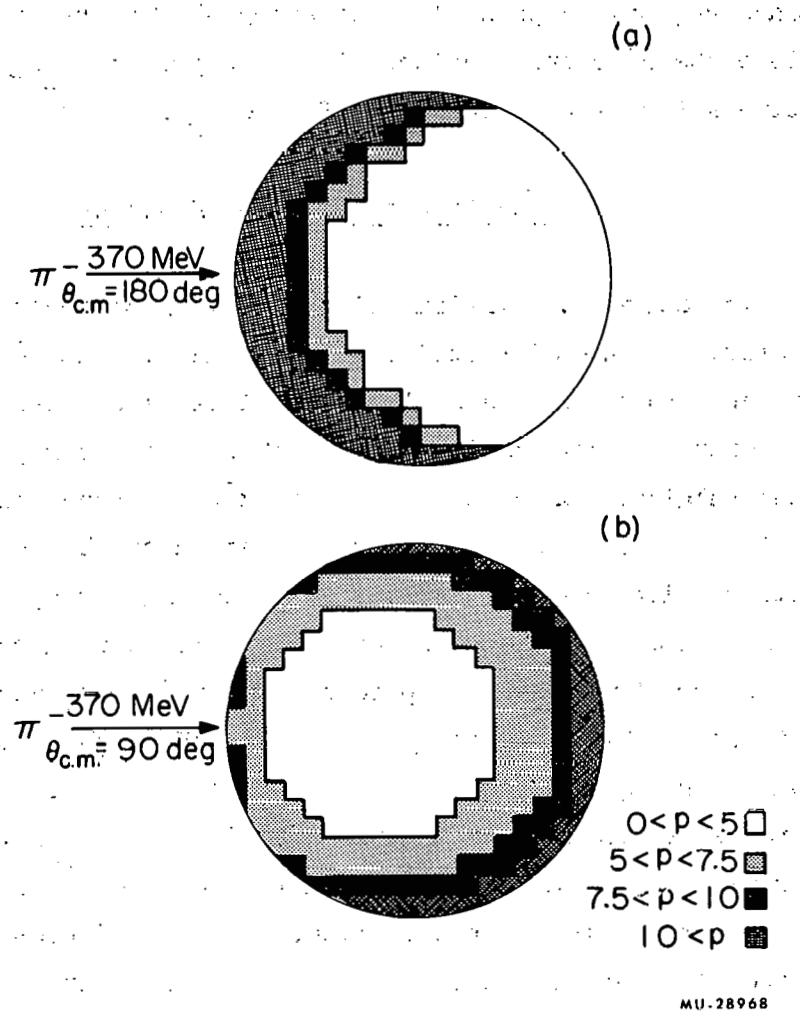

Fig. 26. Location of (π^-,π^-n) events from one-step model. This picture of the C^{12} nucleus represents a plane parallel to the beam path and through the center of the nucleus. p is the relative probability of (π^-,π^-n) event calculated from $p_{ij} = (P_i P_n P_\pi)_{ij}$.

(a) Incident pions of 370 MeV scattering at 180 deg c.m.

(b) Incident pions of 370 MeV scattering at 90 deg c.m.

scattering at 90 deg in the center of mass, the contribution to the $(\pi,\pi m)$ reaction is spread more uniformly over the nuclear volume but predominates at the back surface and polar regions, as shown in Fig. 26(b).

In general, for 180-deg scattering, the main contribution came from the front surface and pole tips. However, for 90-deg scattering, the main contributions came from the front surface only at 190 MeV while at higher energies the reaction occurs mainly from the back surface and polar regions. The angular distributions weighted the 180-deg scattering contributions more heavily than the 90-deg contributions, and the total yield from 90-deg events was usually less than the yield from 180-deg events. Therefore, one can generalize on the basis of this calculation that the $(\pi,\pi m)$ reaction takes place on the front surface and pole tips. Figure 27(a)(b)(c) shows the probable location of the $(\pi,\pi m)$ reaction after weighting the probability according to the angular distribution. The results of Fig. 27 are in distinct contrast with Benioff's calculation, which said that (p,pn) reactions occur on the back surface for GeV protons.[47,58] Since the mean free path of the pion is generally either considerably smaller or about equal to the mean free path of the neutron, the distance the pion travels in nuclear matter is the feature controlling the location of the $(\pi,\pi m)$ reaction. The pion travels the shortest distance when the reaction occurs on the front surface due to the dominance of 180-deg scattering in our calculation. Regardless of the assumptions about the scattering angle, the polar region is a dominant region at all energies for $(\pi,\pi m)$ reactions to occur.

The nuclear model and type of calculation performed here are simple and preliminary theoretical treatments of the $C^{12}(\pi^-,\pi^- n)C^{11}$ reaction. However, they do achieve their purpose in showing that the assumed reaction mechanism can explain the principal features

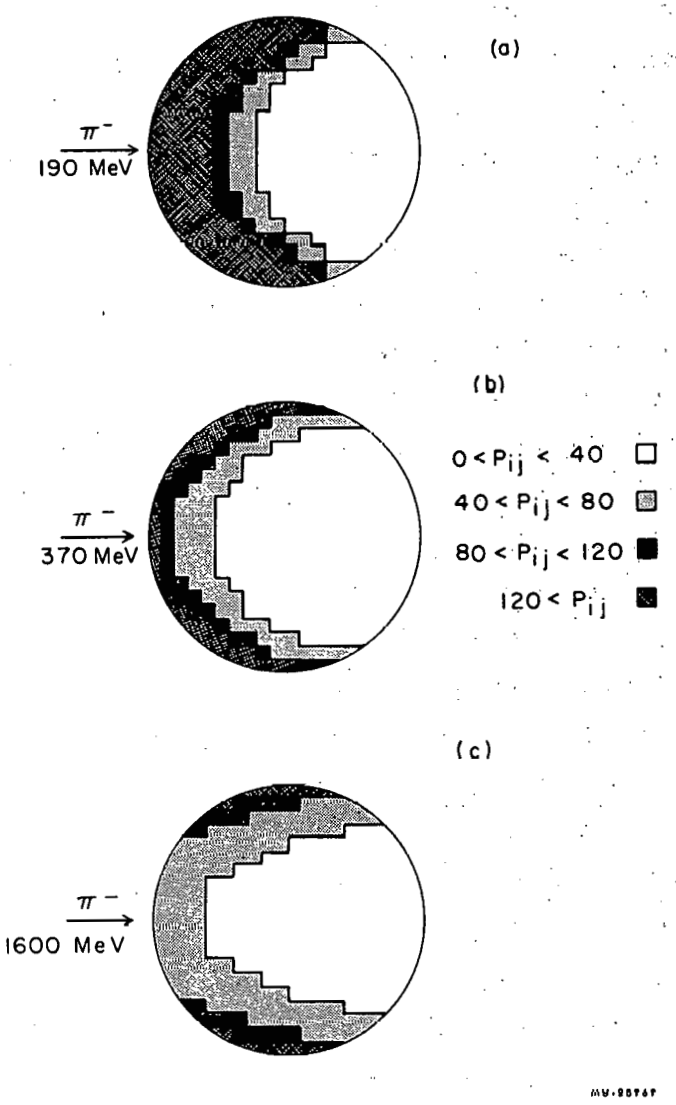

Fig. 27. Location of $(\pi,\pi n)$ events after integration over scattering angle θ. P_{ij} represents the relative probability of a $(\pi,\pi n)$ event [calculated from $P_{ij} = (P_i P_{coll} P_n P_\pi)$] after weighting by the angular distribution.

(a) Incident pion energy is 190 MeV.

(b) Incident pion energy is 370 MeV.

(c) Incident pion energy is 1600 MeV.

of the experimental excitation function—that is, the large peak at the same energy as the free-particle resonance and the comparatively flat excitation function at high energies. The calculation further indicates in a straight forward manner the localization in the target nucleus of the $(\pi^-, \pi^- n)$ events.

E. Two Step Calculation

1. Procedure and Results

The cross sections for the C^{12} $(\pi^-, \pi^- n)$ C^{11} reaction were also calculated by assuming the two-step mechanism. As discussed previously, the two-step mechanism assumes that the pion interacts with just one nucleon and then escapes from the nucleus. The recoil energy of the struck nucleon is converted into nuclear excitation energy and the nucleus eventually de-excites by evaporating just one neutron. We will ignore the possibility of the pion undergoing two collisions and escaping after leaving just enough excitation energy to evaporate one neutron.

The $(\pi^-, \pi^- n)$ cross sections were calculated from

$$\sigma(\pi^-, \pi^- n) = P_1 P_T \sigma_{geom} \quad , \tag{23}$$

where

P_1 is the probability that the incident particle makes one and only one collision in passing through the nucleus,

P_T is the probability that the struck particle receives a recoil energy between 19 and 29 MeV, sufficient to evaporate only one particle,

and σ_{geom} is the geometrical cross section of the C^{12} nucleus.

An analytic expression for P_1 as a function of the mean free path λ, has been given by Markowitz:[69]

$$P_1 = \frac{\lambda^4 - e^{-2R/\lambda}(2\lambda^2 R^2 - 2R\lambda^3 - \lambda^4)}{R^2\lambda^2} \tag{24}$$

where R is the nuclear radius. This expression is valid for cases where the incident particle scatters at 0 deg and continues on with the same mean free path as before the collision. These two

assumptions are not valid for πN scattering below the 190-MeV resonance region, but they become more accurate as the pion energy reaches the GeV region. For the sake of simplicity, we will use this expression for P_1 for the entire excitation function.

P_T is defined so that the recoil energy of the struck particle is sufficient to evaporate just one neutron from C^{12}. This excitation energy must be great enough to overcome the neutron binding energy of 18.3 MeV but not enough to evaporate a second particle. As defined here, P_T is an approximation to the evaporation formula of Eq. (2). This approximation ignores all effects due to the density of states and assumes that only a neutron is evaporated when the excitation energy is within the correct limits for single particle emission. However, it is also possible for a proton to be evaporated from the excited states of C^{12}. Thus this calculation will probably overestimate the $(\pi^-, \pi^- n)$ cross section. (In actual fact, the calculated cross sections came out lower by a factor of two than the experimental cross sections in the GeV region.)

The pion scattering angles corresponding to the nucleon recoil energies of 19 and 29 MeV were calculated from the relativistic equation, Eq. (6). The angular distributions for $\pi^- n$ elastic scattering were then integrated between these two angles and divided by the total elastic-scattering cross section to obtain the fraction of events that left the correct amount of energy.

The geometrical cross section of C^{12}, σ_{geom}, was calculated from πR^2 by using the value of R discussed previously. For $R = 3.04 \times 10^{-13}$ cm, $\sigma_{geom} = 290$ mb.

Table VIII presents the results of this calculation.

Table VIII. Two-step Calculation. ($\sigma_{geom.}$ = 290 mb for C^{12})

T_π (MeV)	P_l	P_T	$\sigma(\pi^-, \pi^- n)$ (mb)	Normalized σ[a] (mb)	Experimental σ (mb)
80	0.321	0.368	34.2	64.0	39 ± 3
127	0.180	0.099	5.16	9.65	56 ± 4
190	0.102	0.163	4.80	9.0	68 ± 6
245	0.18	0.102	5.33	10.0	61 ± 6
304	0.281	0.112	9.10	17.0	42 ± 4
373	0.335	0.112	10.9	20.4	30 ± 3
1000	0.322	0.051	4.80	9.05	20 ± 3
1610	0.335	0.116	11.22	21.0	21 ± 5

[a] Calculated results normalized to experimental σ at 1610-MeV

2. Comparison of One-and Two-Step Calculations with Experimental Results

The calculated cross sections were normalized to the experimental cross section at 1610 MeV and are plotted in Fig. 28 along with the values from the one-step calculation and the experimental excitation function. The two-step calculation does not predict a peak in the $(\pi^-, \pi^- n)$ cross sections at 190 MeV, whereas the one-step calculation does indicate a peak. The calculations show that although the two-step mechanism may be important at pion energies well below the resonance peak, the resonance peak itself is due to the one-step mechanism.

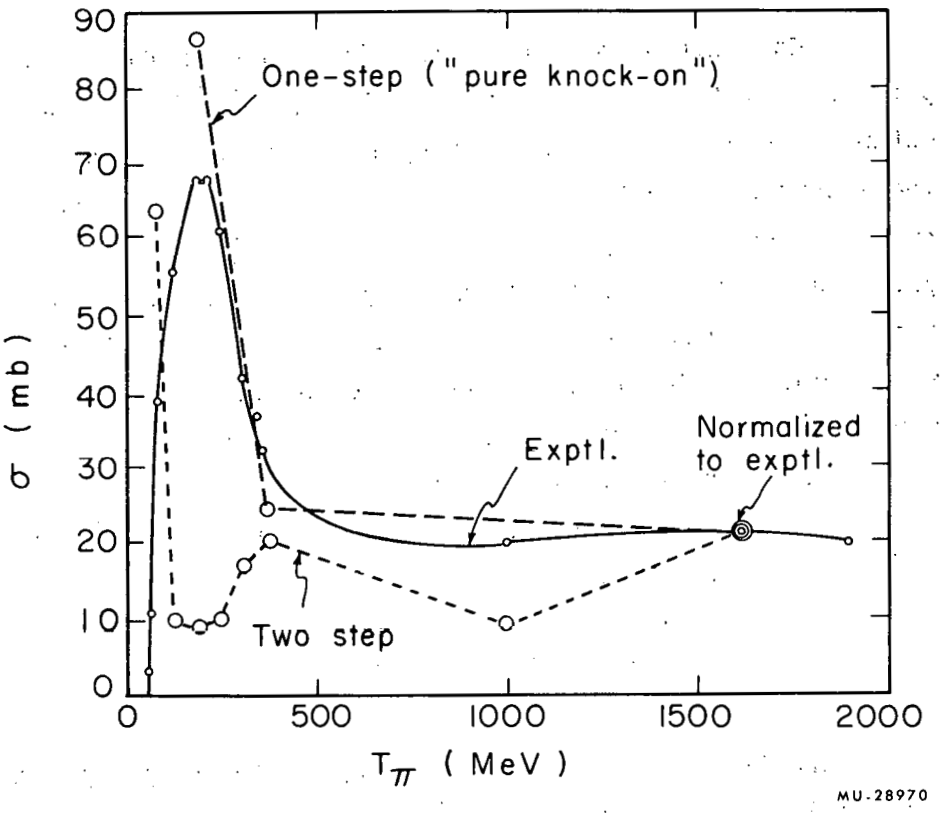

Fig. 28. Comparison of experimental and calculated $C^{12}(\pi^-,\pi^-n)C^{11}$ excitation functions. Solid curve is experimental. Dashed curve connects the cross sections calculated on the one-step model. The dotted curve connects the points calculated on the two-step model. Both calculated curves have been normalized to the experimental curve at 1610 MeV.

V. $C^{12}(\pi^+,\pi^+n)C^{11}$ REACTION

A. Discussion

Now that we have presented the evidence for the elementary-particle-collision nature of the $C^{12}(\pi^-,\pi^-n)C^{11}$ reaction, it is interesting to predict what the consequences of the one- and two-step mechanisms are for the $C^{12}(\pi^+,\pi^+n)C^{11}$ reaction. We shall show that the ratio of the (π^+,π^+n) cross section to the (π^-,π^-n) cross section provides a possible means of distinguishing the one- and two-step mechanisms. The ratio of the experimental $C^{12}(\pi^+,\pi^+n)C^{11}$ cross section at 110 and 73 MeV to the extrapolated values of the $C^{12}(\pi^-,\pi^-n)C^{11}$ cross sections at these energies will be compared to the predictions of the one-step and two-step mechanisms.

We first assume that the probability of a (π^+,π^+n) event can be given by the general expression [Eq.(1)]:

$$P_{(\pi^+,\pi^+n)} = P_i P_{coll} P_\pi P_n , \qquad (1)$$

as for the (π^-,π^-n) case. In the region of the $J = T = 3/2$ resonance, the angular distributions of π^+n and π^-n collisions are similar so that the recoil energy given the struck neutron is similar for both the (π^+,π^+n) and (π^-,π^-n) reactions. Therefore the probability of the neutron escaping will be the same for both reactions regardless of whether the one-step or two-step mechanism applies. Furthermore, for C^{12} the mean free path of the π^+

$$1/\lambda_{\pi^+} = \rho_n \sigma_{\pi^+n} + \rho_p \sigma_{\pi^+p}$$

will be the same as the mean free path of the π^-

$$1/\lambda_{\pi^-} = \rho_n \sigma_{\pi^-n} + \rho_p \sigma_{\pi^-p}$$

because $\sigma_{\pi^- n} = \sigma_{\pi^+ p}$ and $\sigma_{\pi^- p} = \sigma_{\pi^+ n}$ and because $\rho_n = \rho_p$.

Thus both P_i and P_π will be identical for π^+-andπ^--induced reactions. The only difference between the two reactions comes from the difference in the probability of a collision, P_{coll}. For the one-step mechanism this term is proportional to the elementary pion-neutron cross sections, whereas for the two-step mechanism this term is proportional to the sum of the pion-neutron and pion-proton cross sections. Thus:

One step

$$\frac{\sigma_{(\pi^+,\pi^+ n)}}{\sigma_{(\pi^-,\pi^- n)}} = \frac{P_i(\rho_n \sigma_{\pi^+ n}) P_\pi P_n}{P_i(\rho_n \sigma_{\pi^- n}) P_\pi P_n} = \frac{\sigma_{\pi^+ n}}{\sigma_{\pi^- n}} = \frac{1}{3} \text{ at peak.} \quad (25)$$

Two step

$$\frac{\sigma_{(\pi^+,\pi^+ n)}}{\sigma_{(\pi^-,\pi^- n)}} = \frac{P_i \left[\rho_n (\sigma_{\pi^+ n})_{el} + \rho_p (\sigma_{\pi^+ p})_{el} + \rho_n (\sigma_{\pi^+ n})_{ch.ex.}\right] P_\pi P_n}{P_i \left[\rho_n (\sigma_{\pi^- n})_{el} + \rho_p (\sigma_{\pi^- p})_{el}\right] P_\pi P_n}$$

$$= \frac{(\sigma_{\pi^+ n})_{el} + (\sigma_{\pi^+ p})_{el} + (\sigma_{\pi^+ n})_{ch.ex.}}{(\sigma_{\pi^- n})_{el} + (\sigma_{\pi^- p})_{el}} = \frac{12}{10} \text{ at peak.} \quad (26)$$

For the one-step mechanism the ratio of the $C^{12}(\pi^+,\pi^+ n)C^{11}$ to $C^{12}(\pi^-,\pi^- n)C^{11}$ cross sections should be in the same ratio as the free-particle cross sections over the $J = T = 3/2$ resonance region. Theoretical arguments based on isotopic spin rules predict that the free-particle cross sections should be in the ratio of 1/3 at the resonance peak.

As discussed more thoroughly in reference 70, there are three possible reactions for π^-N free particle scattering.

1. $\pi^- + n \rightarrow \pi^- + n$ elastic scattering
2. $\pi^- + p \rightarrow \pi^- + p$ elastic scattering
3. $\pi^- + p \rightarrow \pi^0 + n$ charge exchange scattering

If these reactions occur only in the T = 3/2 isotopic spin state, then theory predicts that the cross sections for these reactions should be in the ratio of 1:2:3 :: 9:1:2. The total $\pi^- p$ cross section is the sum of reactions 2 and 3 so the ratio of the total cross sections is

$$\frac{\sigma_{\pi^- p}}{\sigma_{\pi^- n}} = \frac{1 + 2}{9} = \frac{1}{3}$$

The principle of charge symmetry states that $\sigma_{\pi^- p} = \sigma_{\pi^+ n}$ so that

$$\frac{\sigma_{\pi^+ n}}{\sigma_{\pi^- n}} = \frac{1}{3}$$

Above the J = T = 3/2 resonance, the angular distributions of $\pi^+ n$ and $\pi^- n$ collisions begin to differ so that the pion and neutron recoil energies will be different. These differences are probably great enough to affect the mean free paths. Consequently we cannot expect the $(\pi^+, \pi^+ n)/(\pi^-, \pi^- n)$ ratio to follow the free-particle ratio so closely once the incident pion energy is above this resonance.

For the two-step mechanism, however, the probability of a collision (P_{coll}) is proportional to the sum of pion-neutron and pion-proton elastic cross sections. In addition, the $\pi^+ n$ charge-exchange process contributes to the $(\pi^+, \pi^+ n)$ product because evaporation of a proton from N^{12} gives C^{11} and evaporation of a neutron gives N^{11}, which would immediately β^+-decay to C^{11}. Charge exchange of a π^- cannot produce C^{11} from C^{12}. Thus the C^{12} $(\pi^+, \pi^+ n)$ C^{11} cross section should be greater than the C^{12} $(\pi^-, \pi^- n)$ C^{11} cross section at all energies where charge exchange is possible, provided the reaction mechanism is a two-step process. At the 190-MeV resonance, charge exchange is twice the elastic $\pi^+ n$ cross section and the ratio of C^{12} $(\pi^+, \pi^+ n)$ $C^{11}/C^{12}(\pi^-, \pi^- n)$ C^{11} should be 12/10 (See reference 70). These arguments do not apply at energies where the $\pi^+ p$ and $\pi^- p$ angular distributions have different shapes.

B. Results

Experimentally the $C^{12}(\pi^+,\pi^+n)C^{11}$ cross section was measured at 110 MeV by using the π^+ beam described previously in Sec. II. D-1. Except for the use of the singles counting rate in counter B as the beam monitor rather than the coincidence rate in counters A and B, the experiment was conducted exactly as for the π^- bombardments.

Three bombardments were performed with 110-MeV π^+ giving an average value of the cross section of 39.8 mb with a standard deviation of 0.5 mb. Inclusion of the other errors gives a cross section of 40 ± 4 mb.

By interpolation of the excitation function for the $C^{12}(\pi^-,\pi^-n)C^{11}$ reaction, the cross section is estimated to be about 52 mb at 110 MeV. Thus the experimental ratio is

$$\frac{C^{12}(\pi^+,\pi^+n)C^{11}}{C^{12}(\pi^-,\pi^-n)C^{11}} = \frac{40 \pm 4 \text{ mb}}{52 \pm 5 \text{ mb}} = 0.77 \pm 0.11$$

For the one-step mechanism this is to be compared with the free-particle ratio of

$$\frac{\sigma_{\pi^+n}}{\sigma_{\pi^-n}} = \frac{38 \text{ mb}}{77 \text{ mb}} = 0.50$$

For the two-step mechanism the expected ratio would be

$$\frac{(\sigma_{\pi^+n})_{el} + (\sigma_{\pi^+p})_{el} + (\sigma_{\pi^+n})_{ch.ex.}}{(\sigma_{\pi^-n})_{el} + (\sigma_{\pi^-p})_{el}} = \frac{17 + 77 + 21}{77 + 17} = 1.17$$

(The charge-exchange cross sections are from reference 71.) The experimental ratio tends to support the one-step mechanism, but does not exclude a partial contribution from the two-step mechanism.

There are several interpretations of this result. Assuming that both the experimental (π^+,π^+n) and (π^-,π^-n) cross sections are

correct as given, we could say that the reaction mechanism is a mixture of one-and two-step processes. However, there are two problems with the π^+-induced reaction that were not encountered with the π^- case. The following two sections deal with these problems.

1. Pion Absorption

Up to this point we have ignored the problem of π^+ absorption in our discussion of the C^{12} $(\pi^+,\pi^+ n)$ C^{11} reaction. In contrast to π^- absorption, where the "compound system", B^{12*}, cannot possibly lead to C^{11}, absorption of a π^+ gives N^{12*}, which can form C^{11} by emission of one fast proton. At 62 MeV, Byfield et al.[72] did a cloud-chamber study of the interactions of π^+ and π^- with C^{12}. Out of a total absorption cross section of 181 mb, they found that the cross section for single fast ($T \geq 40$-MeV) proton emission was 77 mb. This then represents the upper limit for the formation of C^{11} by this mechanism at this energy. In all probability, the cross section for C^{11} production by π^+ absorption is very much lower because 40 MeV is only a fraction of the total excitation energy available.

2. Muon Absorption

Another complication in the π^+ experiment comes from the possibility of μ^+ absorption. Muon absorption is a distinctly different process from pion absorption. Pion absorption occurs with a great deal of nuclear excitation due to the recoil of the two nucleons involved in the absorption event. The muon is most likely absorbed by one nucleon with most of the rest-mass energy being carried off by a neutrino. This results in very little nuclear excitation. Experimentally it was observed that in light nuclei, e.g., Ca and Mg, only about one neutron was emitted per slow negative muon absorbed.[73] This is consistent with Rosenblueth's calculation that slow μ^- absorption leads to an average nuclear excitation of about 15 MeV.[74] Other experiments showed that charged particles were very seldom seen

in slow μ^- absorption and that no high-energy γ rays are emitted.[75] Thus muon absorption will cause relatively little disruption of the target nucleus.

Absorption of slow μ^+ does not take place since the positively charged meson is repelled by the positive charge of the nucleus. However, fast μ^+ will easily pass through the Coulomb barrier (1.8 MeV for C^{12}). If a fast μ^+ is absorbed by C^{12} (although muons are weakly interacting) the resultant nucleus is N^{12} in an excited state. The excitation is probably enough to evaporate one nucleon, which produces either C^{11} or N^{11}. N^{11} would immediately decay by positron emission to C^{11}.

The 110-MeV π^+ beam used to measure the $(\pi^+,\pi^+ n)$ cross section was contaminated with about 12% μ^+ by the time it reached the plastic-scintillator target. With this flux it would require a cross section of about 100 mb for the production of C^{11} by μ^+ absorption in order to account for the increased C^{12} $(\pi^+,\pi^+ n)$ C^{11} cross section, if we assume solely the one-step process. However, the expected μ^+ cross section for this kind of reaction should be only about 1 mb.

3. Experiment at 73 MeV

In addition to the 110-MeV π^+ beam, a low-intensity 73-MeV π^+ beam was used to measure the C^{12} $(\pi^+,\pi^+ n)$ C^{11} cross section. One bombardment at this energy gave a cross section of 55 ± 20 mb, which is significantly higher than the corresponding cross section for the $(\pi^-,\pi^- n)$ reaction. By interpolation the $(\pi^-,\pi^- n)$ cross section would be about 25 mb at this energy. The large error on the $(\pi^+,\pi^+ n)$ measurement was caused by the low C^{11} activity due to the low-intensity π^+ beam. This beam had a 35% muon contamination, which is still insufficient to explain why the $(\pi^+,\pi^+ n)/(\pi^-,\pi^- n)$ ratio is much larger than the ratio of the free-particle cross sections when we assume the one-step mechanism is the only process contributing to the yield of C^{11}. At 73 MeV, the one-step mechanism predicts

$$\frac{\sigma(\pi^+,\pi^+ n)}{\sigma(\pi^-,\pi^- n)} = \frac{\sigma_{\pi^+ n}}{\sigma_{\pi^- n}} = \frac{15\text{mb}}{30\text{mb}} = 0.5$$

At 73 MeV the two-step mechanism predicts a ratio of

$$\frac{\sigma(\pi^+,\pi^+ n)}{\sigma(\pi^-,\pi^- n)} = \frac{(\sigma_{\pi^+ n})_{el} + (\sigma_{\pi^+ p})_{el} + (\sigma_{\pi^+ n})_{ch.ex.}}{(\sigma_{\pi^- n})_{el} + (\sigma_{\pi^- p})_{el}} = \frac{6+30+9}{30+6} = 1.25$$

The experimental ratio based on one bombardment at 73 MeV-π^+ is $55 \pm 20/25 \pm 5 = 2.20 \pm 0.91$ which tends to support the two-step mechanism. The $(\pi^+,\pi^+ n)$ data indicate that perhaps the two-step mechanism is important at lower energies, but that the one-step mechanism is more significant at the resonance energy. This corresponds roughly to the situation for the $C^{12}(p, pn)\,C^{11}$ reaction in which the one-step mechanism predominates above 250 MeV and the two-step mechanism is more significant below 100 MeV.

Because of the uncertainties about π^+ and μ^+ absorption and the limited number of bombardments, one should be cautious about drawing conclusions about the mechanism of the $(\pi^{\pm},\pi^{\pm} n)$ reactions from the π^+ data reported here. If future experiments can eliminate the effects of π^+ or μ^+ absorption or prove that they are negligible, comparison of the $(\pi^+,\pi^+ n)$ and $(\pi^-,\pi^- n)$ excitation functions should provide a means of distinguishing the relative importance of the one-step and two-step mechanisms.

VI. (p,2p) AND OTHER PROTON INDUCED REACTIONS

A. Introduction

Because the Monte Carlo calculations do not predict the correct magnitude or energy dependence of the cross sections for the simple reactions $Z^{A}(p,pn)Z^{A-1}$ and $Z^{A}(p,2p)(Z-1)^{A-1}$ and because of the use of "simple" reactions to probe the nuclear surface, there has been considerable interest over the past few years in studying the mechanisms responsible for these reactions. The (p,pn) reaction has been studied over a fairly large mass region whereas only limited data are available for(p,2p) reactions.

The reaction $Ce^{142}(p,2p)La^{141}$ has been studied carefully over the energy range from 60 MeV to 3.0 GeV.[76,77,78] The excitation function rises from 250 to 400 MeV and drops off by a factor of 10 at 3 GeV. However, there have been no cross sections measured in the interesting region of 400 to 1000 MeV.

Most (p,pn) excitation functions are almost independent of energy, from 0.3 to 6 GeV.[29,30] In the GeV region the reaction mechanism is thought to be predominantly a one-step process with some contribution from the two-step mechanism.

The original intention in studying proton-induced reactions was to obtain more data on the energy dependence and mass dependence of (p,2p) reactions to see if they followed the same behavior as for (p,pn) reactions. Then, as the possibility of using pion beams occurred, it became of interest to compare the pion-induced reactions with proton-induced reactions.

Targets of natural Zn and Fe metals were bombarded with 400-, 560-, and 720- MeV protons at the 184-inch cyclotron and at several energies up to 6.2 GeV at the Bevatron to determine the $Zn^{68}(p,2p)Cu^{67}$ and $Fe^{57}(p,2p)Mn^{56}$ cross sections. Natural metal targets were used for convenience and because thin foils could easily be obtained. A

radiochemical separation of the Cu activities was performed on the Zn targets, and likewise the Mn activities were separated from the Fe targets. The yield of Cu^{67} is expected to come mainly from the reaction $Zn^{68}(p,2p)Cu^{67}$. Zn^{68} has an isotopic abundance of 18.6% in natural Zn. However, Zn^{70} is also stable and has an isotopic abundance of 0.63%. It is possible that the presence of Zn^{70} in the target could contribute to the yield of Cu^{67} via a (p,2p2n) or (p,α) reaction. However, the fact that Zn^{68} is 30 times more abundant than Zn^{70}—coupled with the fact that most (p,pn) and (p,2p) reactions have larger cross sections by a factor of two or three than slightly more complicated reactions such as (p,2p2n)—means that the contribution of Zn^{70} to the yield of Cu^{67} is probably less than 2%. This is less than the precision of the experimental results. The probability of a high-energy (p,α) reaction on Zn^{70} that could also lead to Cu^{67} is expected to be quite small at the energies under consideration here. Secondary neutrons could possibly give Cu^{67} by an (n,p) reaction on Zn^{67}(4.1%), but the effect of secondary particles should be small for thin targets. The reaction $Zn^{67}(p,p\pi^{+})Cu^{67}$ could also produce Cu^{67}, but the maximum cross section for this type of reaction as calculated by Ericson et al. is only about 0.2 mb.[89] Because Zn^{68} is 4.5 times more abundant than Zn^{67}, we expect very little contribution to the yield of Cu^{67} from these interfering reactions. The isotopes Zn^{64} (48.9%) and Zn^{66}(28.8%) are too light to contribute to the yield of Cu^{67}. For the other Cu activities observed, Cu^{64} and Cu^{61}, there is no clear knowledge of which isotope of Zn was the target nuclide.

Among the Mn isotopes, Mn^{56} is expected to be a (p,2p) product of the reaction on Fe^{57}. Fe^{57} is 2.2% abundant among the natural iron isotopes, however Fe^{57} is also present to the extent of 0.33%. This means that Fe^{57} is only 6.7 times more abundant than a possible contaminating target nuclide. If we assume a factor of two difference between the (p,2p) cross section and the (p,2pn) cross section in favor of the (p,2p), then we expect a contribution of about 7.4% from the target nuclide Fe^{58}. Because the energy dependence of the

$Fe^{58}(p,2pn)Mn^{56}$ reaction is unknown, no correction for the contribution of Fe^{58} was made in this work.

The $(p,p\pi^+)$ reaction is a more serious problem in this case than in the Zn case. Because Fe^{56} is 41.6 times more abundant than Fe^{57}, the contribution to Mn^{56} from the $Fe^{56}(p,p\pi^+)Mn^{56}$ reaction may be important despite the low cross section ($\leqslant$ 0.2 mb). If we use the measured $Fe^{57}(p,2p)Mn^{56}$ cross section at 400 MeV of 50 mb, we estimate that the $(p,p\pi^+)$ reaction may contribute up to 15% of the Mn^{56} yield at higher energies. The Mn^{51} and Mn^{52} activities observed were assumed to have arisen from any of the stable isotopes of Fe. However, because Fe^{56} is 91.6% abundant it is likely that it was the major target nuclide for the other activities measured, Mn^{52} and Mn^{51}.

B. Experimental Methods

1. Targets

The targets for proton bombardment consisted of stacks of foils. The first three foils were .003-in.-thick Al; the middle foil of these three was used as a monitor of the proton intensity by counting the Na^{24} that was produced. The two foils on either side ensure that Na^{24} nuclei recoiling out of the middle foil were compensated by those recoiling in. The recoil effect was about 4%, as determined by comparing the yield of Na^{24} in the first and second foils. A sheet of pliofilm 120N2, 3.75 mg/cm^2 thick, separated the third Al foil from the Fe foil which was next in the stack. The Fe foil varied from 6 to 16 mg/cm^2 in thickness. Following the Fe foil was another sheet of pliofilm and then the Zn foil which was about 40 mg/cm^2. The pliofilm was used to prevent recoils from one foil contaminating the next foil. (See diagram.) The recoil loss is expected to be small for "simple reactions because of the small momentum transfer in such reactions.

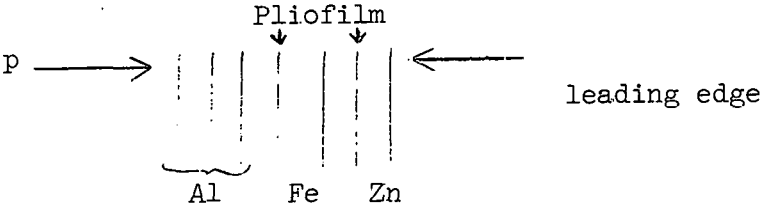

Once the target was assembled and placed in the target holder, the sides and leading edge were trimmed very carefully with scissors to ensure that the target foils were in perfect alignment. It was felt that this procedure gave better results than could be obtained by grinding or milling. With the target arrangement in use at the 184-inch cyclotron, most of the activity is produced at the leading edge of the target, so that it is extremely important that the leading edges be exactly aligned for each foil. At the Bevatron, the beam strikes more of the target, so that the alignment of the leading edge is not quite so critical. However, the same precautions were used for both the cyclotron and the Bevatron targets. After irradiation, the targets were brought back to the chemistry lab where the first cm—including the leading edge—was cut off carefully with scissors. This procedure assured that all the protons passing through the Al monitor foil also passed through the Fe and Zn target foils.

At the 184-inch cyclotron, targets which are to be bombarded with the internal proton beam are placed on a rod which can be driven to various positions along a radial line. The protons gain energy as they spiral out from the center of the cyclotron, reaching a maximum energy of 730 MeV at their largest orbit. Lower-energy protons can be obtained by driving the target closer to the center of the cyclotron. The protons then spiral out from the center until they strike the target at the desired radius. The target assembly, by stopping or scattering the beam, prevents the protons from continuing on out to greater radii and higher energies. The energy at a given position is probably known to about 5% (400±20MeV, 560±25MeV, 720±36MeV).

The Bevatron is a pulsed machine producing 10 pulses per min with about 2×10^{11} protons per pulse. The target holder is placed on a pneumatic ram that is shot into position at the end of each pulse. In between pulses and during the first part of the acceleration stage, the target is in a shielded position so that no low-energy protons can strike the target. Then at the end of the acceleration stage,

the rf accelerating field is turned off while the magnetic field continues to increase. The target is then rammed into position. The protons, which no longer are receiving any increment in energy, travel in orbits with smaller and smaller radii as the magnetic field increases—until they pass through the target. The maximum energy is 6.2 GeV. Lower energies are obtained by turning off the rf accelerating field at earlier times in the cycle.

2. Chemical and Counting Procedures

The chemical separations used for this work are described in Appendix C. The precipitates obtained at the end of the separation were mounted on a filter-paper disk by using a chimney and filter arrangement. The chimneys had an area of 2.41 cm^2, which defined the effective size of the β source. Four drops of a 4% solution of clear paint in ethyl acetate were placed on each precipitate to hold it in place during the drying and mounting stages of sample preparation. The filter paper and precipitate were dried under a heat lamp for a minute or so and then placed in the center of a 2.5- by 3.5-in. 300-mg/cm^2-thick Al card by using double-sided pressure-sensitive tape. Each sample was covered with a thin sheet of Videne TC plastic film, which was 1.34 mg/cm^2 in thickness.

All the samples from the proton bombardments were counted on end-window gas-flow β proportional counters to determine the radioactivities present through analysis of the decay curves. The counters are described in Appendix D, which also describes the method used to determine the counting efficiencies of the various isotopes.

After the activities had decayed, the samples were given to Dr. Huffman's analytical chemistry group who measured the yield of Cu and Mn in the Cu and MnO_2 precipitates, respectively, by using spectrophotometric and EDTA titrimetric methods.

3. Decay-Curve Analysis and Cross-Section Calculation

The activities were followed over a period of time long enough to give an accurate determination of the longest-lived com-

ponent present or until the activities reached background. The various components of the decay curve were resolved by the usual method of decay-curve analysis. Graphical methods gave sufficient accuracy for resolving up to three components.

The Cu decay curve could easily be resolved into 61-h Cu^{67}, 12.8-h Cu^{64}, and 3.3-h Cu^{61}. The Mn decay curve gave components belonging to 5.7-day Mn^{52}, 2.58-h Mn^{56}, and 45-min Mn^{51}. The experimental half-lives agreed with the values quoted in reference 18. Each component was extrapolated back to the end of bombardment to obtain the initial counting rate. The counting rates at end-of-bombardment time, A_o, were converted to disintegration rates, D_o, from the measured counting efficiencies of Appendix D, the decay scheme factors of reference 18, and the chemical yields. A saturation activity, D_{sat}, in disintegrations/min, was calculated by dividing the initial disintegration rate by the factor $(1 - e^{-\lambda t})$ where t is the length of bombardment and λ is the decay constant of the particular isotope. The saturation activity represents the decay rate of the isotope at the end of an infinitely long bombardment and is equal to the rate of formation $nI\sigma$, where n is the number of target nuclei per cm^2, I is the beam intensity in protons/min, and σ is the formation cross section in cm^2/target nucleus. Because both the Al foil and target foil are intercepted by the same beam

$$D_{sat}\ (Na^{24}) = n_{Al^{27}}\ I\sigma(Na^{24}), \qquad (27a)$$

$$D_{sat}\ (X) = n_{tgt}\ I\sigma\ (X), \qquad (27b)$$

where X stands for product nucleus and tgt stands for target nucleus. Dividing Eq. (27a) by Eq. (27b) and rearranging gives:

$$\sigma(X) = \frac{D_{sat}(X)}{D_{sat}(Na^{24})} \frac{n_{Al^{27}}}{n_{tgt}} \sigma(Na^{24}) \qquad (28)$$

Equation (28) was used to calculate the cross sections for proton-induced reactions. The cross sections for the $Al^{27}(p,3pn)Na^{24}$ monitor reaction decrease gradually from 10.7 mb at 400 MeV to 8.7 mb at 6 GeV.[84,87]

C. Results of Proton Bombardments

The resulting cross sections are given in Table IX for the reactions of protons with Zn, and in Table X for the reactions of protons with Fe. The first column lists the energy of the incident proton. The second column lists the cross section for the particular (p,2p) reaction. The other cross sections are listed in the third and fourth columns. The number in parentheses is the number of experiments used in determining the average value of the cross section. The uncertainty was calculated by taking the square of the standard deviation of the average value and the square of the absolute error, which was 10% of the average value. The square root of the sum of these squares is the uncertainty shown in the tables. The absolute error included the uncertainty in the monitor cross section, the uncertainty in counting efficiency, and the uncertainty in the decay schemes.

A distinction should be made between cross sections for reactions where the specific target nuclide is known and cross sections for reactions where several target nuclei contribute to the product. For this purpose we reserve the term "cross section" for the first case and the term "yield" for the second case.

The excitation functions are plotted in Figs. 29 and 30 to show the energy dependence of these reactions.

Table IX. Cross sections for production of Cu isotopes from Zn by p.

Energy (MeV)	$\sigma(Cu^{67})^a$ (mb)	$\sigma(Cu^{64})^b$ (mb)	$\sigma(Cu^{61})^b$ (mb)
400	17.8 ± 1.9 (7)	18.3 ± 2.0 (7)	28.4 ± 3.2 (4)
560	20.2 ± 2.1 (7)	15.7 ± 1.6 (7)	22.3 ± 2.4 (7)
720	26.0 ± 2.8 (5)	17.9 ± 2.0 (5)	22.8 ± 2.5 (5)
2200	21.0 ± 2.1 (2)	12.7 ± 1.4 (2)	14.8 ± 2.3 (1)
4000	19.2 ± 2.2 (2)	12.7 ± 1.3 (2)	14.3 ± 1.9 (2)
5700	19.8 ± 2.3 (2)	12.8 ± 1.6 (2)	13.0 ± 1.4 (2)
6200	23.6 ± 2.4 (2)	11.1 ± 1.3 (2)	12.9 ± 1.3 (2)

[a] Cross section calculated by assuming only Zn^{68} contributes.

[b] These results are "yields" because all isotopes of Zn contribute.

Table X. Cross sections for production of Mn isotopes from Fe by p.

Energy (MeV)	$\sigma(Mn^{56})^a$ (mb)	$\sigma(Mn^{52})^b$ (mb)	$\sigma(Mn^{51})^b$ (mb)
400	50 ± 6 (6)	11.6 ± 1.2 (6)	6.7 ± 0.9 (4)
560	57 ± 7 (7)	9.8 ± 1.0 (8)	5.9 ± 0.6 (6)
720	70 ± 13 (4)	8.4 ± 1.1 (4)	4.0 ± 0.4 (3)
2200	48 ± 8 (1)	5.0 ± 0.6 (1)	
4000	54 ± 6 (3)	5.9 ± 0.6 (3)	
5700	44 ± 7 (1)	5.4 ± 0.6 (1)	3.5 ± 0.5 (1)
6200	50 ± 7 (2)	5.0 ± 0.5 (2)	

[a] Cross section calculated by assuming only Fe^{57} contributes.

[b] These results are "yields" because all isotopes of Fe contribute.

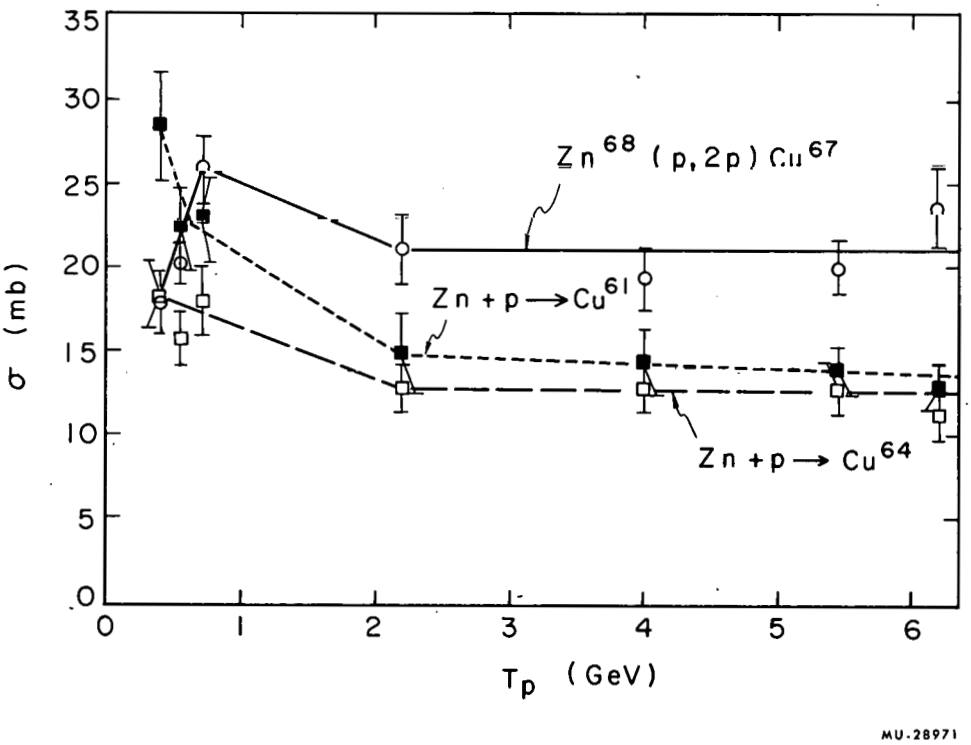

Fig. 29. Excitation functions for production of Cu isotopes from bombardment of Zn with protons.
Smooth curve ◘ is cross section for $Zn^{68}(p,2p)Cu^{67}$ reaction.
Dotted curve ■ is cross section for production of Cu^{61} from natural Zn target.
Dashed curve ⊟ is cross section for production of Cu^{64} from natural Zn target.

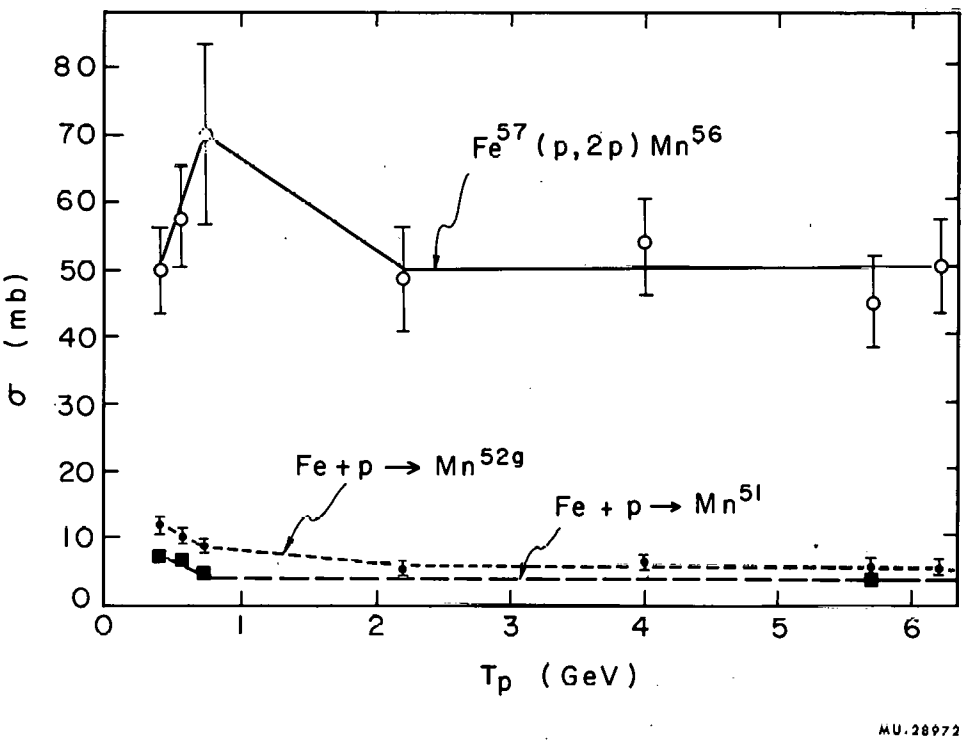

Fig. 30. Excitation functions for production of Mn isotopes from bombardment of natural Fe with protons.
Smooth curve ⊕ is cross section for $Fe^{57}(p,2p)Mn^{56}$ reaction.
curve ⊕ is cross section for production of Mn^{52} from natural Fe target.
Dashed curve ⊕ is cross section for production of Mn^{51} from natural Fe target.

D. Discussion of Proton Results

1. Complex Reactions

The excitation functions for the production of Cu^{64} and Cu^{61} from Zn, and for the production of Mn^{52} and Mn^{51} from Fe can be nicely explained in terms of the Serber Model[32] and the Monte Carlo calculations of Metropolis.[23] These four excitation functions exhibit the same general energy dependence. From 400 to 720 MeV there is a decrease in yield whereas above 2.2 GeV the yields are constant. The data for Mn^{52} have the highest precision since Mn^{52} is the first component to be resolved from the decay curve. Some Mn^{52} will be produced from a (p,2pn) reaction on Fe^{54}, but most of the Mn^{52} is produced by a (p,2p3n) reaction on Fe^{56} because of the greater abundance of Fe^{56} (91.6%) in natural Fe targets. (The symbol (p,2p3n) stands for any reaction involving a $\Delta Z = 1$ and a $\Delta A = 4$.) Therefore we will discuss the Mn^{52} excitation function in detail with the understanding that the discussion applies just as well to the other excitation functions.

As mentioned before, the Serber Model assumes that spallation reactions occur in two stages, the cascade step and the evaporation step. The Monte Carlo calculations of Metropolis[23] have been performed for the reaction of protons with Cu^{64}. The calculation shows that for the cascade step, the cross section for a mass change of one or two units decreases fairly rapidly in the energy region from 400 to 1000 MeV but decreases more slowly from 1 to 2 GeV. The residual nucleus at the end of this cascade has an average excitation energy of about 40 to 50 MeV, which is enough to evaporate several more nucleons. Moreover, the average excitation energy is relatively constant with increasing bombarding energy so that the average number of evaporated particles will be insensitive to the incident-proton energy. Thus the shape of the excitation function for a product nuclide 4 or 5 mass units from the target will be controlled by the cross section for the one or two nucleon-out cascade step.

An alternative mechanism for achieving an overall mass change of 4 would be a four nucleon-out cascade step, leaving the nucleus with very little excitation energy. However, the Monte Carlo calculations predict that the cross section for this type of cascade peaks at about 690 MeV and leaves the nucleus with an average excitation energy of over 100 MeV. In general, the greater the cascade, the greater the residual excitation.

We will assume that the calculation for protons with Cu^{64} is directly applicable to the reactions of protons with Fe^{56}. The experimental excitation function for the yield of Mn^{52} follows the same energy dependence as the one or two nucleon-out cascade in Cu^{64}. Thus we expect that Mn^{52} is produced by a mechanism involving the emission of one or two particles in the cascade step, followed by the emission of four or three particles in the evaporation step.

The yield of Mn^{51} includes the contribution of (p,pxn) reactions with all the Fe isotopes to produce Fe^{51}. The lifetime of Fe^{51} is probably so short that Fe^{51} nuclei decay to Mn^{51} before the chemical separation can be performed. No estimate of this contribution is possible from the data presented here. (This problem is not encountered in the case of Mn^{52} because the isomeric state Mn^{52m} shields the ground state from Fe^{52}.) The shape of the Mn^{51} excitation function is consistant with the expectations for a few-nucleon-cascade step followed by a few-nucleon-evaporation step.

The reactions of protons on Zn involve a shorter extrapolation from the Monte Carlo calculation. However, since natural Zn targets were used for these experiments, the target nuclide for Cu^{64} and Cu^{61} is not nearly as definite as with the natural Fe targets. Since there are several target nuclides, there are probably several reactions contributing to the yield, with each reaction having its own energy dependence. However, the general model of a few-nucleon cascade followed by nucleon evaporation is quite consistent with the observed excitation functions.

2. (p,2p) Reactions

The above discussion has intentionally avoided mentioning the $Zn^{68}(p,2p)Cu^{67}$ and $Fe^{57}(p,2p)Mn^{56}$ reactions. There are two distinctive features of these excitation functions, one being the unique energy dependence and the other being the difference in magnitude between the Cu^{67} and Mn^{56} cross sections. Examination of the (p,2p) excitation functions shows that both increase over the energy region from 400 to 720 MeV, followed by a constant behavior at higher energy.

There is a logical explanation for the cross-section increase in terms of the free-particle pp total cross sections. Above 400 MeV the total pp cross section increases from about 23 mb to about 43 mb at 720 MeV. If we interpret the mechanism of the (p,2p) reaction as being a pure knock-on collision between the incident proton and a proton of the target nucleus with little excitation left behind, we would expect the (p,2p) excitation function to follow the structure of the free-particle excitation function. Using the same notation as for the (π^-,π^-n) reaction, we can express the probability of a (p,2p) event by:

$$P_{(p,2p)} = P_i P_{coll} P_p P_{p'} , \qquad (29)$$

where P_p represents the probability of the incident proton escaping and $P_{p'}$ represents the probability of the struck proton escaping without further collisions.

For a small distance of travel, P_{coll} is given by

$$P_{coll} = 1-\exp\left[-\Delta x \rho(\alpha\sigma_{pp})\right] \approx \Delta x \rho(\alpha\sigma_{pp}) ,$$

where σ_{pp} is the free-particle pp cross section and α is the reduction factor to account for the Pauli exclusion principle and the momentum distribution of the struck proton. Since the cross section for (p,2p)

reactions is related to the integrated probability of a (p,2p) event over the nuclear volume, we see that $\sigma_{(p,2p)}$ is directly related to the free-particle cross section. The rise in the free-particle cross section above 400 MeV is less prominent in the (p,2p) reactions due to the momentum of the struck proton in the target nucleus. A calculation of this effect would be quite interesting but was not attempted in this work.

Previous work on (p,2p) excitation functions has not covered the energy region of 400 to 1000 MeV. Studies at Carnegie Tech showed that the cross section for (p,2p) reactions generally increase slightly with energy in the region from 200 to 400 MeV.[77,79] This is consistent with the energy dependence of the pp cross sections in this region. Morrison and Caretto[79] studied the $Zn^{68}(p,2p)Cu^{67}$ reaction from 130 to 425 MeV by using enriched isotopes of Zn^{68}. They measured a cross section of 20.8 ± 5.8 mb at 400 MeV compared with the value of 17.8 ± 1.9 mb at 400 MeV measured here. Figure 31 shows a plot of both (p,2p) excitation functions measured here, including the data of Morrison and Caretto. A smooth curve for the pp total cross section is also shown for comparison.

Rudstam et al. measured the yields of Mn isotopes from the bombardment of Fe with 340-MeV protons.[80] Their cross section for Mn^{52} fits smoothly onto the Mn^{52} excitation function obtained in this work, but the corresponding (p,2p) cross section is lower than the cross section measured here at 400 MeV by a factor of about two. (This is after correcting their data for the abundance of Fe^{57}.) Their yield of Mn^{51} is also lower than the data measured here, by a factor of two.

Another way of seeing the dependence of the (p,2p) reaction on the free-particle cross section is to plot the ratio of the (p,2p) cross section to the free-particle pp cross section as a function of energy. Figure 32 gives this plot for both the $Zn^{68}(p,2p)Cu^{67}$ and $Fe^{57}(p,2p)Mn^{56}$ reactions. Both sets of data show a decrease in this

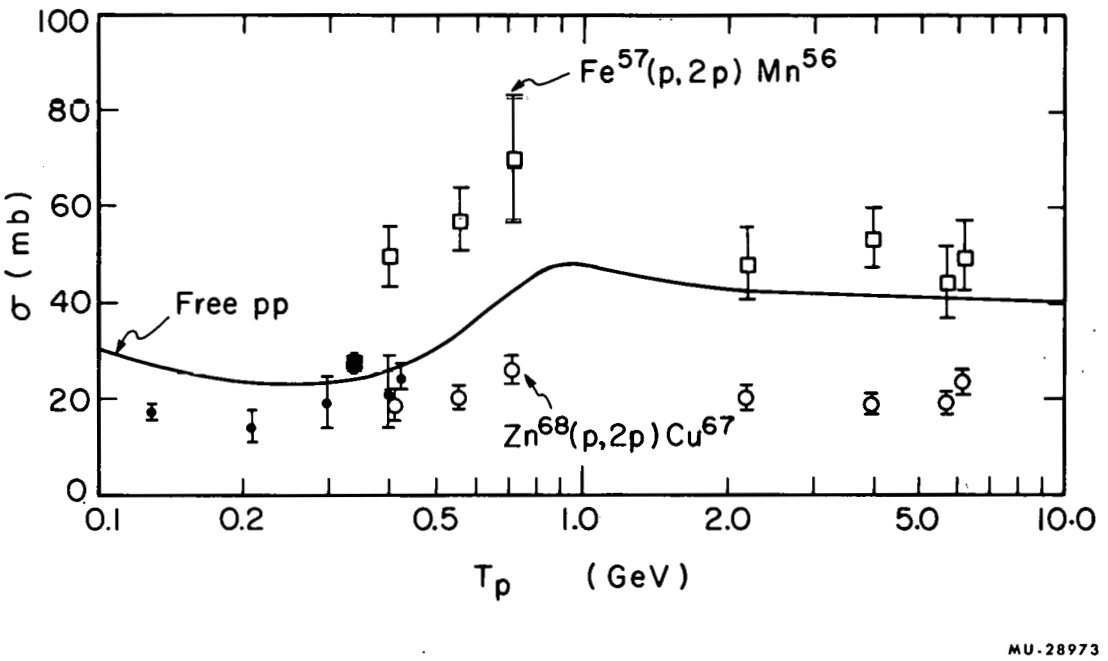

Fig. 31. Excitation functions for (p,2p) reactions.
Cross sections for $Zn^{68}(p,2p)Cu^{67}$ reaction: ⧗ measured here, ⧗ reference 79.
Cross section for $Fe^{57}(p,2p)Mn^{56}$ reaction: ⧗ measured here, ⧗ reference 80.
Smooth curve is free-particle pp cross section.

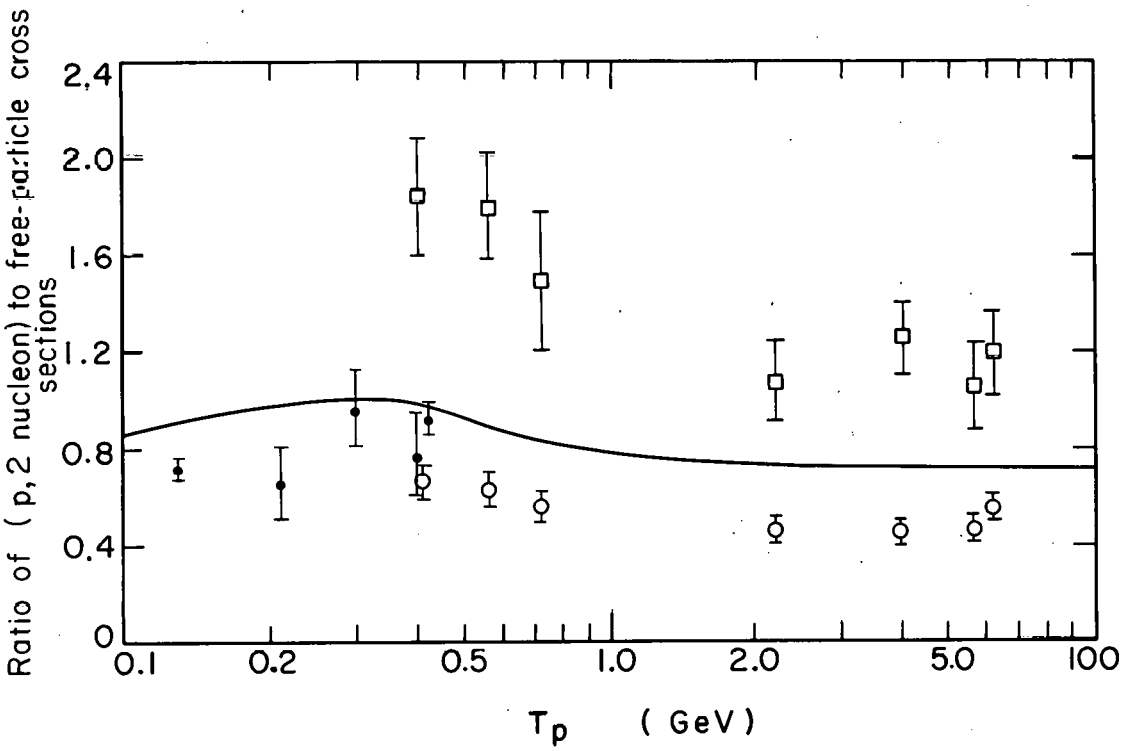

Fig. 32. Ratio of (p,2 nucleon) cross sections to free-particle cross section.
$\sigma[Zn^{68}(p,2p\ Cu^{67}]/\sigma(pp)$ for (p,2p): I measured here
I reference 79.
$\sigma[Fe^{57}(p,2p)Mn^{56}]/\sigma(pp)$ for (p,2p) measured here, I.
Smooth curve is $\sigma[C^{12}(p,pn)C^{11}]/\sigma(pn)$.

ratio from 400 to 720 MeV, followed by a constant ratio at higher energy. The smooth curve in the figure is the ratio of the $C^{12}(p,pn)C^{11}$ cross section to the free-particle pn cross section. The similar energy dependence of the (p,2p)/pp and (p,pn)/pn ratios is rather remarkable in light of the differences in pp and pn cross sections over the energy range of interest here, but fits well into the picture of a single collision of the incident proton with a single nucleon in the nucleus. The decrease in these ratios over the 400- to 1000-MeV region is ascribed to the difficulty of getting the newly produced mesons out of the nucleus without further interactions as mentioned previously in Sec. III.-C. The behavior of the (p,2p) excitation functions is thus consistent with the mechanism of a single pp collision occurring within the nucleus.

3. (p,2p) Magnitudes

The other feature of the (p,2p) reactions measured here is the difference in magnitude between the Cu^{67} and Mn^{56} cross sections. At high energies the Mn^{56} cross section is about 2.5 times the Cu^{67} cross section. This effect would be entirely unexpected from a smooth mass variation or liquid-drop model of the nucleus. The liquid-drop model would predict a larger (p,2p) cross section from a Zn target than from an Fe target simply because there are more protons in Zn. The rather large fluctuations in (p,2 nucleon) cross sections among neighboring nuclei has already been pointed out by Markowitz for (p,pn) reactions.[30] The explanation can be found in terms of the shell model.

From the previous discussion on the shape of the (p,2p) excitation function, we know that a pp collision occurs with both collision partners escaping without giving the nucleus enough excitation energy to evaporate additional particles. Cu^{67} lies just one proton above the closed proton shell for Z = 28 whereas Mn^{56} is midway between the magic numbers of Z = 20 and Z = 28. One might expect that

the binding energy of one proton above a closed shell is quite small, making it difficult to produce a Cu^{67} nucleus with insufficient excitation energy to evaporate another proton. However, looking at the proton binding energies in Cu^{67} and Mn^{56} as given by the Nuclear Data Tables, we find that the proton binding energies are almost identical, 8.52 MeV for Cu^{67} and 9.13 MeV for Mn^{56}. Furthermore, the neutron binding energy for Mn^{56} is 7.27 MeV, or about 1.8 MeV less than the neutron binding energy in Cu^{67}, so that one would expect it to be more difficult to form Mn^{56} at a low enough excitation. The α particle binding energies are quite similar for Cu^{67} and Mn^{56} so we conclude that binding-energy differences cannot be responsible for the differences in cross section.

4. Proton Availability

If we consider the number of "available" (as defined in Sec. III.-F) protons in the target nuclei, we notice a distinct correlation. Assuming that only the two protons beyond the closed shell of Z = 28 in Zn^{68} are available and that all six protons beyond the closed shell of Z = 20 in Fe^{57} are available, we would expect a ratio of 6/2 = 3/1 for the number of available protons. This predicts the $Fe^{57}(p,2p)Mn^{56}$ reaction to have three times the cross section for the $Zn^{68}(p,2p)Cu^{67}$ reaction, in agreement with the observed ratio of 2.5/1.

A shell state is considered to be available only when the difference between the binding energy of the protons in that shell and the binding energy of the topmost shell is less than the energy needed to evaporate other nucleons from the residual nucleus. Unfortunately, binding energies of buried shell states are known only for the light nuclei, and not for the mass region of interest here.[44]

If we assume that the foregoing analysis is valid, we can use experimental data to set limits on the differences between shell-state binding energies. For example, knowing that the $f_{7/2}$ protons in Zn^{68} are not available for a (p,2p) reaction tells us that the

difference in binding energy between the $f_{7/2}$ protons and the $2p_{3/2}$ protons in Zn^{68} is greater than about 8 MeV (the binding energy of an α particle, taken from Cameron's Mass Table[81]). Likewise, the 2s and 1d shells must lie more than 7.27 MeV below the $f_{7/2}$ shell in Fe^{57}, since the protons in these shells are not available for a (p,2p) reaction.

Much more experimental data is needed before we can be certain of the usefulness of (p,2p) reactions as a measure of buried-shell binding energies. Other effects, such as the density of states in the final nucleus, may influence the magnitudes of (p,2p) cross sections. The Nuclear Data sheets lists only the ground state for Cu^{67} whereas there are at least 15 states in Mn^{56} between the ground state and the particle-emitting states. Mn^{56} is an odd-odd nucleus so it probably does have more excited states than the odd-even nucleus Cu^{67}, but it may be that the excited states of Cu^{67} are not yet known.

VII. PION REACTIONS IN AL, CU, AND ZN

A. Introduction

A few experiments were performed to measure the yields of more complicated pion-induced reactions. Specific product nuclei were determined by radiochemically separating specific elements from the target material and measuring the radioactivities with low-background β counters. The "non-simple" pion-induced reactions are of interest for comparison with the Monte Carlo calculations and other theoretical treatments of high energy nuclear reactions.

Included in the cascade step of the Monte Carlo calculations are the effects of pion creation and reabsorption. The use of pions as a means of allowing large energy transfers was first proposed by Wolfgang and Friedlander to explain the mass-yield curve from interactions of protons with Cu at 2.2 GeV.[82] The short mean free path of pions in nuclear matter means that there is a high probability that a newly produced pion will be reabsorbed in the nucleus and give its rest-mass energy to the two nucleons participating in the absorption process. The subsequent scattering of these two nucleons is an efficient means of exciting the nucleus.[83]

Cumming et al. have found that for high-energy proton bombardments of light nuclei the cross sections for the production of various nuclei are constant with energy.[84] This is interpreted to mean that the energy-deposition spectrum is relatively independent of the incident-proton energy. It is possible that pion-nucleon isobars are formed which escape the light nuclei without giving extra excitation energy as the bombarding energy is increased. The interaction of pion-nucleon isobars within nuclear matter is not completely understood as of this writing.

Another high-energy process involving pions is called the fragmentation mechanism. This was proposed to account for the ejection of nuclear fragments of mass $10 < A < 50$.[83,85] The local "hot spot" necessary for the ejection of a fragment is presumably created by the

fast scattering and absorption of a pion in a time comparable to the time for a cascade. The comparison of pion-induced nuclear reactions and proton-induced reactions might provide information on the validity of the fragmentation mechanism.

The major emphasis in the following discussion should be placed on the techniques developed for studying complex reactions induced by pions. The data, results, and analysis are preliminary and introductory and should be evaluated as such. These studies are actively being continued at Berkeley.

B. Experimental Methods

1. Targets

Spallation products were measured from three different metal targets: Al, Cu, Zn. Large quantities of these metals are readily available in sheet form. The targets for meson bombardment consisted of stacks of 2.5-in.-diam disks. Thicknesses up to 0.25 in. were required to produce sufficient amounts of radioactivity from pion beams of intensity 10^6 π/min. The disks were obtained by turning down sheets of the metal on a lathe. In this way it was possible to obtain uniform targets with the exact diameter of the beam-defining counter.

Aluminum was chosen mainly to study the production of Na^{24}. The yield of Na^{24} in a piece of 3-mil Al has been widely used as a beam intensity monitor in proton bombardments. It was hoped that the reaction $Al^{27}(\pi^-,p2n)Na^{24}$ could serve as a similar monitor for pion-induced reactions once the excitation function was measured. But the radiochemical method for separation of milligram amounts of Na from gram amounts of Al described in this work is inconvenient and lengthy. The thickness of Al required to obtain measureable counting rates of Na^{24} make total-β counting of the original target impossible. Low-background γ counting of the original target was not tried in this work but ought to succeed.

Copper was chosen as a target because of the possibility of comparing the data for pion-induced reactions with the large amount of data available for proton-induced spallation reactions.[86] Copper has been a convenient target for many studies of spallation reactions despite the fact that natural copper has two stable isotopes, Cu^{63} and Cu^{65}.

The third target, Zn, was chosen in order to compare the $Zn^{68}(\pi^-,\pi^-p)Cu^{67}$ reaction with the reaction $Zn^{68}(p,2p)Cu^{67}$. If free-particle collision cross sections govern these reactions, the (π^-,π^-p) reaction should show some effect from the $J = T = 3/2$

resonance, and the (p,2p) should show the rise in cross section between 400 and 1000 MeV characteristic of pp total cross sections.

No separated isotopes were used for these experiments because of the large quantities of target material required. The metal targets were of high purity. The Al was 99.99% pure. The Cu showed less than 0.01% of Fe, Mn, and Ni when analyzed spectroscopically by George Shalimoff. The Zn was reagent grade supplied by A.D. Mackay Co. The total weight of target material in a given run was as much as 70 g for an Al target, 485 g for a Cu target, and 100 g for a Zn target. (Thus the radiochemical separation techniques could be classified as "bucket" rather than "micro.")

In most of the bombardments, the pion beam was monitored by using the counter telescope described in Sec.II-B. The same corrections for muon contamination and coincidence-counting losses were made as discussed previously. No correction was made for secondary particles produced in the targets themselves in these initial experiments.

After irradiation for many hours (8 to 20), the targets were walked, not run, back to the chemistry laboratory for chemical separation of the spallation products. A precipitate of NaCl was obtained from the Al targets, a precipitate of Fe_2O_3 was separated from the Cu targets, and precipitates of Cu, MnO_2 and NiO were obtained from the Zn targets. The chemical procedures are outlined in Appendix C. The final precipitates on filter paper were mounted on 1-in.-diam aluminum disks for counting in the low-background counters. Initial counting rates from these samples were seldom more than 100 counts/min and often less than 10 counts/min; this made decay-curve resolution and half-life determination difficult. After the activities had decayed to background levels, the samples were analyzed by members of Dr. Huffman's analytical chemistry group to determine the yield of the element involved.

2. Low-Background Counting

Because of the relatively low intensities of pion beams, special anti-coincidence equipment was designed for low-background β counting.

A successful counter, designed by Duane Mosier and Richard Leres, consisted of a standard β-proportional counter surrounded by a ring of 16 large brass Geiger tubes, each about 20 in. long and 2 in. in diameter. This entire assembly was surrounded by a Pb-brick cave, the inside of which was lined with 1/4-in. lucite. Every pulse in the ring of Geiger tubes generated a block pulse about 200 μsec long, which turned off the scaler that recorded counts from the β counter. Two clocks were available, one recording the total elapsed time and the other only the time the counter was actually on (live time). The background with this set-up was typically about 1.9 counts/min, compared with the usual β-counter background of 8 to 10 counts/min. The live time was 99% of the elapsed time and the efficiency was identical to the other β counters. An optional feature was the use of a scaler-gater blocking pulse to turn off the β scaler during the acceleration cycle of the Bevatron. This system was discussed earlier for the C^{11} counter. Use of the Bevatron blocking pulse cut the live time to about 97% and the background to about 1.6 counts/min.

To get more reliable low-background counting equipment, Ken Russel designed a transistorized counter based on a model used at Livermore. The detector consisted of a gas-flow β-proportional counter surrounded on top and sides by an Ampex tube giving pulses in anti-coincidence. Except for the high-voltage power supply and the scalers, all the components were transistorized. The detector was housed within an 18-in.-diam Pb shield. Two of these counters were made and placed in a room on the basement floor of the new chemistry annex about 150 feet further from the Bevatron than the old counting room. It was felt that the Bevatron would have less effect here because of the increased distance and because a hill separates the basement of the annex from the Bevatron. These counters had backgrounds of about 0.2 to 0.3 counts/min, but the β detection efficiency was only about 77% of the efficiency of shelf 1 on a regular β counter. The decreased efficiency was due to the lower solid angle. Sources for the new counters had to be prepared on 1-in.-diam disks rather than on the usual 2.5- by 3.5-in. Al counting card, but in all other respects mounting of the samples was the same.

3. Decay-Curve Analysis

The NaCl samples from the bombardment of Al showed no activity other than the 15-h Na^{24}, and a straight line could be drawn through the data. The Cu precipitate from the bombardments of Zn showed components characteristic of Cu^{67}, Cu^{64}, and Cu^{61}, and were resolved graphically. The Fe_2O_3 samples gave decay curves with several components in addition to 8-h Fe^{52}. These could be resolved into 5.7-day Mn^{52} and 2.58-h Mn^{56}. The MnO_2 samples from bombardment of Zn gave the Mn^{52} and Mn^{56} activities and also a shorter-lived activity probably due to 45-min Mn^{51}. To facilitate analysis of these decay curves, an IBM computer program (FRENIC) was used to give a least-squares analysis of the decay curves. The original program arranged by Rasmussen and Hoff for the Berkeley 704 has recently been revised by John Mahony and the computer group for use with the IBM 7090. This program allows both the half-life and initial activity of all the components to be varied in order to find a least-squares fit to the decay curve. Since the half-lives are well known for the isotopes studied here, they were kept constant and only the initial activities were allowed to vary.

C. Results of π^- -Induced Complex Reactions

The initial activity at end-of-bombardment was corrected for the efficiency of the counter at the given shelf position and source thickness; for the saturation factor $1 - e^{-\lambda t}$, and for the chemical yield. The efficiency of a given nuclide as determined in Appendix D was multiplied by 0.77 to obtain the corresponding efficiency of the transitorized low-background counter. The beam intensity was monitored with the counter telescope described in Sec. II-B. The cross sections were calculated from

$$\sigma(x) = \frac{D_{sat}(x)}{n_{tgt} I}$$

1. π^- + Al

Table XI gives the measured cross sections for the production of Na^{24} from Al^{27} by negative pions.

Table XI. Cross sections for the reaction $Al^{27}(\pi^-,p2n)Na^{24}$.

Incident-pion energy (MeV)	Measured cross section (mb)	Average cross section (mb)
127 ± 9	12.7	13 ± 3[a]
245 ± 10	3.3, 12.4, 4.8	7 ± 4
373 ± 10	7.5, 7.5, 9.2, 10.4	9 ± 2
423 ± 10	4.8	5 ± 1

[a]The pion beam was monitored by means of a calibrated ion chamber at 127 MeV only.

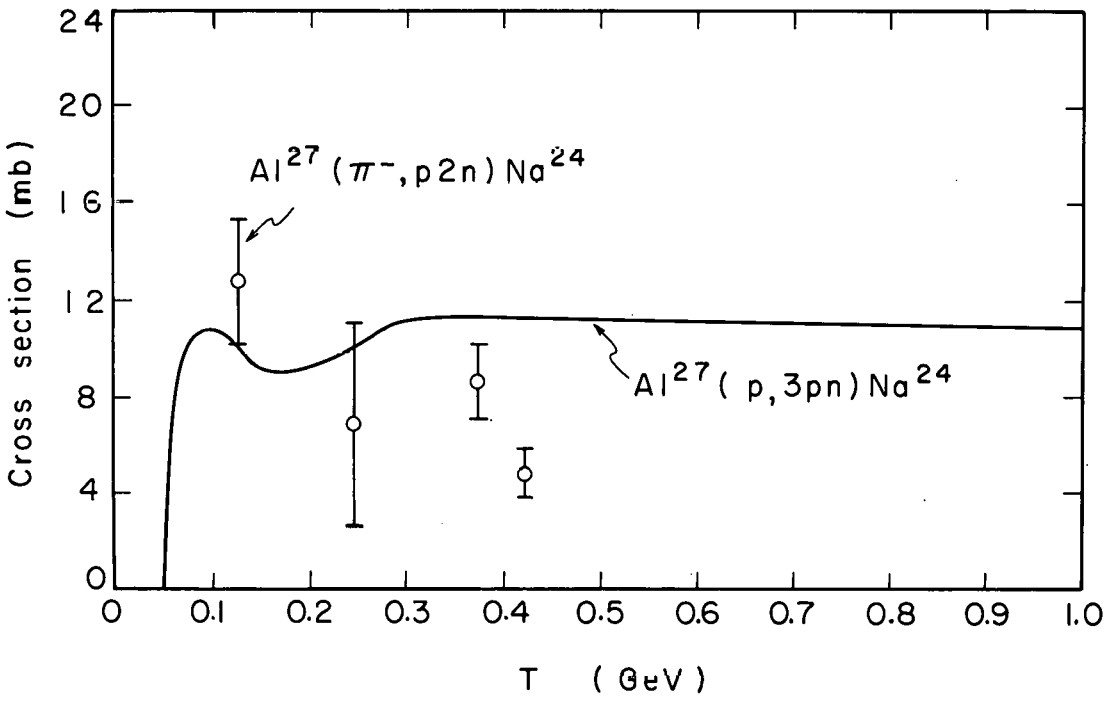

Fig. 33. Excitation functions for production of Na^{24} from Al.
Φ cross sections for Al^{27} $(\pi^-, p2n)Na^{24}$ reaction.
Smooth curve is cross section for $Al^{27}(p,3pn)Na^{24}$ reaction from data of reference 84 and 87.

These cross sections are plotted in Fig. 33 along with a smooth curve representing the cross section for production of Na^{24} from Al^{27} by protons. The pion data have large errors and are sparse making it premature to say anything definite about the excitation function for π^--induced production. One can say that the $Al^{27}(\pi^-,p2n)Na^{24}$ cross sections are of similar magnitude as the p-induced cross sections.

2. π^- + Cu

Table XII gives the cross sections for the reactions of pions on Cu. The cross sections are calculated with the assumption that both Cu^{63} and Cu^{65} contribute to the yield. The Mn and Fe activities were detected with the low-background β counters, while the Cu^{61} activity was measured by counting the 0.511-MeV annihilation radiation with a 3-by 3-in. NaI crystal. No special chemical separation for Mn was performed in the bombardments of Cu with pions. The Mn activities appeared in the Fe_2O_3 samples. It was assumed that the Mn activities had carried on the $Fe(OH)_3$ precipitates since no Mn holdback carrier had been added. In the calculation of the Mn cross sections, the chemical yield was assumed to be the same as the chemical yield for Fe.

The data of Table XII are based on only one experiment for each cross section. The error of 30 to 40% is determined from the errors in beam-monitoring, decay-curve resolution, and chemical-yield determination. The target for the 302-MeV data was a thin-Al can filled with CuO powder. The other runs were made with metal targets. The powder target was much easier to work with chemically and it is recommended that further experiments be performed with powder targets rather than the metal targets.

3. π^- + Zn

The cross sections for the reactions of pions with Zn are presented in Table XIII. The Cu^{67} cross section is based on the assumption that only Zn^{68} contributes to its formation. The cross section for Ni^{65} was calculated by assuming that all the isotopes of

Table XII. Cross sections for the production of various nuclides from the bombardment of Cu with negative pions.

Isotope	Incident-pion energy (MeV)	cross section (mb)
Cu^{61}	215 ± 40	21 ± 7[a]
Mn^{56}	215 ± 40	4.7 ± 1.3
Mn^{56}	245 ± 10	2.7 ± 0.9
Mn^{56}	302 ± 10	2.1 ± 0.7
Mn^{52}	245 ± 10	1.1 ± 0.4
Mn^{52}	302 ± 10	14.4 ± 5.0
Fe^{52}	215 ± 40	1.6 ± 0.5
Fe^{52}	245 ± 10	0.73 ± 0.3
Fe^{52}	302 ± 10	1.7 ± 0.5

[a] Cu^{61} was detected by counting the annihilation γ ray.

Table XIII. Cross sections for the production of various isotopes by the bombardment of Zn with negative pions.

Isotope	Incident-pion energy (MeV)	Measured cross section (mb)	Average cross section (mb)
Cu^{67}	302 ± 10	15.5, 17.1	16 ± 2
Cu^{67}	373 ± 10	23.4, 38.0, 56.3	39 ± 8
Cu^{64}	302 ± 10	9.25, 12.6	11 ± 2
Cu^{64}	373 ± 10	13.9, 16.5, 26.1	19 ± 4
Cu^{61}	302 ± 10	16.9, 17.3	17 ± 2
Cu^{61}	373 ± 10	18.7, 22.1, 26.4	20 ± 2
Mn^{56}	302 ± 10	5.3	5 ± 1
Mn^{52}	302 ± 10	8.22, 13.4	11 ± 2
Ni^{65}	245 ± 10	2.4[a]	2.4 ± 0.8

[a] The Ni^{65} cross section was calculated after assuming that all isotopes of Zn contribute to its formation except Zn^{64}. The total percent abundance of the applicable Zn isotopes was 51.1%.

Zn except Zn^{64} can produce Ni^{65}. The other cross sections are calculated on the basis that all Zn isotopes contribute to the yield. Again the 302-MeV data were obtained with an oxide target rather than a metal target. For the bombardment of pions on Zn, Mn carrier was added to the target solution and a specific chemical separation of Mn was performed.

The absolute yields of Cu^{64} and Cu^{61} can be compared with the relative yields presented by Turkevich and Fung for the absorption of slow π^- in $ZnCl_2$.[88] The following table gives the ratio of the Cu^{61} to Cu^{64} cross sections for the absorption of slow π^-, pion energies measured here, and for the bombardment of Zn with 400-MeV protons.

Table XIV. Ratio of Cu^{61} and Cu^{64} cross sections from bombardment of Zn.

Slow π^-	302-MeV π^-	373-MeV π^-	400-MeV p
0.80	1.57 ± 0.28	1.09 ± 0.24	1.55 ± 0.24

D. Discussion

The primary object in the bombardment of Zn with pions was to compare the $Zn^{68}(\pi^-,\pi^-p)Cu^{67}$ reaction with the corresponding $Zn^{68}(p,2p)Cu^{67}$ reaction. The pion data obtained at 373 MeV with metal targets was not very reproducible; the average value given in the table is probably not too reliable. However the two runs at 302 MeV that used a ZnO powder target were quite reproducible for all three Cu activities measured. Comparing the (π^-,π^-p) cross section to the (π^-p) total cross section at 300 MeV, we see that the ratio is $\frac{16 \pm 2}{30} = 0.53 \pm .07$. The value of the $Zn^{68}(p,2p)Cu^{67}/(pp)$ ratio shown in Fig. 32 is $0.66 \pm .07$ at 400 MeV.

This would indicate that the term for the probability of a collision, P_{coll}, dominates the expression for the probability of a "simple" event, $P_{(a,ab)}$. This is expected when reactions of this type occur on the nuclear surface. When a collision occurs on the surface, the particle involved will travel only short distances to escape the nucleus. Thus the differences in mean free path for pions and nucleons will not be too important in determining the relative yield for different "simple" reactions. However it is again necessary to obtain more experimental data to establish this relationship.

The production of isotopes more than one mass unit less than the target can be interpreted in terms of the Serber model.[32] A modification is necessary—to account for pion absorption. It is most probable that the incident pion will be absorbed after a few collisions inside the nucleus. The absorption is assumed to take place between two nucleons, and the rest-mass energy of the pion is divided between the two nucleons. The two recoiling nucleons will initiate a fast cascade and from then on the process is indistinguishable from a proton-induced cascade. From this model we speculate that the yields of pion-induced reactions do not differ greatly from the yields of proton-induced reactions when we consider "non-simple" reactions.

Table XV summarizes the non-simple reactions measured in this work and compares the yields with similar yields from proton reactions. In general, the yields from pion reactions agree with the yields from proton-induced reactions. The accuracy of the pion data is not sufficient to enable detailed conclusions to be drawn, but there does not seem to be a very strong dependence on the incident-pion energy.

It should be noticed that the yields of Cu^{64} and Cu^{61} from 300-MeV π^- + Zn are both lower than the corresponding yields from 400-MeV p + Zn. The absorption of a π in a Zn target nuclide means that no protons can be emitted if a Cu product is to be observed. For p + Zn, two protons along with several neutrons must be emitted, which opens up several more reaction channels. Thus we might predict slightly greater yields for the proton-induced reaction when the product nuclide is only one charge unit below the target nuclide. For product nuclei farther removed from the target, this effect is probably less important.

One other feature can be noticed from these data. Let us assume that the reactions π^- + Zn^{64} and p + Cu^{63} form highly excited compound systems of Cu^{64*} and Zn^{64*}, respectively. At the high excitation energies considered here the difference in charge of these two "compound nuclei" is relatively unimportant in determining the numbers of protons and neutrons emitted in the de-excitation process. Thus we would expect the yields from these two reactions to be almost identical. Zn^{64} composes 48.9% of the Zn target, and Cu^{63} composes 69% of the Cu target, so the data given here may be suitable for a comparison of this type. From the data of Table XV we see that the yields of Mn^{52} and Mn^{56} are 11 and 5 mb for the case of 300-MeV π^- on Zn, and 7.1 and 2.5 mb for 340-MeV p on Cu. The magnitudes of the proton cross sections are slightly lower than the pion cross sections, but the ratio of the Mn^{52}/Mn^{56} yields (2.2 ± 0.6 in the pion case and 2.8 ± 0.6 in the proton case) are similar within the experimental error.

From the limited amount of data presented here, one cay say that, in general, pion-induced reactions do not behave differently from proton-

Table XV. Comparison of yields for "non-simple" pion- and proton-induced reactions. σ is given in mb.

Reaction	Cu^{64}	Cu^{61}	Ni^{65}	Mn^{56}	Mn^{52}	Fe^{52}
215 MeV π^- + Cu		21		4.7		1.6
245 MeV π^- + Cu				2.7	1.1	0.73
302 MeV π^- + Cu				2.1	14	1.7
245 MeV π^- + Zn			2.4			
302 MeV π^- + Zn	10	17		5.3	11	
373 MeV π^- + Zn	18	20				
340 Mev p + Cu[a]		23		2.5	7.1	0.18
400 MeV p + Zn	18	28				
400 MeV p + Fe					11.6	
340 MeV p + Fe[b]					12.9	

[a] Data from reference 86.

[b] Data from reference 80.

induced reactions for targets and products in this mass region. The major significance of this remark comes from consideration of the various theories for energy transfer in proton-induced spallation reactions. The production and reabsorption of pions has been often proposed as the mechanism of energy transfer for high-energy nuclear reactions. The experimental evidence given here indicates that the energy deposition from pion- and proton-induced reactions is quite similar. This supports the hypothesis that pion processes play a major role in high-energy nuclear reactions.

The influence of pions in the fragmentation process is still unknown. To clarify this point it would be necessary to obtain cross sections for production of much lighter fragments than measured here.

VIII. SUMMARY AND CONCULSIONS

The most significant feature of the experimental results described in this thesis is the appearance of free-particle-like collisions within nuclear matter. Quasi-free-particle scattering has been investigated in many laboratories around the world by using proton beams and measuring two outgoing protons in coincidence. Major accomplishments of the (p, 2p) coincidence experiments have been the determination of the binding energy of shell-model states in light nuclei, and the determination of the momentum distributions of protons in nuclei. However similar and complimentary effects can be discovered by using techniques to measure the residual nucleus after a simple reaction has occurred. The $(\pi^-,\pi^-\ n)$ reaction studied here is an example of such a technique.

First we will summarize the free-particle effects discovered in this work and then list the applications of $(\pi,\pi\ n)$ reactions.

A. Summary of Free-Particle Effects

The measurement of the C^{12} $(\pi^-,\pi^- n)$ C^{11} excitation function showed a peak at the same incident-pion energy as the resonance in free-particle $\pi^- n$ scattering. This peak is in distinct contrast to the C^{12} (p, pn) C^{11} excitation function, which shows no peak in this energy region and where no resonance exists in the free-particle pn cross sections. Arguments based on the recoil energy given the struck neutron show that the pion peak is not due to the incident pion having the same momentum as the proton at the (p, pn) peak. A simple calculation, based on the assumption of a single $\pi^- n$ collision after which both collision partners escape directly, reproduced the shape of the experimental excitation function. The fact that the calculated values were lower than the experimental values by a constant factor is attributed to the approximations employed and the defects in the nuclear model. The calculation showed, in addition, that the greatest contributions to the $(\pi^-,\pi^- n)$ reaction came from the nuclear surface.

The experimental excitation function for the Zn^{68} (p, 2p) Cu^{67} and Fe^{57} (p, 2p) Mn^{56} reactions showed structure similar to the free-particle pp total cross sections. The free-particle pp cross sections have a rise from 400 to 1000 MeV and then decrease to a constant value in the GeV region. The (p, 2p) reactions show similar behavior. In contrast the (p, pn) excitation functions do not show this behavior because the free-particle pn cross sections are relatively constant in the 400- to 1000-MeV region.

At 300-MeV incident-pion energy the ratio of the Zn^{68} $(\pi^-,\pi^- p)$ Cu^{67} cross section to the free-particle $\pi^- p$ cross section is almost the same as the ratio of the Zn^{68} (p, 2p) Cu^{67} cross section to the free-particle pp cross section. This is to be expected if free-particle scattering is the controlling feature of both the $(\pi^-,\pi^- p)$ and (p, 2p) reactions. However, more information is needed about the energy dependence of the $(\pi^-,\pi^- p)$ reaction before this can be firmly established.

Data on the C^{12} $(\pi^+,\pi^+ n)$ C^{11} reaction ought to give evidence concerning whether the $(\pi^+,\pi^+ n)$ reactions proceed by the one-step or two-step mechanism provided experimental complications can be overcome. The tentative results obtained here are inconclusive on this point. However both mechanisms assume an initial πN collision, so that the basic premise of the impulse approximation is still preserved regardless of which mechanism applies.

B. Uses of $(\pi^-,\pi^- n)$ Reaction

Once the mechanism of the C^{12} $(\pi^-,\pi^-$ n) C^{11} reaction is firmly established, the reaction may be applied to several other problems in nuclear physics.

The resonance peak in π^-n scattering is considerably broadened when the neutron is moving within the potential well of the nucleus. This broadening can be calculated provided the momentum distribution of the neutrons is known. Starting with the experimental peak, one could infer a momentum distribution for the neutrons in the "available" shell-model states.

By using the concept of available states and studying the $(\pi^-,\pi^-$ n) reaction as a function of target mass, it may be possible to put limits on the binding energy of various shell-model states.

Any theoretical treatment of the $(\pi^-,\pi^-$ n) reaction is sensitive to the value of the mean free path for pions in nuclear matter. If a suitably accurate model and detailed computer calculation were attempted, the experimental $(\pi^-,\pi^-$ n) cross sections could be used in determining the mean free path and effective cross sections in nuclear matter.

The C^{12} $(\pi^-,\pi^-$ n) C^{11} reaction can be used as a monitor of pion intensities for pion-induced reactions in other target nuclei. The plastic-scintillator technique is quite straightforward and reliable and the C^{11} half-life is convenient for short bombardments. This will enable determination of other monitor reactions for longer bombardments without the necessity of counting the beam directly.

Ericson et al. have discussed the use of low-momentum transfer reactions as a means of obtaining $\pi\pi$ cross sections by radiochemical techniques.[89] The method assumes that peripheral collisions occur within nuclear matter between the incident particle and one nucleon. The C^{12} $(\pi^-,\pi^-$ n) C^{11} reaction studied here gives evidence that

elementary-particle collisions do occur in nuclear matter. This provides the experimental evidence they require to support their mechanism for low-momentum transfer reactions. Pion-pion cross sections can be obtained from data on pion exchange reactions ($\Delta Z \leq 1$, $\Delta A = 0$) by comparison of the pion-induced cross section to the proton-induced cross section at the same c.m. energy.

C. Comparison of Pion-and Proton-Induced Reactions

The data presented here for spallation reactions caused by pions are quite limited, but the yields are similar in magnitude to yields from proton-induced reactions with the same element. The assumption that pions are absorbed and the ensuing cascade is equivalent to a proton-induced cascade is consistent with the data. The Monte Carlo calculations currently being carried out at Brookhaven use the assumption that the pion quickly forms an isobar and travels through nuclear matter coupled to a nucleon. It would be necessary to obtain much more extensive data to check this assumption. More data are also needed to investigate the fragmentation mechanism.

To summarize: a little is known, much is unknown.

ACKNOWLEDGEMENTS

I wish to thank my research director Professor Samuel Markowitz for suggesting these topics and for his guidance throughout the course of this study.

I am grateful for valuable discussions with Dr. John Alexander, Dr. Homer Conzett, Dr. Burton Moyer, Dr. Virendra Singh, Dr. Bhalchandra Udgaonkar, and Dr. Kenneth Watson concerning various theoretical aspects of this research.

This work could not have been performed without the cooperation of the physicists responsible for the many pion beams. Unfortunately their names are too numerous to mention individually, but I am grateful to them all.

The helpful discussions over experimental problems with Dr. Daniel Horen, Barry Barish, Richard Kurz and Bruce Wilkins are gratefully acknowledged.

Special thanks go to Richard Chanda for the use of his fast-slow coincidence system, to George Kilian, Duane Mosier, and the electronics group, for the setup and maintenance of the electronic equipment; to James Vale and the cyclotron crew, for the bombardments at the 184-in. cyclotron; to Walter Hartsough and the Bevatron crew, for similar services at the Bevatron; to Health Chemistry for the transportation of targets and concern over my welfare; to George Shalimoff for spectral analysis of various samples; and to Dr. Eugene Huffman and the analytical chemistry group for determination of the chemical yields.

The aid and assistance of David Anderson, Roger Newman and Arthur Pape with pion bombardments is deeply appreciated, as is the critical reading of this manuscript by D.A. and R.N.

The discussions and contacts with many friends and associates at the Lawrence Radiation Laboratory have been of infinite value to my education in life and science.

This work was performed under the auspices of the U.S. Atomic Energy Commission.

APPENDICES

A. Free-Particle Total Cross Sections

The following four figures are free-particle total cross sections taken from the literature.

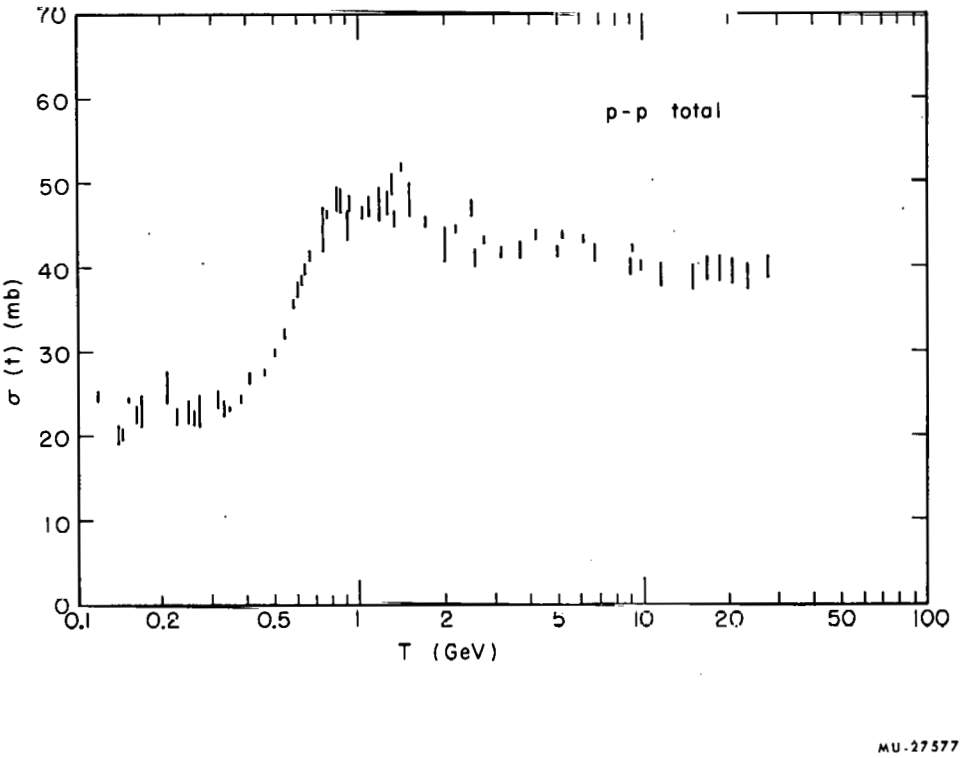

Fig. A-1. Free-particle pp cross sections (from graph by Glassgold[96]).

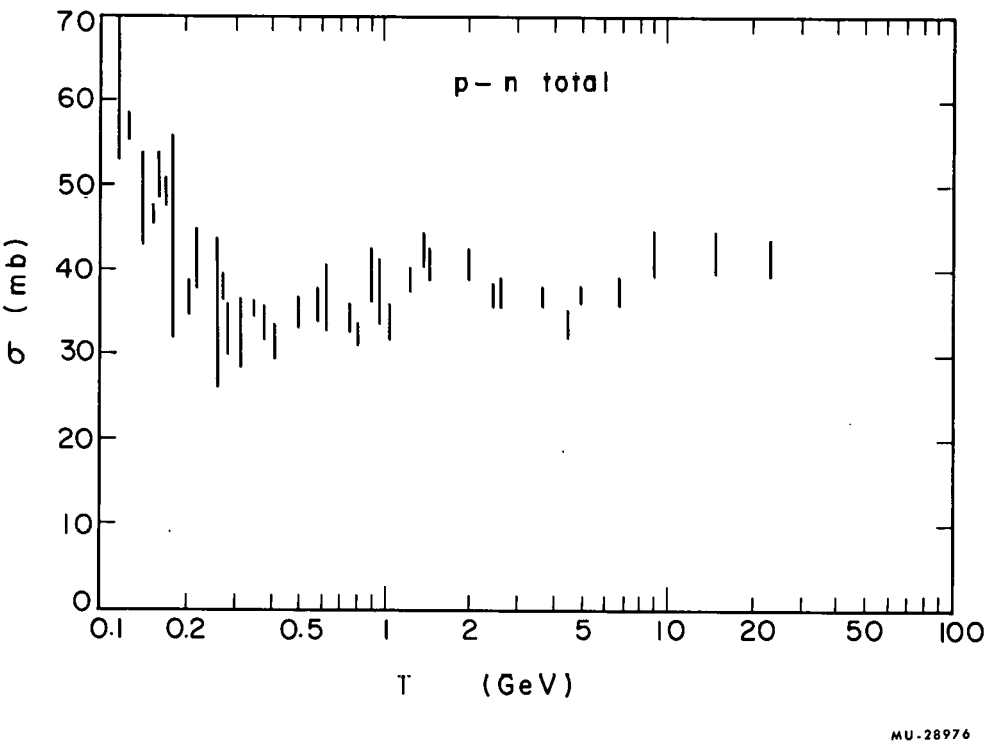

Fig. A-2. Free-particle pn cross sections(from data collected in reference 97).

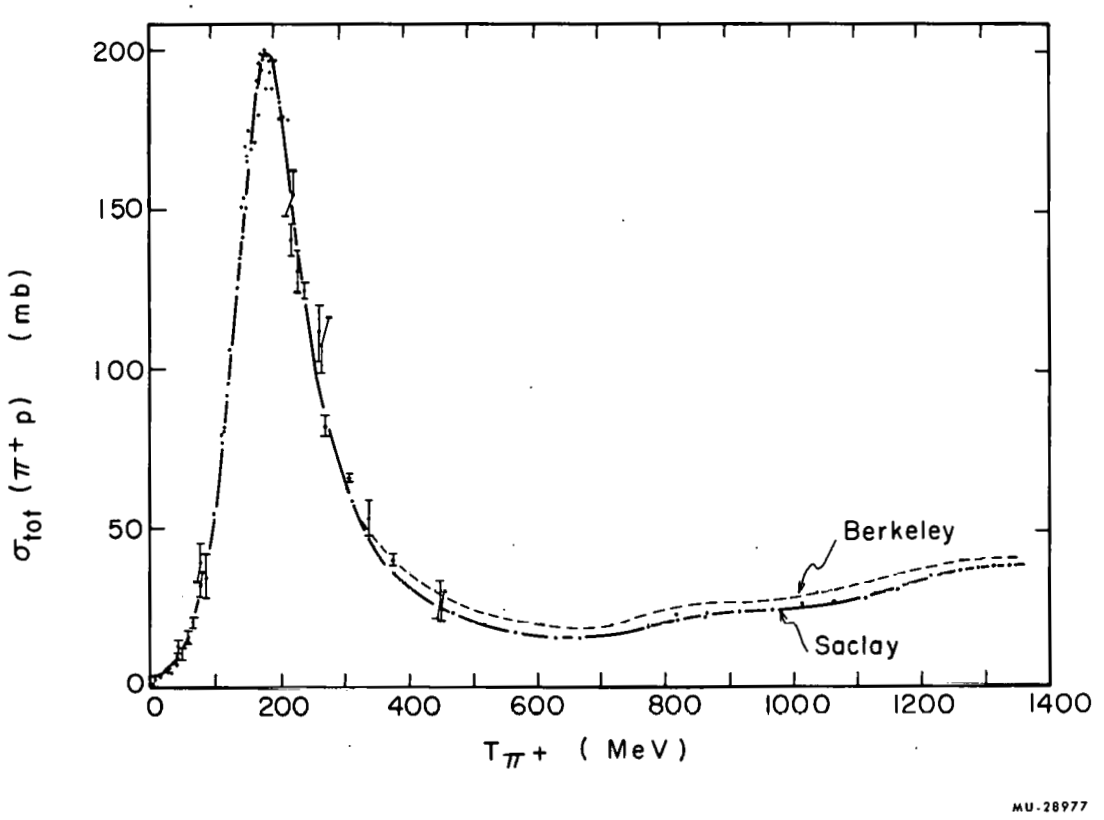

Fig. A-3. Free-particle π^+p cross sections (from data collected in reference 97).

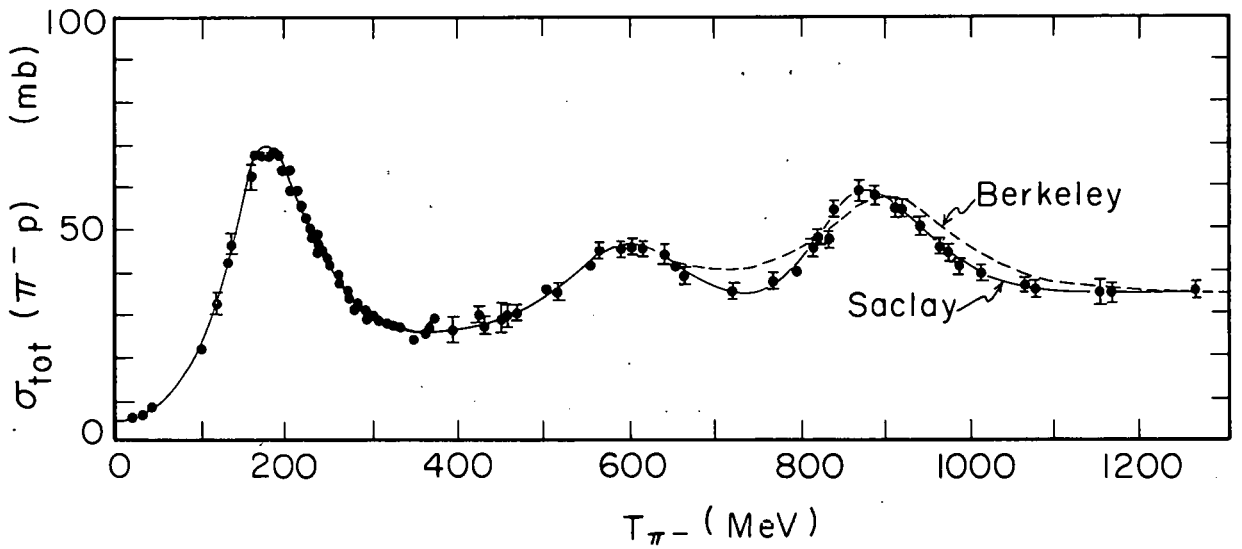

Fig. A-4. Free-particle π^-p cross sections (from data collected in reference 97).

B. Correction for π^- Decay to μ^-

The μ^- and ν from the decay of a π^- are emitted at 180 deg to each other in the c.m. frame of reference. Assuming that the μ^- is isotropic in the c.m. coordinate system, we want to calculate the solid angle subtended by a counter at some distance r from the point of decay. The solid angle in the c.m. system when divided by 4π gives the fraction of the decays at a given distance that reach the counter. This fraction must be multiplied by the fraction of decays occurring at the given point to obtain the relative μ contribution from that point. The total μ contamination is obtained by summing the contributions from each segment of path length. The steps in the calculation are as follows.

1. Divide the path length into segments.
2. From the midpoint of each segment, calculate the laboratory angle θ: $\tan\theta = r_c/r$, r_c = radius of counter

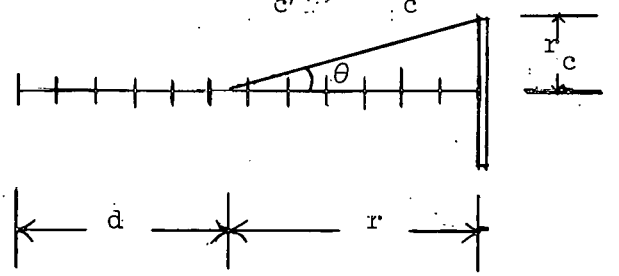

3. Convert θ to c.m. system by using the equation at end of this appendix. There will be two values of θ', corresponding to μ's that come off backward in the c.m. and μ's that come off in the forward direction. Even some of the μ's in the backward hemisphere reach the counter because of the large forward velocity of the c.m.
4. Convert the c.m. angle θ' to a c.m. solid angle Ω':

$$\Omega' = 2\pi \quad (1-\cos\theta')$$

5. Add the forward and backward solid angles for each segment and divide by 4π to obtain the fraction of decays reaching the counter.
6. Calculate the mean distance of travel before decay λ:

$$\lambda = \beta \gamma c \tau_0$$

where

$\beta = v/c$

v = velocity of pion,

c = speed of light,

$\gamma = (1 - \beta^2)^{-1/2}$

and

$\tau_0 = 2.55 \times 10^{-8}$ sec.

7. Calculate $e^{-d/\lambda}$ for each segment to determine the fraction of initial beam that decays in each segment. (The distance d is measured from the start of the π^- flight to the point of decay)
8. Multiply the fraction of decays in each segment by the fraction of muons reaching the counter, to determine fraction of initial beam that gives μ's in counter for each segment.
9. Sum up μ contributions from all the segments.
10. At the counter, the fraction of the beam that is pions is given by the number of pions still remaining in the beam divided by the total number of particles.

The total number of particles at the counter is the sum of the pions still remaining plus the muon contamination of the beam. The initial contamination can be determined by a range curve. Then we assume that all the muons and electrons initially present reach the counter telescope. These statements apply to the case where the contamination of the beam is known at some point (e.g., liquid-hydrogen

target) and the contamination is desired at some point downstream (e.g., chemistry target).

The equation for the conversion of the lab angle of the muon into the c.m. angle is double valued for the c.m. angle. Therefore it is simpler to calculate the lab angle for a given c.m. angle and make a plot of lab angle vs c.m. angle. The c.m. angles may then be interpolated from the known lab angles. The equation is:[42]

$$\tan\theta = \frac{\beta' \sin\theta'}{\gamma(\beta + \beta' \cos\theta')} ,$$

where

β' = v/c for μ^- in c.m.,

β = v/c for π^- in lab,

θ = lab angle,

θ' = c.m. angle,

and $\gamma = (1 - \beta^2)^{-1/2}$ for π in lab.

β' is a constant for π-μ decay equal to 0.268

β and γ depend on the particular π-beam energy involved.

C. Chemical Procedures

1. Separation of Cu from Zn foils after proton bombardments:

   a. Dissolve Zn foil in 6M HCl.

   b. Add 10 mg Cu^{++} carrier and holdback carriers for Ni^{++}, Co^{++}, $Fe^{(++)}$ and Mn^{++}.

   c. Dilute solution to 3M HCl.

   d. Bubble in H_2S gas and precipitate CuS.

   e. Centrifuge, dissolve CuS in 6M HCl plus 1 drop 30% H_2O_2.

   f. Make Cu^{++} solution just barely acidic, add Na_2SO_3, and heat until solution is decolorized to reduce Cu^{++} to Cu^{+}.

   g. Add 1M KSCN to precipitate CuSCN.

   h. Centrifuge, dissolve CuSCN in HCl and H_2O_2.

   i. Make strongly ammoniacal, add $Na_2S_2O_4$, and heat to precipitate Cu.

   j. Filter, wash with water, alcohol, and acetone; mount.

2. Separation of Mn from Fe foils after proton bombardments:

   a. Dissolve Fe foil in 6M HNO_3 solution containing 10 mg Mn^{++} carrier and holdback carriers for Cr^{+++}, V^{+++} and Sc^{+++}.

   b. Add concentrated HNO_3, heat and add $KClO_3$ to precipitate MnO_2.

   c. Centrifuge, dissolve MnO_2 in 6M HNO_3 and 1 drop 30% H_2O_2.

   d. Pour solution carefully into hot solution of excess NaOH and H_2O_2 to precipitate MnO_2.

   e. Centrifuge, dissolve MnO_2 in 6M HNO_3.

   f. Repeat precipitation of MnO_2 with $KClO_3$.

   g. Filter, wash with H_2O, alcohol and acetone; mount.

3. Separation of Na from Al after pion bombardment:

   a. Dissolve Al in big bucket (3 liter) of 6M HCl containing 30 mg Na^{+} carrier.

   b. Make solution basic with NH_4OH to precipitate $Al(OH)_3$.

c. Centrifuge in floor-model centrifuge (4-liter capacity).

d. Wash precipitate thoroughly with H_2O then recentrifuge.

e. Collect supernatant solutions (2 or 3 liters), acidify with 4/1 mixture of concentrated HNO_3 and HCl.

f. Evaporate to small volume by using all possible techniques for safe rapid evaporation. Add more acid as necessary to destroy NH_4Cl.

g. When solution is less than 30 mliter, an $Fe(OH)_3$ scavenging precipitation may be performed if desired. (No noticeable effect on the decay curve was observed due to this step).

h. Evaporate the solution to dryness in a small beaker.

i. Heat in a muffle furnace for 10 min at 600° C. NH_4^+ salts should be completely destroyed and Na^+ will be converted to Na_2O; cool.

j. Add 1 mliter of concentrated $HClO_4$ and fume carefully to dryness.

k. Dissolve $NaClO_4$ in 10-mliter n-butanol.

l. Add 2 mliter n-butanol saturated with dry HCl.

m. Filter the NaCl formed, wash with butanol-HCl mixture; mount.

4. Separation of Fe from Cu after pion bombardments:

a. Dissolve Cu target in concentrated HNO_3 and a little concentrated HCl.

b. Add 30 mg Fe carrier and dilute.

c. Make strongly ammoniacal, filter out $Fe(OH)_3$.

d. Dissolve Fe in HCl, dilute to 2N.

e. Add Cupferron reagent to precipitate Fe.

f. Centrifuge, dissolve Fe-cupferron precipitate in HCl.

g. Precipitate $Fe(OH)_3$ with NH_4OH.

h. Filter, ignite to Fe_2O_3.

i. Transfer to filter chimney.

j. Wash with H_2O, alcohol, and acetone; mount.

5. Separation of Cu, Mn and Ni from Zn after pion bombardments:

   a. Dissolve Zn in 6M HCl.
   b. Add 30 mg each of Cu^{++}, Mn^{++} and Ni^{++} carriers.
   c. Dilute to 3M HCl, pass in H_2S gas.
   d. Filter CuS and continue as in Procedure 1 to obtain Cu sample.
   e. Take filtrate from step d, make strongly basic with NaOH to precipitate MnO_2 and $Ni(OH)_2$.
   f. Dissolve precipitate in HCl, make pH about 6.
   g. Add dimethylglyoxime reagent to precipitate NiDMG.
   h. Filter NiDMG, dissolve, and reprecipitate NiDMG.
   i. Ignite NiDMG to NiO, filter, wash with H_2O, alcohol and acetone; mount.
   j. Evaporate filtrate containing Mn from step h to remove HCl.
   k. Add concentrated HNO_3, then add $KClO_3$ to precipitate MnO_2.
   l. Continue as in Procedure 2 to obtain precipitate of MnO_2.

D. Beta Counter and Efficiency Determination

1. Counters

The samples from the proton bombardments were counted on end-window gas-flow beta proportional counters. These counters have been described by Blann.[90] The community counters mentioned by him were brought up to date and standardized. New amplifiers and scalers of an improved design were obtained for seven β counters. A potentiometer gave increased sensitivity to the high-voltage control on the amplifier. The scaler has a built-in power supply which feeds the amplifier also. A regulated 5000-V power supply replaced the old nonregulated supply.

The detectors were modified in several ways to achieve greater reproducibility. The electrode that formerly consisted of a loop of tungsten wire on a single hypodermic needle was replaced with a new design. This consists of two hypodermic needles suspended like an inverted V from the top of the chamber. Across the open end of the V is an 180-deg arc of 0.001-in. tungsten wire with an arc diameter of 1 cm. This design allows the wire to come closer to the window with a resultant decrease in background. The aluminized Mylar windows were replaced with goldized Mylar, the evaporated gold being on the inside layer of the Mylar. This made the counters less sensitive to light. A thin aluminum ring was designed for each detector to hold the Mylar window securely in place. With this ring it is possible to put considerable gas pressure on the window without having the window bow. This eliminates changes in efficiency due to changes in gas pressure. Brooks-mite gas flowmeters replaced the "bubblers" previously used to regulate gas pressure. A lucite ring was designed for each detector to hold it securely in the counter stand.

After these changes, (and with constant care and feeding) each counter gave a constant counting rate to within 1% with a Cl^{36} source.

All counters agreed to within 2% for this standard on shelf 3. The backgrounds normally were about 9 counts/min with a fluctuation of about 0.5 counts/min, depending directly on whether the Bevatron was operating or not. (One of these counters was placed on a portable rack and then the background was measured in several locations throughout the building. The first floor gave approximately 1 count/min lower background than the second-floor counting room.)

2. Efficiencies

The efficiency of these β counters was determined following a procedure outlined by Bayhurst and Prestwood.[91] Their method eliminates the need for making separate corrections for backscattering, shelf geometry, air absorption, etc. They found that the efficiency for β counting on a given shelf was a smooth function of the average energy of the β spectrum for allowed β spectra. The average energy for positive or negative β spectra for a given nuclear charge and β end-point energy is read from a family of curves. For a given-type β counter and sample-mounting technique, an empirical curve must be drawn giving the efficiency of the counter vs the average energy of the β spectrum. This curve is shown in Fig. D-1 for the β counters and mounting techniques used in this experiment. (For mounting techniques see Sec. VI. B2) The efficiencies were obtained by comparing the counting rate of a weightless sample on a 4π counter with the counting rate of the same source mounted in the standard fashion and counted on shelf 1 of the β counters.

For Mn^{56} and Cu^{67}, plots were made of the efficiency on a given shelf vs the thickness of the precipitate in which the activity is located. These data are shown in Fig. D-2. Mn^{56} is representative of most of the high-β-energy activities. Cu^{67} shows the strong effect the source thickness has on the efficiency of low-energy β's. The data of Blann[90] and Crespo[92] were used when source-thickness corrections were desired for other activities. Data were also obtained for the relative counting efficiency on various shelves for Na^{22}, Na^{24}, Mn^{56},

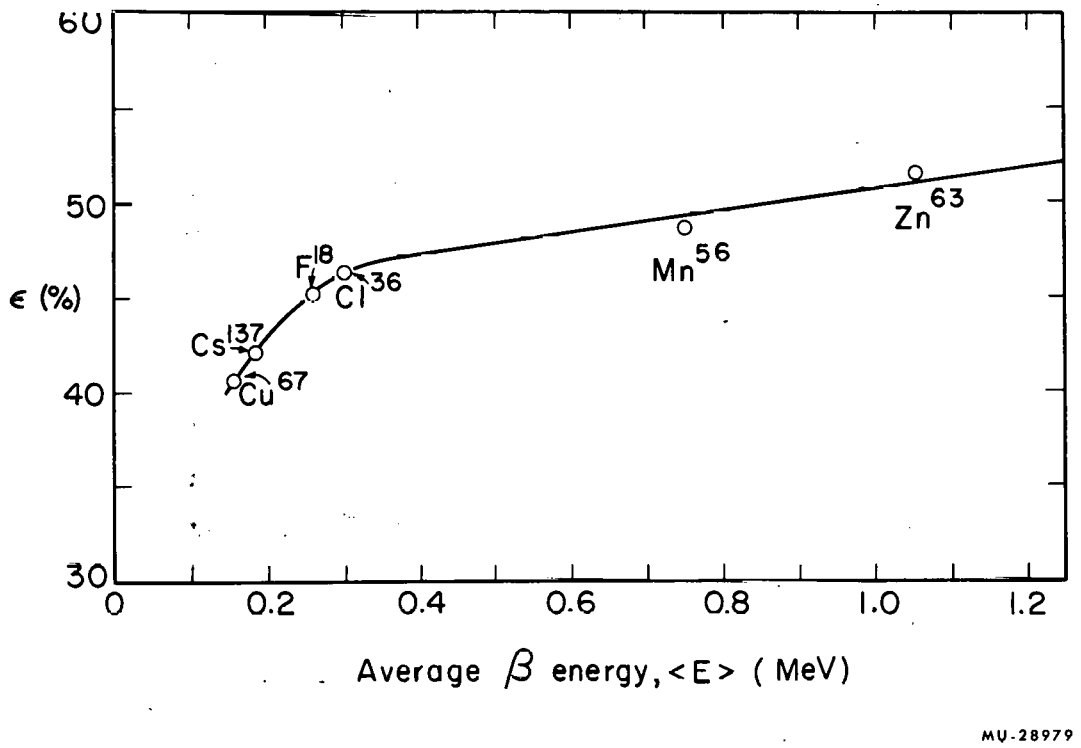

Fig. D-1. Beta-counting efficiency vs average β energy for shelf 1 of end-window proportional counters. P^{10} point determined by Mahony.[98] Zn^{63} point determined by Smith.[98] Other data are from this work. All efficiencies were determined with weightless sources.

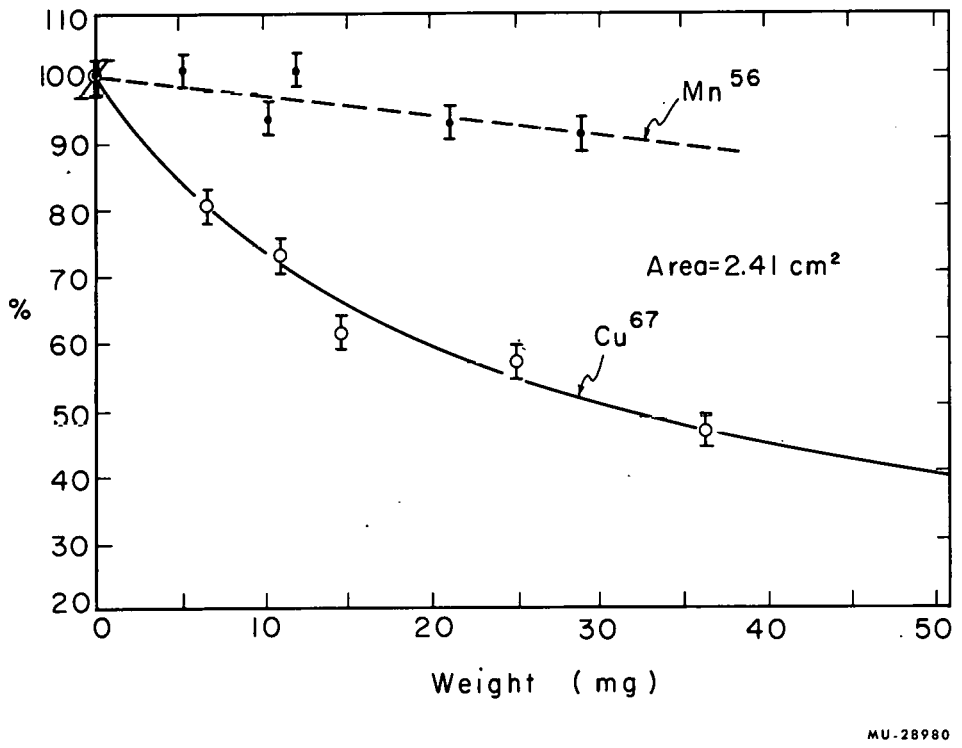

Fig. D-2. Counting-efficiency correction vs weight of sample.

$$\% = 100 \left(\frac{\beta\text{-counting efficiency for thickness x.}}{\beta\text{-counting efficiency for 0 thickness}} \right)$$

Smooth curve I is for Cu^{67} prepared as free Cu.
Dashed curve I is for Mn^{56} prepared as MnO_2.
Weight refers to the weight of the element rather than the weight of the compound. All sources were prepared on 2.41-cm^2 circular disks.

Cu^{67}, Mn^{52}, Cl^{36} and Cs^{137}. These data showed that the efficiency could vary by a few percent for the same activity on the same shelf of different counters, even though the standards agreed to within 1%. This variation is presumably due to small differences in shelf distances.

Once the empirical curves have been determined for efficiency vs average β energy, and for efficiency vs sample thickness, then it is possible to calculate efficiencies for any other activity. The average energy is determined from the graph, the efficiency of a weightless source is determined from the empirical curve, and the source-thickness correction is determined by comparing the new activity with the absorption effect of some other activity with a similar average energy. The error on the efficiencies determined in this manner is about 5%.

E. Physics Groups That Provided Meson Beams

1. Moyer Group - W.C. Bowman, J.B. Caroll, J.A. Poier, M. Pripstein
   Oct. 1961
2. Crowe Group - R. Beck, N. Dairiki, T. Maung,.
   May 1962
3. Crowe Group - B. Czirr
   June 1961
4. Moyer Group - H. Goldberg, R.W Kenney
   Feb. 1962
5. Segrè Group - N. Booth, R. Hill, H. Rugge, O. Vik
   April 1962
6. Moyer Group - B.C. Barish, R.J. Kurz, J. Solomon, V. Perez-Mendez July 1961, Dec. 1961, Jan. 1962, April 1962
7. Segrè Group - T. Eliof, W. Johnson, C.E. Wiegand, T. Ypsilantis
   March 1961
8. Crowe Group - G. Bingham, H. Kruger
   Sept. 1961

REFERENCES

1. H. Yukawa, Proc. Phys. Math. Soc. Japan 17, 48 (1935).
2. C.F. Powell, Nature 160 453, 486 (1947).
3. E. Gardner and C.M. Lattes, Science 107, 270 (1948).
4. A. Turkevich and J.B. Niday, Phys. Rev. 84, 1253 (1951).
5. N. Sugarman and A. Haber, Phys. Rev. 92, 730 (1953).
6. L. Winsberg, Rev. Sci. Instr. 25, 1079 (1954).
7. L. Winsberg, Phys. Rev. 95, 198 (1954).
8. M. Rich and R. Madey, Range-Energy Tables, University of California Laboratory Report UCRL-2301, March, 1954 (unpublished).
9. J. Mollenauer, Phys. Rev. 127, 867 (1962).
10. I am indebted to the Moyer physics group for loaning me the discriminator and scale-of-eight unit.
11. J. Ashkin, T. Fazzini, G. Fidecaro, Y. Goldschmidt-Clermont, N.H. Lipman, A.W. Merrison, and H. Paul, Nuovo Cimento 16, 490 (1960).
12. O. Chamberlain, Optics of High Energy Beams, Ann. Rev. Nuclear Sci. 10, 161 (1960).
13. O. Chamberlain, E. Segrè and C. Wiegand, Phys. Rev. 83, 923 (1951).
14. L.B. Auerbach, T. Eliof, W.B. Johnson, J. Lach, C.E. Wiegand and T. Ypsilantis, Study of Pion-Pion Interaction from Pion Production by Pions, Lawrence Radiation Laboratory Report UCRL-10212 Rev, May 1962 (unpublished).
15. David Anderson, ex-Kansas University track star, has recently lowered this record to 1:41.
16. B. Grimeland, Intern. J. Appl. Radiation Isotopes 4, 116 (1958).
17. J. Cumming and R. Hoffman, Rev. Sci. Instr. 29, 1104 (1958).
18. D. Strominger, J. Hollander, and G. Seaborg, Rev. Mod. Phys. 30, 585 (1958).
19. H. Bosch and T. Urstein, Beta Spectroscopy with Scintillation Counters, Lawrence Radiation Laboratory Report UCRL-8924, Oct. 1959 (unpublished).

20. P.J. Campion, Intern. J. Appl. Radiation Isotopes 4, 232 (1959).

21. Dr. Owen Chamberlain and members of his group donated the time needed for this bombardment.

22. The 310-MeV π^- beam was set up at the 184-in cyclotron by Norman Booth, Roger Hill, Hugh Rugge, and Olav Vic in April, 1962 to measure the polarization of the neutron in the reaction $\pi^- + p \rightarrow \pi^o + n$. (unpublished).

23. N. Metropolis, R. Bivins, M. Storm, J.M. Miller, G. Friedlander, and A. Turkevich, Phys. Rev. 110, 204 (1958).

24. A. Poskanzer, J. Cumming, G. Friedlander, J. Hudis, and S. Kaufman, Bull. Am. Phys. Soc. 6, 38 (1961).

25. A. Poskanzer and L. Remsberg (Brookhaven National Laboratory, Upton, L.I., N.Y.), private communication.

26. A.E. Ignatenko, CERN Symposium on High Energy Accelerators and Pion Physics. Geneva, June 1956, (CERN, Geneva, 1956), Vol 2, p. 313.

27. Mark Gusakow, Contribution A L'Etude Des Reactions (p,pn) A Moyenne Energie, (Ph.D. Thesis), University of Paris, 1962 (unpublished).

28. P. Strohal and A. Caretto, Phys. Rev. 121, 1815 (1961).

29. P. Benioff, Phys. Rev. 119, 316 (1960).

30. S. Markowitz, F. Rowland, and G. Friedlander, Phys. Rev. 112, 1295 (1958).

31. N. Metropolis, R. Bivins, M. Storm, A. Turkevich, J. M. Miller, and G. Friedlander, Phys. Rev. 110, 185 (1958).

32. R. Serber, Phys. Rev. 72, 1114 (1947).

33. E. Merz and A. Caretto, Phys. Rev. 126, 1173 (1962).

34. W. Crandall, G. Millburn, G. Pyle, and W. Birnbaum, Phys. Rev. 101, 329 (1956).

35. J. Cumming, G. Friedlander, and C. Swartz, Phys. Rev. 111, 1386 (1958).

36. J. Cumming, G. Friedlander, and S. Katcoff, Phys. Rev. 125, 2078 (1962).

37. S. Singh and J. Alexander, Phys. Rev. 128, 711 (1962).

38. G.F. Chew, Phys. Rev. 80, 196 (1950).

39. G.F. Chew and G. Wick, Phys. Rev. 85, 636 (1952).

40. K.M. Watson, Revs. Mod. Phys. 30, 565 (1958).

41. I. Dostrovsky, Z. Fraenkel and G. Friedlander, Phys. Rev. 116, 683 (1959).

42. Philip Morrison, Experimental Nuclear Physics, Vol. II, E. Segrè, Ed. (John Wiley and Sons, Inc., New York, 1953), Part VI, pp. 3 to 11. This article is a readable reference for relativistic kinematics.

43. I am indebted to Dr. B. Udgaonkar and Dr. V. Singh for explaining the procedure for estimating the resonance broadening.

44. J. Garron, J. Jacmart, M. Riou, C. Ruhla, J. Teillac, and K. Strauch, Nuclear Phys. 37, 126 (1962).

45. Nikol'skii, Kudrin, and Ali-Zade, Soviet Phys. JETP 5, 93 (1957).

46. R.H. Miller, Nuovo Cimento 6, 882 (1957).

47. P. Benioff, Phys. Rev. 119, 324 (1960).

48. R. Hofstadter, Nucleus and Nucleon Scattering of High Energy Electrons, Ann. Rev. Nuclear Sci. 7, 231 (1957).

49. J. Helland, T. Devlin, D. Hagge, M. Longo, B. Moyer, and C. Wood, Angular Distributions in $\pi^{\pm}$p Elastic Scattering in the Ranges 530-1550 MeV, Lawrence Radiation Laboratory Report UCRL-10263, May, 1962 (unpublished).

50. B. Moyer, Rev. Mod. Phys. 33, 367 (1961).

51. L. Goodwin, R. Kenney, and V. Perez-Mendez, Phys. Rev. 122, 655 (1961).

52. L.C.L. Yuan, Proc. of the CERN Symposium on High Energy Accelerators and Pion Physics, Geneva, June 1956 (CERN, Geneva, 1956), Vol. 2, p. 195. (See other papers in this volume.)

53. P. Wolff, The Inelastic Scattering of Protons from Carbon, University of California Radiation Laboratory Report UCRL-1410, July 1951 (unpublished).

54. J. Cladis, W. Hess, and B. Moyer, Phys. Rev. 87, 425 (1952).

55. Y. Prokoshkin, Pion Production in p-d Collisions and Intranuclear Motion of Nucleons, Report submitted to 6th Session of Scientific Council of Joint Institute of Nuclear Research in May 1959, Dubna, Joint Institute of Nuclear Research Report NP-8201, 1959 (unpublished).

56. B. Moyer, Phys. Rev. 99, 875 (1955).

57. J. Garron and J. Jacmart, J. phys. radium 22, 622 (1961).

58. P. Benioff, Phys. Rev. 128, 740 (1962).

59. T. Clements and L. Winsberg, Phys. Rev. 122, 1623 (1961).

60. M. Goldberger, Phys. Rev. 74, 1269 (1948).

61. R.M. Frank, J.L. Gammel, and K.M.Watson, Phys. Rev. 101, 891 (1956). The α used herein corresponds to the γ of these authors.

62. R.M.Sternheimer, Phys. Rev. 106, 1027 (1957).

63. I.G. Ivanter and L.B. Okun, Soviet Phys.—JETP 5, 340 (1957).

64. G. Philbert, Compt. rend. 246, 591 (1958).

65. Jean Grea, Recherches sur l'application de la Methode de Monte Carlo dans les Processus de Physique Nucleaire a Haute Energie: Interaction des Pions Negatifs de 4.5 GeV (Ph.D. Thesis), Universite de Lyon, Oct. 1961 (unpublished).

66. E. Grigor'ev and N. Mitin, Soviet Phys.—JETP 5, 378 (1957).

67. J.M. Miller,(Brookhaven National Laboratory, Upton, L.I.,N.Y.) private communication.

68. D. Anderson and R. Newman (Lawrence Radiation Laboratory, Berkeley, California), private communication.

69. S. Markowitz,(p,pn) Reactions in the BeV Energy Region, (Ph.D. Thesis), Princeton University, Jan. 1957 (unpublished).

70. H. Bethe and F. de Hoffman, Mesons and Fields, (Row, Peterson and Company, Evanston, Illinois, 1955), Vol.II.

71. J. Caris, Charge Exchange Scattering of Negative Pions by Hydrogen at 230, 260 290 317 and 371 MeV (Ph.D. Thesis), Lawrence Radiation Laboratory Report UCRL-9048, March 1960 (unpublished).

72. H. Byfield, J. Kesler, and L.M. Lederman, Phys Rev. 86, 17 (1952).

73. A. Conforto and R. Sard, Phys. Rev. 86, 465 (1952).
74. M. Rosenblueth, Phys. Rev. 75, 532 (1949).
75. A. Turkevich, Ann. Rev. Phys. Chem. 4, 119 (1953).
76. W. Ware and E. Wiig, Phys. Rev. 122, 1837 (1961).
77. P. Strohal and A. Caretto, Phys. Rev. 121, 1815 (1961).
78. A. Caretto and G. Friedlander, Phys. Rev. 110, 1169 (1958).
79. D. Morrison and A. Caretto, Phys. Rev. 127, 1731 (1962).
80. G. Rudstam, P. Stevenson and R. Folger, Phys. Rev. 87, 358 (1952).
81. A.G.W. Cameron, A Revised Semi-Empirical Atomic Mass Formula, CRP 690, Chalk River, Ontario, March 1957, AECL No. 433.
82. R. Wolfgang and G. Friedlander, Phys. Rev. 96, 190 (1954).
83. R. Wolfgang, E. Baker, A. Caretto, J. Cumming, G. Friedlander and J. Hudis, Phys. Rev. 103, 394 (1956).
84. J. Cumming, J. Hudis, A. Poskanzer, and S. Kaufman, The $Al^{27}(p,3pn)Na^{24}/C^{12}(p,pn)C^{11}$ Cross-Section Ratio in the GeV Region, Brookhaven National Laboratory Report BNL-6270, 1962 (to be published).
85. P. Kruger and N. Sugarman, Phys. Rev. 99, 1459 (1955).
86. G. Rudstam, E. Brunnix, and A. Pappas, Phys. Rev. 126, 1852 (1962).
87. E. Brunnix, High Energy Nuclear Reaction Cross-Sections, CERN Report CERN-61-1, Jan. 1961 (unpublished).
88. A. Turkevich and S. Fung, Phys. Rev. 92, 521 (1953).
89. T. Ericson, F. Selleri, and R. Van de Walle, Nuclear Phys. 36, 353 (1962).
90. H.M. Blann, Fission of Gold with 112 MeV C Ions: A Yield Mass and Charge Distribution Study (Ph.D. Thesis), Lawrence Radiation Laboratory Report UCRL-9190, May 1960 (unpublished).
91. B. Bayhurst and R. Prestwood, Nucleonics 17, 82 (1959).
92. V. Crespo, Ejection of Large Fragments in High Energy Nuclear Reactions (Ph.D. Thesis), Lawrence Radiation Laboratory Report UCRL-9683, Sept. 1961 (unpublished).
93. N. Horwitz and J. Murray, Phys. Rev. 117, 1361 (1960).
94. I. Prokoshkin, A. Tiapkin, Soviet Phys.—JETP 5, 148 (1957).

95. W. Burcham, J. Symonds and J. Young, Proc. Phys. Soc. (London) 68A, 1001 (1955).

96. A.E. Glassgold, Nuclear Reactions at Very High Energies, invited paper presented at the International Symposium on Direct Interactions and Nuclear Reaction Mechanisms, held in Padua, Sept. 3-8, 1962 (unpublished).

97. V.S. Barashenkov and V.M. Maltsev, Fortschr. Physik 9, 549 (1961).

98. John Mahony and Charles Smith (Lawrence Radiation Laboratory, Berkeley, California), private communication.

99. J.M. Meadows and R.D. Holt, Phys. Rev. 83, 47 (1951).